Università degli Studi di Trieste

XXVII Ciclo del Dottorato di Ricerca in
Environmental and Industrial Fluid Mechanics

Large Eddy Simulation of Suspended Sediment in Turbulent Open-Channel Flow

Settore scientifico-disciplinare: ICAR/01

Ph.D. Student:	Maryam Dallali
Supervisor and Director:	Prof. Vincenzo Armenio
Co-Supervisor:	Prof. Ana Maria Ferreira da Silva
Co-Supervisor:	Prof. Andrew Pollard

Academic Year 2014-2015

Abstract

This study aims to shed light on the dark sides of sediment transport and meandering channel flow patterns. For this purpose, the Large Eddy Simulation methodology is used to investigate sediment transport in open-channel flow and also to predict the meandering channel flow pattern in two sine-generated channels.

In the turbulent flows the transported suspended sediments is usually assumed in a passive form. In other word, the feedback effect of sediment suspension on near-wall momentum transport is neglectable. The first phase of this research is devoted to quantify the just mentioned effect in the open channel flow. A single phase approach is used to gain better description of sediment-turbulence interaction. The effect of suspended particles on flow properties is presented through a buoyancy term in momentum equations.

The initial analysis of concentration profiles shows that the combination of large near-wall concentration and small deposition term, enhances the suspension concentration in case of small particles. Considering the buoyancy effect (two-way coupling model), the suspension concentration is reduced compared to the passive case. In addition, the buoyancy effects on the velocity field are also discussed. The comparison of streamwise mean velocity profiles reveals that the interaction of suspended particles with the underlying flow suppresses the vertical turbulent fluctuations and consequently reduces the von Kàrmàn constant (κ). The results clearly show that, in presence of large suspension, the two-way coupling approach should be applied to represent the sediment-turbulence interaction.

The second phase of this research is dedicated to gain insight into the complex three-dimensional nature of the meandering streams, in particular the secondary flow and turbulence characteristics. The curvature-induced secondary motion in the flow domain, which is the most typical feature of meandering channel flow, depends on turbulence. This secondary current removes the eroded material from the concave banks, transports it across the channel, and deposits it on the convex banks.

In agreement with the conditions present in natural streams, the channel center-line is idealized as a sine-generated curve, characterized by a downstream variation in curvature. Moreover, the presence of the free-surface which moves according to the actual flow field conditions is considered in

the numerical model. The numerical results reveal the significant influence of the channel sinuosity on the velocity pattern as well as the development of the secondary flow throughout the meandering bend. A detailed investigation of the bed shear stress and Reynolds stresses patterns clarifies the complex interaction of the turbulence structure with the secondary motion inside the bend.

In addition, a preliminary study is presented to clarify the distribution of suspended sediments in the meandering channel. Comparison of the suspended sediment concentration contours reveals how the secondary flow mechanism and bed shear stress contribute to the non-uniform distribution of the dispersed phase.

To my Mother Mahboubeh, who made me believe in the true spirit of kindness and generosity.

Acknowledgment

Stepping into this Ph.D. program was a unique challenge in my life. It has been a long road, but here I am and today is the day: Writing this note of thanks is the finishing touch on my thesis. It has been a period of intense learning for me, not only in the scientific area, but also on a personal level. Therefore, I would like to reflect on the people who have supported and helped me greatly throughout this period.

First of all, I wish to express my gratitude to my supervisor, Prof. Vincenzo Armenio, who taught me new insights into science. He patiently disciplined my scientific work with his intuition, and led me to become a better professional. This thesis would not have been possible without his valuable and unrelenting guidance and feedback.

I also wish to sincerely thank my co-supervisor Prof. Ana Maria da Silva, who provided me with the opportunity to spend more than one year and a half of my academic program in her research group at the department of Civil Engineering in Queens's university. I really appreciate the effort she generously made to teach me the practical approaches to my research during the long discussion hours even over the weekends. This opportunity inspired me with new visions for my professional career, and I had the pleasure of working with people who warmly contributed their stories, histories, and experiences.

Moreover, I would like to extend my gratitude to Prof. Andrew Pollard who welcomed our extensive discussions about my research and asked inspiring question through our weekly discussion sessions.

Additionally, I wish to acknowledge the HPC facility, Albert in Malta for their computational time and support.

I would also like to thank my colleague Santiago for his contribution in the development of my numerical model.

My thanks also go to my friend Arash for his time and support over the last tough months of my Ph.D. program; it is always great to have the hope you share.

Special thanks to my friends, Sogol and Soheil who supported me throughout the cold days of my stay in Canada with memorable moments. Simply put, that was one of the happiest times of my life.

Last but not least, I wish to thank my family, who has been encouraging,

supportive and particularly for the belief they have shown in me. This goes especially to my mom; thank you for making me more than who I am.

Contents

List of Figures

List of Tables

Chapter 1

Introduction

It has long been recognized that erosion and deposition processes occur naturally in alluvial rivers and lead to change their form. The most commonly occurring natural pattern in rivers, named meandering, consists of a series of alternating curved reaches with pools at the outer bank, and deposition along the inner bank.

A detailed understanding of flow through river meandering and the interaction between that flow and the bed is a complicated process because the flow is usually turbulent and characterized by a spectrum of rotational eddies at various scales. In turbulent motion, the ability of mixing and transporting momentum and scalars at rates much higher than those due to molecular diffusion is another important feature. Until now, predictions of flow and sediment transport in rivers have mostly been performed at the levels of 1D and 2D simulations, which usually neglect the influence of secondary flows. However, three-dimensional effects are important for sediment transport both in the bed-load mode and in the suspended mode.

During recent years, three-dimensional (3-D) computational fluid dynamics (CFD) modeling has emerged as a powerful tool for studying complex flows in man-made channels and natural rivers. Differently from experimental studies, the computational approach can simulate at full scale and give detailed information on the flow field.

The complex turbulent structures like secondary flow cells, vortices and Reynolds stresses can be effectively and distinctly identified using high-resolution eddy-resolving techniques. Nowadays, different computational frameworks are used to solve Navier-Stokes equations which are the governing equations for any fluid flow. Direct Numerical Simulation (DNS) of the Navier-Stokes equations has emerged as a leading research tool for examining the physics of turbulence at moderate Reynolds numbers because of their unique ability to provide fully resolved spatial-temporal evolution of the flow fields without any modeling approximation. On the other hand, DNS is, in a way, the most straightforward approach to CFD which either

requires a high-resolution numerical schemes or a grid system with very fine grid resolution. The only drawback in this approach is that solutions are available only at low-to-moderate values of Reynolds number.

Thereby, instead of solving for the instantaneous flow-field, approaches based on the Reynolds-average Navier-Stokes (RANS) equations are the most prevalent for CFD problems. Since RANS deals with statistical quantities of turbulent flows, the solutions are obtained through the use of turbulence models, whose reliability depends on a number of empirical constants.

The Large Eddy Simulation (LES) methodology intermediate between DNS and RANS seems to be more appropriate, since instead of averaging the equations, it makes use of a low-pass spatial filtering in order to separate the resolved scales from the sub-grid (non-resolved) scales. The main idea of this method is to simulate the largest, most energetic turbulent motions directly, while modelling the unresolved small-scale turbulence.

Over the years, LES has been used to investigate a wide class of flow fields of interest in hydraulics. Herein, LES is used to investigate the suspended sediment transport in turbulent open channels.

First, we numerically study the sediment transport in an idealized, straight open-channel flow. We first analyse under which conditions the suspended phase can be considered as passively transported by the carrying fluid. Successively we move to the analysis of more complex, meandering flows.

Despite the importance of sediment erosion and sediment transport, the fundamental aspects involved are far from being completely understood. In the researches on the prediction of sediment transport for several flow topologies and conditions, less attention has been dedicated to a critical evaluation of scalar transport modeling. Available numerical experiments have systematically adopted the Eulerian framework for dispersion modeling. The scalar quantity in this approach is assumed to be a passive scalar, whose mass fraction is small and does not give a feedback on momentum transport. Among the experimental studies, the influence of suspended particles on turbulence properties of mean flow has been considered through a damping function applied to the eddy viscosity profile. When the mass fraction of the dispersed phase is large, the two-phase flow framework can be employed.

The objective of this study is to first provide a numerical study to further investigate the effect of sediment transport on dynamics of turbulent flow. Large Eddy Simulations are carried out to study scalar transport considering both one-way coupling (passive scalar case) and two-way coupling approach in Eulerian framework. The sediment-induced buoyancy term is considered in the Boussinesq form of 3D Navier-Stokes equations.

Successively, turbulent flow in meandering channels is addressed. The turbulent flow field in channel bend is quite complex. The presence of turbulence, coherent structure and shear layers within high curvature bends, impact the river erosion and sediment transport. The nonlinear interaction

of curvature-induced secondary flow and primary flow leads to increased anisotropy in circularly motion. The shorter length of the channel bend in the inner bank compared to the outer bank, results in a non-uniform distribution of stream-wise velocity in cross-stream direction. This redistribution leads to the acceleration/deceleration zones of flow in inner/outer parts of cross-section. The strength of secondary flow in channel bends which is a function of channel curvature is varied along the bend. These variations can directly affect the bed-shear stress distribution and consequently the erosion pattern. Although details of turbulence and flow field have previously been investigated for curved channel, most of these studies have involved the sharp and circular bend. As far as we know the numerical models employed have not considered the presence of a free surface, thus limiting the attention to flows with very low Froude number. This is the first time that freely evolving free-surface is considered in the investigation of flow in meandering channel. We performed large-eddy simulations (LES) of flow in two meandering channels. It is expected that insights gain from LES simulation of turbulent flow in meandering channel improve the understanding of turbulent mechanism in natural rivers.

Since the properties of the flow passing through the meandering channels is obviously different from the one in straight channels due to the presence of the secondary flow, the study of concentration field in meandering channel is presented in this thesis as well.

This thesis is structured as follows: the mathematical and numerical models for open channel flow and dispersed phase are presented in chapter 2. In chapter 3, the sediment transport model is introduced to investigate the suspended sediment concentration in a straight open channel flow. The simulations are performed for one-way and two-way coupling approaches. Different sediment sizes are tested and the results are compared with theoretical formula for validation. Chapter 4, is dedicated to study the complex 3D flow in meandering channels. The flow parameters are chosen to match the experiment by Binns and da Silva [2015] for validation purposes. The simulation results are presented for time-averaged flow properties. Finlay, in chapter 5, the simulation results of suspended sediment in the meandering channels are reported.

Chapter 2

Mathematical Model

The purpose of this chapter is to describe the mathematical framework of the Large Eddy Simulation. For this purpose, the theoretical basis of the simulation including the conservation of mass and momentum equations, is presented in Section 2.1. The LES approach and derivation of the corresponding equations, as well as the subgrid-scale modeling in the filtered form of Navier-Stokes equations are explained in Section 2.2. Section 2.3 deals with the numerical method to solve the governing equations. The details of the discretization technique which involves the grid system are covered in Section 2.4.

2.1 Equations of Motion

As is well known, the conservation of mass (continuity) and Navier-Stokes equations (N-S equations) are the governing equations of motion in a flow field. The N-S equations comprise the momentum equations. For an incompressible Newtonian fluid, the continuity and N-S equations can be written as:

$$\frac{\partial u_i}{\partial x_i} = 0, \tag{2.1}$$

$$\frac{\partial u_i}{\partial t} + \frac{\partial}{\partial x_j}(u_i u_j) = \frac{1}{\rho_0}\Pi - \frac{1}{\rho_0}\frac{\partial p}{\partial x_i} - g\delta_{i2} + \nu\frac{\partial^2 u_i}{\partial x_i \partial x_j}, \tag{2.2}$$

where $i, j = 1, 2, 3$ denote the three spatial directions x, y and z. The spatial variables x, y, z represent stream-wise, wall-normal and span-wise directions, respectively, u_i is the velocity component in i-direction, Π is an imposed pressure gradient driving flow, p is hydrodynamic pressure, ρ_0 is density of fluid and ν is kinematic viscosity, related to dynamic viscosity μ by $\nu = \mu/\rho_0$.

The interaction between the flow and erodible bed in turbulent open channels can result in sediment transport, leading to changes in bed bathymetry and flow characteristics. Thereby, to understand and predict the behavior of sediments transported by the turbulent flow, the concentration field has been introduced by means of the advection-diffusion equation [Zedler and Street, 2001]:

$$\frac{\partial C}{\partial t} + \frac{\partial}{\partial x_j}[(u_j - v_s\delta_{j2})C - \frac{\nu}{\sigma}\frac{\partial C}{\partial x_j}] = 0, \tag{2.3}$$

in which C is local suspended sediment concentration, σ is Schmidt number (usually assumed to be 1), v_s is sediment settling velocity which is directed toward the gravity and varies depending on particle size.

2.2 Computational Approach: LES-COAST

In LES, the large, energy-carrying eddies are resolved completely and the small structures are modeled. In order to obtain the filtered N-S equations for the Large Eddy Simulation, a spatial filtering process was applied to the governing equations. By application of this filtering, large and small structures can be explicitly separated.

The process involves a Kernel function $G(x)$ which defines the filtered property f as:

$$\overline{f}_i(x) = \int_D G(x, x^{'}) f_i(x^{'}) dx^{'}, \tag{2.4}$$

where D is the entire domain and $G(x, x^{'})$ is the Kernel function with a relevant characteristic width $\overline{\Delta}$. This divides the variables into resolved and subgrid-scale ($f_i = \overline{f}_i + f_i^{'}$). The Kernel function we use in LES-COAST solver is defined as

$$G(x) = \begin{cases} \frac{1}{\overline{\Delta}} & if \quad |x| \geq \frac{\overline{\Delta}}{2} \\ 0 & elsewhere \end{cases} \tag{2.5}$$

By imposing the Kernel function any spatial fluctuations shorter than the characteristic length scale are effectively damped.

Thus, by filtering the continuity and N-S equations (Equation 2.1 and Equation 2.2) and scalar transport equation (Equation 2.8) explicitly and then using the above relations, the following filtered equations can be derived when u_i is decomposed into resolved and subgrid-scale ($u_i = \overline{u}_i + u_i^{'}$):

$$\frac{\partial \overline{u}_i}{\partial x_i} = 0, \tag{2.6}$$

$$\frac{\partial \overline{u}_i}{\partial t} + \frac{\partial \overline{u}_i \overline{u}_j}{\partial x_j} = \frac{1}{\rho_0}\Pi - \frac{1}{\rho_0}\frac{\partial \overline{p}}{\partial x_i} - g\delta_{i2} + \nu\frac{\partial^2 \overline{u}_i}{\partial x_j \partial x_j} - \frac{\partial \tau_{ij}}{\partial x_j}, \tag{2.7}$$

$$\frac{\partial \overline{C}}{\partial t} + \frac{\partial}{\partial x_j}[(\overline{u_j} - v_s\delta_{j2})\overline{C}] = \frac{\nu}{\sigma}\frac{\partial^2 \overline{C}}{\partial x_j \partial x_j} - \frac{\partial \chi_j}{\partial x_j}, \tag{2.8}$$

where over-bar symbol "−"defines the filtering operator in the LES approach. These filtered equations simulate the evolution of large scales, while the effect of small scales are presented as SGS stress term τ_{ij} in Equation 2.7 and as SGS scalar flux χ_j in Equation 2.8.

To close the system of equations the terms τ_{ij} and χ_j, have to be represented. The SGS turbulent fluxes for flow and scalar quantity are respectively expressed as:

$$\tau_{ij} = \overline{u_i u_j} - \overline{u}_i \overline{u}_j \tag{2.9}$$

$$\chi_j = \overline{u_j C} - \overline{u}_j \overline{C}. \tag{2.10}$$

The SGS model commonly employs information from the smallest resolved scales as the basis to model the stresses of the unresolved scales. A number of SGS models are introduced next.

The most commonly employed model for SGS stress tensor (Eddy Viscosity SGS Model) was first introduced by Smagorinsky [1963]. The basic assumptions in this model can be summarized as follows:

- an inertial subrange exists in the scales that encompass the grid size.
- there is a balance between the production and dissipation of the SGS turbulent kinetic energy.

In the Eddy Viscosity SGS model, the term τ_{ij} is proportional to the strain rate tensor S_{ij} of the resolved scales as follows:

$$\tau_{ij} - \frac{\delta_{ij}}{3}\tau_{kk} = -2\nu_{sgs}\overline{S}_{ij} \ , \ \nu_{sgs} = (C_s\Delta)^2|\overline{S}| \tag{2.11}$$

where $\overline{S}_{ij} = -\frac{\nu_{sgs}}{2}(\frac{\partial \overline{u}_i}{\partial x_j} + \frac{\partial \overline{u}_j}{\partial x_i})$ and $|\overline{S}| = \sqrt{2\overline{S}_{ij}\overline{S}_{ij}}$ is its magnitude, ν_{sgs} is SGS eddy viscosity, $\overline{\Delta}$ is a characteristic length scale associated with the computational grid resolution and C_s is Smagorinsky coefficient which is adjusted empirically.

To improve the modeling performance of the Eddy Viscosity SGS Model, a dynamic Smagorinsky model is proposed (see Germano et al. [1991]) in which an additional test filter is applied to the equations. In this model, the coefficient of ν_{sgs}, (C_s) is determined locally by means of a dynamic procedure using the Germano identity (Germano et al. [1991]).

In Cartesian framework, the Germano identity is written as:

$$T_{ij} = \tau_{ij} + \mathscr{L}_{ij}, \tag{2.12}$$

in which $\mathscr{L}_{ij} = \widehat{\overline{u}_i \overline{u}_j} - \widehat{\overline{u}}_i \widehat{\overline{u}}_j$ is the "resolved turbulent stresses", and $T_{ij} = \widehat{\overline{u}_i \overline{u}_j} - \widehat{\overline{u}}_i \widehat{\overline{u}}_j$ is the "subtest scale stresses" that appear if the test filter $\widehat{\cdot}$, with width $\widehat{\overline{\Delta}} > \overline{\Delta}$, is applied to the filtered continuity and Navier-Stokes equations (Equation 2.6 and Equation 2.7). Applying a least squares approach, the coefficient C_s is evaluated as (Lilly [1992]):

$$C_s = -\frac{1}{2} \frac{\langle \mathscr{L}_{ij} M_{ij} \rangle}{\langle M_{mn} M_{mn} \rangle}, \tag{2.13}$$

where

$$M_{ij} = \widehat{\overline{\Delta}}^2 |\widehat{\overline{S}}| \widehat{\overline{S}}_{ij} - \widehat{\overline{\Delta}}^2 |\overline{S}| \overline{S}_{ij}, \tag{2.14}$$

and $\langle \cdot \rangle$ represents an appropriate ensemble or local averaging required to avoid the mathematical inconsistency that one encounters when removing C_s from a filtering operation.

While the dynamic model provides realistic predictions of C_s in a sufficiently resolved flow field, it has been found that the scale-invariance assumption in this model causes an under-prediction of C_s near the wall. To overcome this weakness, a Lagrangian version of dynamic Smagorinsky model was developed by Meneveau et al. [1996] in which C_s is averaged along fluid trajectories.

Among the aforementioned models, the contribution of the small scales in this simulation is parametrized by the use of the dynamic model [Germano et al., 1991] with the Lagrangian averaging technique proposed by Vreman et al. [1994] (see Armenio and Piomelli [2000]).

In the present study, a LES code (LES-COAST) has been used to solve the 3-dimensional Navier-Stokes equations for the incompressible flows and the advection-diffusion equation for suspended sediment concentration where the Boussinesq approximation for buoyancy effects is applied.The code is a parallel message passing interface (MPI) solver that uses a finite difference scheme. A spatial discretization is carried out using the second-order centered finite differences. The equations are advanced in time in semi-implicit way [Armenio and Piomelli, 2000]. Over the years, the code has been validated and used in a wide class of problems (see for example Falcomer and Armenio [2002] for an application on complex geometry and Taylor et al. [2005] for an application in the free surface stratified flows). A version of the model (LES-COAST) with ability to handle the real-scale estuarine and coastal hydrodynamic mixing processes has been developed recently (see for example Petronio et al. [2013], Galea et al. [2014]). One of our near-future research activities, which the present activity constitutes the preliminary

step, is to develop suspended sediment transport models to be incorporated in LES-COAST.

2.3 Numerical Method

In the previous section, the equations of motions were presented in the Cartesian framework. However, most of the engineering problems occur over complex, irregular geometries which can not be handled well in the Cartesian coordinate system. One approach to overcome this problem is to employ curvilinear coordinates to transform the computational domain to a rectangular domain.

In LES-COAST, the curvilinear form of equations are solved using a non-staggered-grid layout where the Cartesian velocity components and pressure are defined at the center of the cells and the volume fluxes are defined at the corresponding faces.

Therefore, by considering:

$$\frac{\partial u_i}{\partial x_j} = \frac{\partial u_i}{\partial \xi_k}\frac{\xi_k}{\partial x_j}, \tag{2.15}$$

the system of equations (2.1-2.3) is rewritten in the curvilinear coordinates form as:

$$\frac{\partial U_m}{\partial \xi_m} = 0, \tag{2.16}$$

$$\frac{\partial J^{-1}\overline{u}_i}{\partial t} + \frac{U_m \partial \overline{u}_i}{\partial \xi_m} = -\frac{\partial}{\xi_m}(\frac{\partial J^{-1}\xi_m}{\partial x_i}\overline{p}) - g\delta_{i2} - 2\epsilon_{ijk}\Omega_i\overline{u}_k + \frac{\partial}{\partial \xi_m}(\nu G^{mn}\frac{\partial \overline{u}_i}{\partial \xi_m}) - \frac{\partial \tau_{ij}}{\partial \xi_m}\frac{\partial \xi_m}{\partial x_i}, \tag{2.17}$$

$$\frac{\partial J^{-1}C}{\partial t} + \frac{\partial U_m C}{\partial \xi_m} = \frac{\partial}{\partial \xi_m}(kG^{mn}\frac{\partial C}{\partial \xi_m}), \tag{2.18}$$

where ξ_m indicates transformed coordinates (ξ, η, ζ), J^{-1} is inverse of the Jacobian or the cell volume, U_m is volumetric flux normal to the surface of constant ξ_m and G_{mn} is mesh skewness tensor.

The just mentioned quantities are given by:

$$J^{-1} = \det \frac{\partial x_i}{\partial \xi_j} \tag{2.19}$$

$$U_m = J^{-1}\frac{\partial \xi_m}{\partial x_j}u_j \tag{2.20}$$

$$G_{mn} = J^{-1}\frac{\partial \xi_m}{\partial x_j}\frac{\partial \xi_n}{\partial x_j} \tag{2.21}$$

2.4 Numerical Discretization

The LES-COAST solves the governing equations using a semi-implicit fractional step algorithm, accurate to second order both in space and time [Zang et al., 1994]; it employs the Adams-Bashforth method for the explicit terms and Crank-Nicholson method for the implicit terms (diagonal diffusive terms). Spatial derivatives are approximated with second order central differences, except for the advective terms which are treated by a QUICK scheme (which calculates the face value from the nodal values using a quadratic upwind interpolation) to make the simulation more stable. The discretized form of the equations is as follows:

$$\frac{\delta U_m}{\delta \xi_m} = 0, \tag{2.22}$$

$$J^{-1}\frac{u_i^{n+1}-u_i^n}{\delta t} = \frac{3}{2}(C_i^n + D_E(u_i^n)) - \frac{1}{2}(C_i^{n-1} + D_E(u_i^{n-1}) + R_I(p^{n+1}) + \frac{1}{2}(D_I(u_i^{n+1}+u_i^n)), \tag{2.23}$$

in which $\delta/\delta\xi$ defines the discrete finite difference operator. The quantities C_i (convective terms), R_I (the discrete operator for the pressure gradient terms), D_E(discrete operators representing respectively the off-diagonal viscous term) and D_I(the diagonal viscous terms) are expressed as:

$$C_i = -\frac{\delta}{\delta \xi_m}(U_m u_i), \tag{2.24}$$

$$R_I = -\frac{\delta}{\delta \xi_m}(J^{-1}\frac{\delta \xi_m}{\delta x_i}), \tag{2.25}$$

$$D_I = \frac{\delta}{\delta \xi_m}(\nu G^{mn}\frac{\delta}{\delta \xi_n}), \quad m = n \tag{2.26}$$

$$D_E = \frac{\delta}{\delta \xi_m}(\nu G^{mn}\frac{\delta}{\delta \xi_n}), \quad m \neq n \tag{2.27}$$

The superscripts (such as n) represent the time step and ν is the appropriate variable: $\overline{u}_i^n$.

By applying the fractional step method to Equation 2.23, the time integration of the momentum equation can be carried out where it can be split into two steps called predictor and corrector. LES-COAST model solves the Equation 2.23 by applying the fractional step method for each iteration.
In the fractional method, the predictor step is concerned with the time advancement of the advective and diffusive transport of momentum for an

unphysical velocity u^*, as:

$$(1-\frac{\Delta t}{2J^{-1}}D_I)(u_i^*-u_i^n)=\frac{\Delta t}{J^{-1}}[\frac{3}{2}(C_i(\overline{u}_i^n))+D_E(\overline{u}_i^n))] \\ -\frac{1}{2}(C(\overline{u}_i^{n-1}))+D_E(\overline{u}_i^{n-1}))+D_I(u_i^n)]; \quad (2.28)$$

Afterwards, the corrector step adjusts the flow-field considering the pressure gradient. In this step, u_i^{n+1} is calculated from the intermediate velocity u^* such that the continuity equation is satisfied. From Equation 2.23 and Equation 2.28 the terms u_i^{n+1} and u^* are related to the pressure gradient by:

$$u_i^{n+1}-u^*=\frac{\Delta t}{J^{-1}}[R_I(\phi^{n+1})], \quad (2.29)$$

in which , the term ϕ satisfies the following relation:

$$R_I(p)=(J^{-1}-\frac{\Delta t}{2}D_I)(\frac{R_I(\phi)}{J^{-1}}). \quad (2.30)$$

Interpolation of Equation 2.29 on the cell face yields:

$$U_m^{n+1}=U_m^*-\Delta t(G^{mn}\frac{\delta\phi^{n+1}}{\delta\xi_n}), \quad (2.31)$$

where $U_m^*=J^{-1}(\delta\xi_m/\delta\xi_j)u_j^*$ is called the intermediate volume flux.

By replacing Equation 2.31 into Equation 2.22 the Possion equation for the pressure ϕ^{n+1} is obtained as:

$$\frac{\delta}{\delta\xi_m}(G^{mn}\frac{\delta\phi^{n+1}}{\delta\xi_n})=\frac{1}{\Delta t}\frac{\delta U_m^*}{\delta\xi_m}. \quad (2.32)$$

It should be noted that as Zang et al. [1994] indicated for solving the N-S equations on a non-staggered grid, the pressure p and velocity components u_i are defined on the cell center while the intermediate volume fluxes U_i are defined on the cell faces.

Chapter 3

Large Eddy Simulation of two-way Coupling Sediment Transport[1]

In the present chapter numerical simulations are used to investigate suspended sediment transport and its effect on the dynamics of the turbulent boundary layer. We use an Euler-Euler methodology based on single-phase approach. Large eddy simulation is employed to resolve the large scales of motion, whereas the contribution of the small scales is parametrized by the use of a dynamic Smagorinsky model. In order to account for sediment-induced buoyancy on momentum, a buoyancy term is considered in the three-dimensional Navier-Stokes equations through the use of the Boussinesq approximation. We consider four sediment sizes and the simulations are performed for both one-way and two-way coupling approaches to gain a better description of sediment-turbulence interaction. The level of stratification for each particle size is qualified by the bulk Richardson number which increases by decreasing the grain size.

This chapter is structured as follows: Section 3.1 presents a general introduction to the topic with a review on the previous studies. Section 3.2 provides a detailed discussion of the governing equations together with the relevant non-dimensional parameters and of the numerical method. This is followed by a description of the boundary conditions in Section 3.3. The simulation parameters are given in Section 3.4. The simulation results are presented in Section 3.5. Finally, concluding remarks are given in Section 3.6.

[1] Published in Advances in Water Resources 81, DOI: 10.1016/j.advwatres.2014.12.004

3.1 Introduction

Prediction of sediment transport in turbulent flows is one of the most complex issues in environmental engineering. A number of critical problems like bed deformation, sedimentation in reservoirs and some kinds of pollutant dispersion in marine environments are associated to sediment suspension and transport. The erodible bed is typically mobile under the flowing fluid which has sufficient strength to initiate general motion of uppermost particles of the bed. In bed load mode, where particles are moved along the channel bed by rolling, sliding or saltation, the result is generally bed morphology changes such as ripple or dunes which cause a complex interaction with flow. When sediments are very small, they are suspended in the water column and travel horizontally along length scales much larger than the vertical one [Metha, 2013]. Suspension of polluted sediments has also long-term/long-range ecological impacts on coastal and fresh water environments. It may lead to transport of organic and inorganic matters and nutrients from one area to another hence modifying water quality characteristics [Wetzel, 2001, Weyhenmeyer, 1996].

Several researchers addressed the problem of numerical modelization of sediment transport in coastal engineering and related areas. Depending on how sediments are treated in the flow field, the numerical models for two-phase transport are classified as Euler-Lagrange and Euler-Euler. The Euler-Lagrange approach is frequently used when the second phase occupies a low fraction of total volume. The fluid is treated as continuum and ruled by Navier-Stokes equations, while the dispersed phase is described by the equation of motion for each particle. This approach has shown to be able to describe the behavior of the particles, which selectively respond to the turbulent time-scales, depending on their own characteristic time-scale (the latter being related to the particle's inertia) (see Armenio and Fiorotto [2001] and literature therein cited for a discussion). Also, the Euler-Lagrange approach is able to reproduce the increase of the particle free-fall velocity due to the presence of turbulence (among the others, see the seminal paper by Wang and Maxey [1993]). However, tracking large number of particles through flow field is not practical in engineering problems.

The Euler-Euler approach, in which the governing equations for both phases (momentum and sediment concentration) are derived according to the continuum approximation, is more appropriate for engineering applications. Euler-Euler methods can be distinguished into two main classes, namely two-phases and single phase models.

The two-phase approach (see among the others Hsu [2003]) is more general and valid even when the sediment concentration is large; it consists in solving mass and momentum conservation equations for both phases, namely the liquid one and the sediment concentration one. The regions occupied by the two phases are ruled by a mass fraction coefficient and coupling between

phases is modeled through interaction forces like drag, lift and fluctuating pressure force [Teisson et al., 1993].

The single phase approach, in which a single set of conservation equations is solved for the mixture, is mainly valid for fine particles in suspension. Sediment transport is accounted for through the use of an advection-diffusion equation for sediment concentration. According to Uittenbogaard [1994], this assumption holds if the settling velocity of particles is much smaller than the vertical turbulent velocity fluctuations ($v_s \ll v_{RMS}$). This model is valid under the restriction which limits the diameter of particles to the smallest dynamic length-scale of turbulence [Villaret and Davies, 1995, Zedler and Street, 2001]. As discussed by Winterwerp [2001] the condition for single-phase approach is generally met in coastal problems characterized by the presence of fine sediments having settling velocity of order $0.1 - 2mm/s$, which is smaller than the vertical velocity fluctuations.

In a single-phase, Euler-Euler model, the dispersed phase follows the flow movement except for the vertical settling velocity which is parametrized by means of empirical or analytical formulations. In this simplified model, the feedback effect of particle concentration on momentum is usually not considered. In order to take into account for the influence of the suspended particles on the mean flow, a two-way coupling approach must be employed, meaning that the feedback effect of sediment concentration on momentum transport needs parametrization. Among the others, buoyancy effects associated to the space-time variation of the mixture density due to suspended sediment concentration can be considered taking advantage of the general theory of stable stratified flows. A state equation which defines the density variation is added to the governing equations and an-extra term appears in the momentum equations to model buoyancy effects (see, for instance, Guo and Julien [2001]).

Over the years, numerous laboratory and theoretical studies have been performed for the analysis of sediment-laden flows. Experimental investigations of particle suspension effects on the velocity profiles were first carried out by Vanoni [1946], Enstein and Chien [1955] and Elata and Ippen [1961]. They observed a decrement of the von Kàrmàn constant as suspended sediment concentration increases. In their experiments no deposition on the bed was allowed. Vanoni [1946] argued that turbulence is damped due to the buoyancy effect induced by suspended sediments. Gelfenbaum and Smith [1986] verified the experiments of Vanoni [1946] by a semi analytical approach which is based on the use of an empirical eddy diffusivity. He concluded that a damping effect of sediment suspension should be included in the model to reproduce the experimental data.

Coleman [1986] established a new point of view in interpretation of the effect of suspended sediments on the velocity distribution in open-channel flows. He argued that the velocity profile is controlled by the law of wake in water column and the logarithmic part which is considered by Vanoni

[1946] is limited to the lower 20% of water column. He concluded that the von Kàrmàn constant is independent on suspended sediment concentration. Lyn [1988] proposed a similarity approach for sediment-laden flows in which two different concentration scales characterize the concentration profile in the inner and outer region respectively, whereas the velocity profile is characterized by a single scale common to both regions. His experimental results for the velocity profile clarified that for a range of laboratory conditions, the effect of sediment was confined to the near wall region.

Muste and Patel [1997] used discriminator laser-Doppler velocity (DLDV) in open channel flow for velocity measurements with and without suspended sediments with diameter ranging from $0.21 - 0.25\ mm$. In the experiments, the range of sediment volumetric concentration was found in the range $10^{-3} - 10^{-4}$. The authors found the mean sediment velocity to be smaller than that of water, although the difference was not as significant as in Coleman [1986] and Lyn [1988]. A slight decrease of streamwise velocity fluctuations and a significant decrease of vertical velocity fluctuations for sediment phase were observed when comparing with clear water fluctuations.

In subsequent experiments, Muste et al. [2005] determined the interactions between suspended particles and flow turbulent structures. They found that particles extract turbulent kinetic energy from the flow. They observed a gradual reductions of the von Kàrmàn constant with addition of particles, irrespective of their density.

An experimental study was performed by Cellino and Graf [1999] to investigate sediment-laden flow under capacity and non-capacity condition. The capacity condition is defined as the maximum sediment load that a flow can transport. Under this condition a layer of particles, composed of the same particles as are in suspension, appears on the bed. For both cases, to describe the vertical concentration distribution, they used the Rouse equation which is derived by assuming a parabolic eddy-viscosity profile. Specifically, they focused on the experimental determination of the β factor appearing in the Rouse number $y = v_s/\beta\kappa u_\tau$ where v_s is settling velocity of sediments, κ is von Kàrmàn constant and u_τ is the shear velocity. They found that, with small particles ($d \simeq 0.1\ mm$), the β values at capacity condition are smaller than unity. Analyzing the power spectral density function of the turbulent kinetic energy, they found a decrease of power density in the region of low frequencies due to the presence of suspended particles. They also showed that the vertical velocity fluctuations of sediment-laden flow decrease continuously with increasing suspended concentration and also gave an explanation for the damping effect of solid suspended particles on the turbulence of flow.

Guo and Julien [2001] carried out a theoretical analysis in sediment-laden flow and considered the effect of suspension on turbulence in terms of governing equations. The authors showed that sediment suspension causes an increment of the mean flow energy loss and affects the velocity profile due to

the presence of concentration and density gradient. Winterwerp [2001] studied stratification effects of sediment suspension of cohesive and non-cohesive particles with a one-dimensional vertical (1DV) numerical model. Comparison of the non-cohesive particle results with experimental data of Gust [1984], clarified that the velocity profile modification is caused by sediment-induced buoyancy term in the turbulent kinetic energy equation.

Despite extensive studies of suspended sediment transport and turbulence-sediment interaction, few numerical investigations survey the effect of suspension on both mean flow and concentration profile. Further, the effect of suspended sediment concentration on the turbulent field has still to be completely clarified. The aim of the present research is twofold: 1) We study the effect of suspended sediments on the dynamics of turbulent flow field and quantify the effect of variation of sediment size on the hydrodynamic and concentration fields; 2) We compare the results of two different Euler-Euler, single-phase modelizations to identify their own range of validity: the first one where buoyancy effects on momentum are neglected (henceforth denoted as one-way coupling); the second one where buoyancy effects on momentum are considered (henceforth denoted as two-way coupling).

We employ Euler-Euler single-phase approach, which considers the two phases as a mixture. As previously discussed, in the case of low volumetric sediment concentration and settling velocity much smaller than vertical velocity fluctuation, the single phase approach can be used. We use the Boussinesq approximation of the Navier-Stokes equations to account for sediment induced buoyancy effects. This approach is widely in use for the analysis of stratified flows and applies when the density variations in the field are much smaller than the bulk density of the flow. According to this approach the feedback effect of concentration on momentum occurs through a modified gravity term. This is the methodology adopted in the present study.

The simulations are carried out for different particle sizes in a range of $0.1 - 0.65\ mm$. To verify the effect of mutual interaction between the two phases through buoyancy, the statistics of the flow field will be discussed for both one-way and two-way coupling cases.

3.2 Mathematical Method

3.2.1 Governing Equations

Considering the Euler-Euler single-phase approach, the flow field obeys the 3-dimensional Navier-Stokes equations for incompressible flows, while the advection-diffusion equation describes the transport of sediment concentration in the flow domain as scalar quantity. The Boussinesq approximation for buoyancy effects is applied. We use LES, in which the large, anisotropic and energy-carrying scales of motion are directly solved through an unsteady,

three-dimensional numerical simulation; the small, more isotropic and dissipative scales are modelled by means of a subgrid-scale (SGS) closure.

Recalling the earlier discussion in Section 2.2, application of a filter (denoted by the over-bar) to conservation equations gives:

$$\frac{\partial \overline{u}_i}{\partial x_i} = 0, \tag{3.1}$$

$$\frac{\partial \overline{u}_i}{\partial t} + \frac{\partial \overline{u}_i \overline{u}_j}{\partial x_j} = \frac{1}{\rho_0}\Pi - \frac{1}{\rho_0}\frac{\partial \overline{p}}{\partial x_i} - g_m \delta_{i2} + \nu \frac{\partial^2 \overline{u}_i}{\partial x_j \partial x_j} - \frac{\partial \tau_{ij}}{\partial x_j}, \tag{3.2}$$

where u_1, u_2 and u_3 (or u, v and w) are the velocity components in the stream-wise x_1 (or x), vertical upward x_2 (or y) and span-wise x_3 (or z) directions, Π is an imposed pressure gradient driving the flow, p is the hydrodynamic pressure, ρ_0 is the density of the fluid, g_m is the modified gravity (defined later on) and ν is the kinematic viscosity of the fluid. The effect of unresolved velocity field to the resolved large scales of motion is accounted for in τ_{ij}.

Similarly, filtering the scalar transport equation for suspended sediments yields:

$$\frac{\partial \overline{C}}{\partial t} + \frac{\partial}{\partial x_j}[(\overline{u_j} - v_s \delta_{j2})\overline{C}] = \frac{\nu}{\sigma}\frac{\partial^2 \overline{C}}{\partial x_j \partial x_j} - \frac{\partial \chi_j}{\partial x_j}, \tag{3.3}$$

where C is the sediment concentration. σ is the Schmidt number assumed to be 1 as in Kraft et al. [2011] and v_s is the sediment settling velocity; The term χ_j represents the contribution of the unresolved scales to the resolved concentration fluxes.

As mentioned before, to account for the effects of sediment concentration on the flow field, we consider the modified gravity in Navier-Stokes equations. We account for weak density variations in buoyancy effects through the Boussinesq approximation. Therefore, we retain density variations in the buoyancy term in the vertical direction of the momentum equation. We define the buoyancy coefficient as:

$$c_b = \frac{\rho_s - \rho_0}{\rho_0} C, \tag{3.4}$$

where ρ_s and ρ_0 are sediment and clear-water density, respectively. Thus, the modified gravity is obtained as [Teisson et al., 1993, Winterwerp, 2001]:

$$g_m = g c_b, \tag{3.5}$$

in which g is gravitational acceleration. When Eqs. 3.4 and 3.5 are used in the LES context, instantaneous filtered values must be considered for C and g_m.

The SGS turbulent fluxes for sediment concentration ($\chi_j = \overline{u_j C} - \overline{u}_j \overline{C}$) are expressed as:

$$\chi_j = -k_{sgs} \frac{\partial \overline{C}}{\partial x_j}. \tag{3.6}$$

Here k_{sgs} is the SGS concentration diffusivity obtained dynamically using the procedure described in Armenio and Sarkar [2002].

In LES, filtering implies removing out the SGS contribution from the total fluctuating field. If the symbols $'$ and $''$ respectively denote total and resolved fluctuations, for a generic turbulent quantity R, its fluctuation can be written as:

$$R'(x_i, t) = R''(x_i, t) + R_{sgs}(x_i, t). \tag{3.7}$$

The quantity $R_{sgs}(x_i, t)$ by itself is unknown, but the SGS contributions to the turbulent momentum and concentration fluxes are known, so that, for the total fluxes we can write:

$$\begin{aligned} < u_i' u_j' > &= < u_i'' u_j'' > + \tau_{ij} \\ < C' u_j' > &= < C'' u_j'' > + \chi_j. \end{aligned} \tag{3.8}$$

Hereafter, when discussing second-order statistics, we refer to total quantities, sum of the resolved one and the SGS one.

For sediments with mean diameter d in the range of $0.1 - 1\ mm$, the settling velocity v_s is estimated by using the formulation of Zanke [1977] which considers the balance between gravitational force and drag resistance of a particle moving in a fluid otherwise at rest:

$$v_s = \frac{10\nu}{d}[(1 + \frac{0.01(s-1)gd^3}{\nu^2})^{0.5} - 1], \tag{3.9}$$

where $s = \rho_s/\rho_0$ is the specific gravity of suspended sediments. For sand particles smaller than about $0.1\ mm$ (Stokes-range) the settling velocity is better described by:

$$v_s = \frac{1}{18} \frac{(s-1)gd^2}{\nu}. \tag{3.10}$$

According to the sediment size considered, we apply the correspondent formulation in our simulations.

3.2.2 Non-dimensional parameters

In stratified shear flows, the gradient Richardson number has been largely used to assess the stability of the flow. In a one-directional flow, it is defined as:

$$Ri_g = \frac{N^2}{S^2} = \frac{-\frac{g}{\rho_0}\frac{\partial\langle\rho\rangle}{\partial y}}{(\frac{\partial\langle u\rangle}{\partial y})^2}, \tag{3.11}$$

where N is the buoyancy frequency and S stands for the mean vertical shear. The symbol $\langle . \rangle$ denotes Reynolds averaging as defined in Section 4. Considering the effect of concentration on the density distribution, we have:

$$\rho = \rho_0 + (\rho_s - \rho_0)C. \tag{3.12}$$

By using Equation 3.12 in Equation 3.11, we get:

$$Ri_g = \frac{sg\frac{\partial\langle C\rangle}{\partial y}}{(\frac{\partial\langle u\rangle}{\partial y})^2}. \tag{3.13}$$

Values of Ri_g larger than $0.2 - 0.25$ indicate very stable conditions where high stratification inhibits mixing because of the strong restoring buoyancy force.

A parameter which quantifies the level of stratification in the flow is the bulk Richardson number:

$$Ri_b = \frac{\Delta\rho g\delta}{2\rho_0 u_b^2}, \tag{3.14}$$

where $\Delta\rho$ is the density variation over the channel height δ. Using Equation 3.12, we obtain:

$$Ri_b = \frac{sg\delta}{2u_b^2}\Delta C, \tag{3.15}$$

where $u_b = 1/\delta \int_0^\delta u \; dy$ and $\Delta C =< C_{ref} > - < C_{fs} >$ is the concentration difference between the bottom and the free surface of the channel. In sediment-laden flows the mixing efficiency is represented by the turbulent Schmidt number σ_t which is the ratio between the vertical momentum and scalar fluxes as:

$$\sigma_t = \frac{\nu_t}{k_t}, \tag{3.16}$$

where ν_t and k_t are the turbulent momentum and concentration diffusivities respectively. Assuming uni-directional shear flows, ν_t and k_t are defined using the gradient-transport hypothesis as:

$$\nu_t = -\frac{\langle u'v'\rangle}{\partial\langle u\rangle/\partial y}, \tag{3.17}$$

$$k_t = -\frac{\langle C'v'\rangle}{\partial\langle C\rangle/\partial y}. \tag{3.18}$$

3.3 Boundary Condition for the Concentration

A critical issue in sediment transport modeling is the definition of the appropriate boundary conditions for the concentration. While solving the governing equations, two types of boundary conditions need to be prescribed, namely at the free surface and at the bottom surface. At the free surface, the net instantaneous vertical flux must be zero, that is:

$$v_s\overline{C} + \frac{\nu}{\sigma}\frac{\partial\overline{C}}{\partial y} = 0. \tag{3.19}$$

The bottom boundary condition may be prescribed in two ways, namely assigning the reference concentration or the sediment net flux. A wide variety of expressions exist in literature for predicting the near-bed reference concentration of suspended sediments. In this study, the expression for reference concentration is that given by Smith and Mclean [1977] and reads:

$$\overline{C}_{ref} = C_0\frac{\gamma_0\overline{S}_0}{1+\gamma_0\overline{S}_0}, \tag{3.20}$$

with

$$\overline{S}_0 = \frac{\overline{\tau}_w - \tau_{cr}}{\tau_{cr}}, \tag{3.21}$$

where $\gamma_0 = 2.4 * 10^{-3}$ is a constant and $C_0 = 0.65$ is the maximum permissible concentration for single-grain spherical sediments. The reference concentration is a function of the instantaneous bed shear stress ($\overline{\tau_w}$) and the critical bed shear stress (τ_{cr}). When the bed shear stress exceeds the critical value, the sediments are eroded from the bottom surface and suspended into the flow field. Conversely, when the bed shear stress is smaller than the critical value, erosion is absent. The quantity C_{ref} quantifies the ability of the flow to carry in suspension sediments placed at the bed. As will be discussed later, it decreases with the increase of the sediment size. Equation 3.20 is one among the possible choices available in literature (see Amoudry [2008] for a review on the subject). The advantage of the Smith and McLean formula used in the present study consists in the presence of a maximum available concentration equal to 0.65. The presence of such an upper limit is consistent with the physics of suspended single-grain sediments.

Although the Shields diagram slightly underestimates the critical bed shear stress in the region of suspended transport, for simplicity in the present paper we use values obtained from Shields curve. It establishes a relationship between the critical Shields parameter $\theta_{cr} = \tau_{cr}/(\rho_s - \rho_0)gd$ and the non-dimensional particle size d^+. For suspended sediment transport, a third dimensionless parameter in the Shields diagram (Figure 3.1) can be introduced as [Vanoni, 2006] :

$$S_s = \frac{d}{\nu}[0.1((\frac{\rho_s}{\rho_0} - 1)gd)]^{0.5}, \tag{3.22}$$

which depicts as a family of inclined parallel lines (dashed lines in Figure 3.1); each line corresponds to a constant value of the parameter S_s. A particular set of flow/sediment configuration is represented by a point along the inclined lines. The intersection of such lines with the Shields curve yields the critical stress value. The distance of the point from the Shield curve provides an indication of flow potential to transport sediment in suspension. The flow conditions analyzed in the present study are denoted by cross symbols in Figure 3.1. The instantaneous bed shear stress is computed by:

$$\overline{\tau}_w = \sqrt{\overline{\tau}_x^2 + \overline{\tau}_z^2}, \tag{3.23}$$

where $\overline{\tau}_x$ and $\overline{\tau}_z$ are the instantaneous bed shear stress components in stream-wise and span-wise directions respectively.

3.4 Simulation Parameters

In the present work we consider an archetypal problem, namely sediment suspension in a turbulent open channel flow. The flow develops between two infinite horizontal planes, a solid one at the bottom and a shear-free surface at the top, the latter mimicking the presence of a free-surface in absence of waves. The flow is driven by a constant pressure gradient Π which yields a shear velocity $u_\tau = \sqrt{\tau_w/\rho_0} = \sqrt{\delta\Pi/\rho_0} = 0.01m/s$. This gives a friction Reynolds number of $Re_\tau = u_\tau\delta/\nu = 600$ and a Froude number of $Fr = u_{av}/\sqrt{g\delta} = 0.2$. We perform a wall-resolving LES, meaning that we directly solve the near-wall layer up to the wall without using a wall layer model. The channel has dimensions 5δ and 2.5δ in stream-wise and span-wise directions, respectively, where $\delta = 0.06\ m$ is the channel height. The spatial resolution of grid cells is $N_x * N_y * N_z = 64 * 32 * 64$. The grid is not uniform in the wall normal (vertical) direction. The grid we use gives $\Delta x^+ = 46$, $\Delta z^+ = 23$ and $\Delta y^+ = 1$ at the first grid point off the wall [2]; in the wall-normal direction 5 grid points are placed within $\Delta y^+ = 10$. The grid spacing and the point distribution in the wall-normal direction satisfy the requirements for wall-resolving LES.

Periodic boundary conditions are imposed along the horizontal directions allowing reproduction of a laterally unbounded flow, a free-slip b.c. is imposed at the top surface and no-slip condition is applied at the channel bed. In order to assess the effect of buoyancy, the non-dimensional grain sizes are chosen as $d^+ = u_\tau d/\nu = 1, 3, 5, 6.5$ and the sediment density is

[2] the index $^+$ denotes quantities made non-dimensional with the wall-unit ν/u_τ

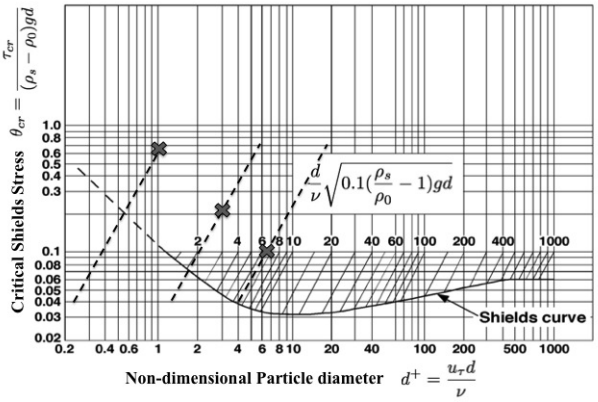

Figure 3.1: Shields diagram (after Vanoni [2006]). The dashed lines represent the values of parameter S_s for our study and cross symbols mark the position of the present test cases with $d^+ = 1, 3, 6.5$.

$\rho_s = 2650 kg/m^3$. The cases with $d^+ = 1, 3$ and 6.5 are plotted in Figure 3.1 as cross symbols. We are aware that most particle diameters are larger than the near-wall cell size used in the simulations. However we recall here that we are not using a Lagrangian particle model, rather we use a continuum Eulerian model for the sediments, and the diameter must be considered as a quantity ruling the Shields parameter and the terminal fall velocity of the concentration C.

For cases $d^+ = 1, 3, 5$ and 6.5, we calculate the settling velocity through Equation 3.9 and for $d^+ = 1$ Equation 3.10 is applied. Morphological effects are not considered in the present work. The initial sediment concentration in the flow is set to zero. Simulations are run up to the development of a statistically steady state and then continued to accumulate statistics. As mentioned, statistical quantities are calculated Reynolds averaging in time and over the $x - z$, horizontal planes of homogeneity:

$$\langle R \rangle(y) = \frac{1}{T\ l_x\ l_z} \int \int \int \overline{R}(x, y, z, t) dx\ dz\ dt, \tag{3.24}$$

where R is a generic turbulent quantity.

3.5 Results

3.5.1 Mean Field

The mean properties of the flow field are discussed in this section. We first discuss saturated sediment concentration profiles defined as the balance between sedimentation by gravity and diffusion by turbulence [Rouse, 1937]. The concentration profile is analyzed over two main steps. First we discuss

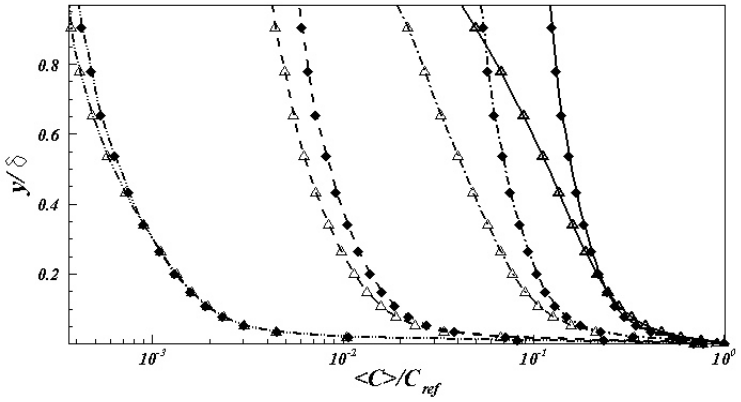

Figure 3.2: The normalized vertical profile of averaged sediments concentration for 4 different particle sizes. $d^+ = 1$: solid line, $d^+ = 3$: dashed dot line, $d^+ = 5$: dashed line, $d^+ = 6.5$: dashed dot dot line; One-way coupling simulation (diamond); two-way coupling simulation (delta).

the variation of the concentration profile along the channel height. Afterward, we focus on the effect of grain sizes on the suspended concentration for each pair of one-way and two-way coupling cases.

The Reynolds averaged form of the sediment concentration equation reads:

$$k\frac{\partial < C >}{\partial y} - < C'v' > + < C > v_s = F_c, \tag{3.25}$$

where F_c is the concentration flux at the wall, which is a negative quantity (Table 3.1). On the left hand side (LHS) of Equation 3.25 the concentration flux is composed of three terms, namely the sediment diffusive flux (negative quantity), the turbulent one (positive quantity) and the deposition contribution $< C > v_s$ (negative quantity). The sum of the absolute values of the three terms on the LHS balances the absolute value of the term on the right hand side (RHS). As a result of the analysis of the terms of Equation 3.25 the larger the deposition flux is the smaller the sum of the diffusive and turbulent fluxes is. We first discuss the one-way coupling cases, where the buoyancy effect associated to sediment concentration is neglected.

Close to the wall, the turbulent flux is negligible compared to the diffusive one and we observe a steep slope of the concentration profile which is partially compensated by the deposition flux which is large close to the wall. Moving upward, the turbulent flux gets more relevant and deposition and molecular fluxes get smaller and smaller. The no-flux boundary condition prevents the upward flux at free surface. The described behavior is common to all concentration profiles depicted in Figure 3.2.

As the particle diameter decreases, (Figure 3.2 from left to right, lines with diamond symbol), the ability of the flow field to erode sediments from

the bed increases. As shown in Equation 3.9Equation 3.10, the settling velocity is proportional to the second power of particle diameter. Larger particles experience a larger settling force (Table 3.1), which leads to larger deposition. In contrast, small settling velocity will allow particles to stay in suspension. The total deposition term ($< C > v_s$) is not the only relevant term in establishing the net suspension amount. The erosion rate from the bed channel, quantified by C_{ref}, also has a crucial role in this balance. Comparing particles by size, from the biggest ($d^+ = 6.5$) to the smallest ($d^+ = 1$), we observe enhancement of available sediment concentration in the water column (see Table 3.1). In summary, the concentration profile is strongly sensitive to the variation of the particle size and a smaller value of the particle diameter results in higher concentration level and larger suspended load.

When mutual interaction between concentration and momentum is considered through the buoyancy term in Equation 3.2, the concentration profiles change compared to the previous (one-way coupling) cases. For each particle size, the two-way coupling profile is shown in Figure 3.2 by delta symbols. Equation 3.25 remains unchanged although the redistribution of the three terms on the LHS varies due to stratification effects (see Table 3.1). Specifically, since the turbulent concentration flux (shown in subsection 3.5.2) decreases with the reduction of the sediment diameter, the sediment diffusion flux must increase (as absolute value being it negative) thus reducing the concentration upward and consequently reducing the deposition process. Overall, the amount of suspended concentration in the flow column appears reduced compared to the non-stratified case. This effect is well observable when the non-dimensional diameter of sediments is smaller than 3.

To identify the density variation level by a single value, each particle size is represented by the corresponding bulk Richardson number (see Table 3.1). For the largest particles ($Ri_b = 0.028$) the concentration profile is nearly insensitive to buoyancy effects. This has to be attributed to the fact the deposition term is large and the available sediment concentration C_{ref} is small. As a result the concentration of sediments moving out of the wall region is very small and the feedback effect on momentum through buoyancy is negligible. As the sediment size decreases ($Ri_b = 0.031$, see Figure 3.2), the difference between one-way and two-way coupling cases is approximately constant along the channel height except near the wall region. This because concentration is not negligible in the wall region due to the reduced deposition term (Table 3.1), thus producing buoyancy effects on momentum. However, moving out of the wall, concentration remains small and the buoyancy effect is negligible. By further decreasing the particle size ($Ri_b = 0.038$ and 0.041), the difference between one-way and two-way coupling gets relevant. This happens because of the combination of large available concentration C_{ref} and small deposition term (Table 3.1); particle

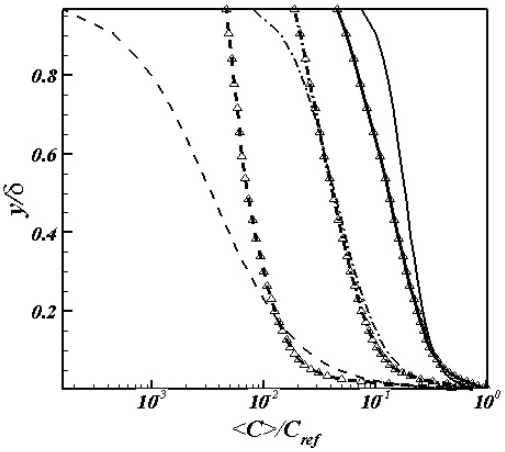

Figure 3.3: Two-way coupling sediments concentration profiles (delta) and Rouse equation (no symbol) for different particle sizes. $d^+ = 1$: solid line, $d^+ = 3$: dashed dot line, $d^+ = 5$: dashed line ; Rouse fitted profile, $\beta = 0.1$:solid line, $\beta = 0.38$:dashed dot line, $\beta = 0.6$:dashed line.

concentration penetrates more and more in the fluid column thus giving rise to detectable buoyancy effects. The increasing buoyancy penetration effect with reduction of sediment diameters can be clearly visualized plotting the vertical distribution of the gradient Richardson number for the three cases (Figure 3.4).

According to Armenio and Sarkar [2002] two regions may be detected: for $Ri_g \preceq 0.2$ (*buoyancy-affected* regime), turbulence is active but reduced due to stratification effects; for $Ri_g \succeq 0.2$, (*buoyancy-dominated* regime), turbulence is suppressed and internal gravity waves may be generated. In Figure 3.4 it clearly appears that decreasing the particle size (increasing Ri_b) gives an increase of Ri_g along the fluid column, indicating enhancement of stable stratification effects in wider and wider regions of the fluid column. The buoyancy dominated regime practically occurs for $Ri_b = 0.041$ only, in a small region far from the wall. In this case sediment-induced buoyancy may significantly affect the flow.

In classical studies of sediment transport, the vertical profile of mean concentration is expressed though the theoretical Rouse profile, already mentioned in Section 3.1:

$$\frac{C}{C_{ref}} = (\frac{\delta - y}{y} . \frac{a}{\delta - a})^{\alpha}; \ \alpha = \frac{v_s}{\beta \kappa u_\tau}, \tag{3.26}$$

where the reference concentration C_{ref} is calculated at elevation a and α is the Rouse number. The parameter β, which relates sediment and momentum diffusion coefficients is generally assumed to be 1. The theoretical expression has been found for high values of Re where turbulence is not affected by viscous effects and assuming turbulent diffusivity of the concen-

Table 3.1: Bulk Richardson number Ri_b, non-dimensional settling velocity v_s, mean reference concentration$< C_{ref} >$, concentration flux F_c and deposition term $(< C_{ref} > v_s)$ for different particle sizes at wall, where $Ri_b = 0$ stands for one-way coupling approach.

	$d^+ = 1$		$d^+ = 3$		$d^+ = 5$		$d^+ = 6,5$	
	$Ri_b = 0$	$Ri_b = 0.041$	$Ri_b = 0$	$Ri_b = 0.038$	$Ri_b = 0$	$Ri_b = 0.031$	$Ri_b = 0.$	$Ri_b = 0.028$
v_s/u_τ	$8.7 * 10^{-3}$	$8.7 * 10^{-3}$	$7.7 * 10^{-2}$	$7.7 * 10^{-2}$	0.22	0.22	0.33	0.33
$< C_{ref} >$	0.42	0.38	0.39	0.36	0.32	0.32	0.29	0.29
F_c/u_τ	-0.075	-0.051	-0.155	-0.128	-0.242	-0.241	-0.309	-0.310
$(< C_{ref} > v_s)/u_\tau$	$-3.65 * 10^{-3}$	$-3.3 * 10^{-3}$	-0.03	-0.027	-0.072	-0.071	-0.0957	-0.0957

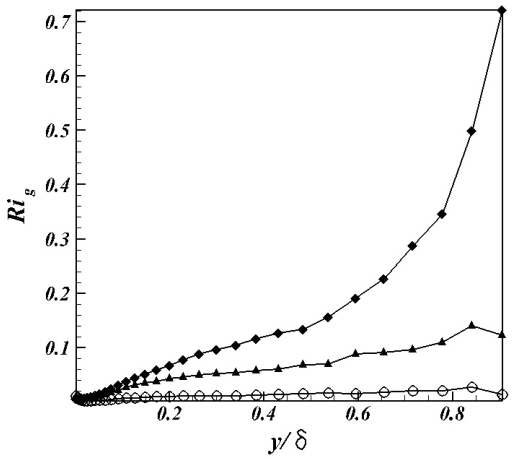

Figure 3.4: Vertical profile of gradient Richardson number for three stratification levels, diamond: $Ri_b = 0.041$, delta: $Ri_b = 0.038$, circle: $Ri_b = 0.031$.

tration constant along the depth.

Here we place our results for two-way coupling approach within the Rouse equation context. As done by Muste et al. [2005], we vary the parameters of the Rouse equation to fit the numerical results. The reference height appearing in Equation 3.26 is chosen to be at the first centroid off the wall and the parameter β varies between 0.1 and 0.6. The profiles are shown in Figure 3.3. For smaller sediments (larger volume concentration in the water column), the fit is fairly good. As sediments concentration decreases in the water column ($d^+ = 5$) the Rouse-fitted profile substantially differs from simulated data. This is reasonable since larger particles are more likely transported according to the bed-load mode and hence, the Rouse formula, which describes suspended mode transport, may be not suited. The need to use values of β smaller than the canonical one may be related to Reynolds number effects and to the assumption of constant turbulent diffusivity of sediment concentration along the depth [Muste et al., 2005].

Here we discuss the effect of sediment concentration on the velocity field. Interaction of suspended particles with the underlying turbulent flow

changes the dynamic behavior of flow because more variables like the sediment concentration and density gradient are involved in sediment-flow system. The comparison of stream-wise mean velocity profiles obtained by the two-way coupling model with the passive scalar (one-way) case is shown in Figure 3.5. In the passive scalar case the velocity profile is unaltered changing sediment size from case to case. This obviously happens because concentration does not interact with the velocity field in the momentum equation. In the two-way coupling case, it is observed that in presence of sediments, the vertical profile of stream-wise velocity is modified by buoyancy effects. From studies of suspended sediment transport as well as of stratified wall-bounded turbulence, it is known that turbulence is damped by density gradients [Vanoni, 1946, Muste and Patel, 1997, Cellino and Graf, 1999, Armenio and Sarkar, 2002]. In particular, the correlation between vertical and stream-wise velocity fluctuations is reduced by the presence of stratification. Accordingly, vertical momentum transport is suppressed compared to the passive scalar case. In the flow herein investigated, the total mean shear stress is independent on stratification and varies linearly from the maximum value at the wall (τ_w) to the value 0 at the free-surface. It is composed of two contributions in the Reynolds-averaged equation; the Reynolds shear stress and the viscous mean shear stress:

$$\tau(y) = - < u'v' > + \nu \frac{\partial \langle u \rangle}{\partial y} = \tau_w (1 - \frac{y}{\delta}). \tag{3.27}$$

To keep the total shear stress in balance, the mean velocity gradient must increase when the Reynolds shear stress decreases for stratification effects (see Figure 3.6a in subsection 3.5.2). This increase is more significant for the smallest particle ($Ri_b = 0.041$), namely for large buoyancy effects. For the largest particles ($Ri_b = 0.031$), Ri_g is small along the fluid column and hence the mean velocity profile does not show any observable change comparing to one-way coupling model. As quantified by the vertical distribution of Ri_g, this is due to the fact that the concentration gradient level is not strong enough to alter the vertical distribution of the Reynolds shear stress. For larger values of Ri_b corresponding to smaller sediment diameters, Figure 3.5 shows a decrease of the von Kàrmàn constant associated to the increase of suspended particles in the flow. This result agrees with the findings of Vanoni [1946], Muste and Patel [1997], Gelfenbaum and Smith [1986]. The decrease of κ is a consequence of the increased mean velocity gradient.

To summarize, reduction of sediment size produces larger suspension in the flow field. This happens because the available concentration at the wall increases and at the same time the deposition term decreases. This large suspension causes a reduction of the Reynolds shear stress and thus the increase of flow velocity which reflects on the decrease of the von Kàrmàn constant. By the other side, buoyancy effects increase the vertical concentration gradient due to a strong decrease of the turbulent concentration flux

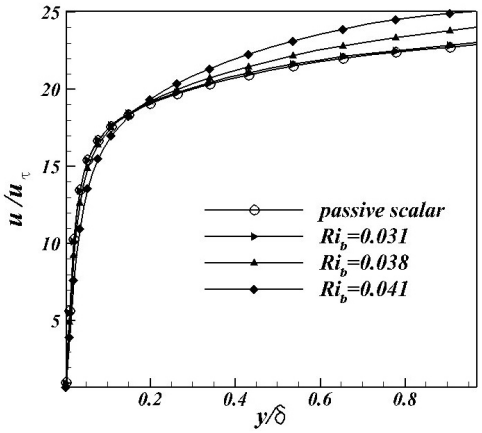

Figure 3.5: Vertical profile of averaged stream-wise velocity for three stratification levels.

in the fluid column. When sediment suspension is large in the fluid column two-way coupling effects cannot be neglected.

3.5.2 Turbulent Fluxes

As discussed, suspension varies the level of turbulence in the flow field. To show this, we present the vertical distribution of turbulent shear stress $\langle u'v' \rangle$, of the vertical turbulent intensity $v_{rms} = \sqrt{\langle v'v' \rangle}$, and of the turbulent concentration flux $\langle C'v' \rangle$. First we show the vertical profile of the Reynolds shear stress which is also discussed in the previous Section to explain the decrease of the von Kàrmàn constant of the mean velocity profile. The non-dimensional vertical profiles of $\langle u'v' \rangle$ are given in Figure 3.6a, for the passive scalar case and the two-way coupling simulation results, for three sediment diameters. The figure also shows the straight line representing the total stress (right-hand side of 3.27). A significant difference can be noted between the strong stratification case $Ri_b = 0.041$ and the passive scalar case. By decreasing the bulk Richardson number (increasing sediment size) the difference decreases, and for the bulk Richardson number $Ri_b = 0.031$ a marginal decrease of Reynolds shear stress is observed. To be noted that the decrease of $\langle u'v' \rangle$ obtained in our simulations is larger than that measured in the experiments of Muste et al. [2005]. This can be attributed to the fact that the Reynolds number of our simulation (based on the bulk velocity) is equal to 9600, much smaller than that of the reference experiments (17600). In fact, it is well known that the increase of Re makes the flow less sensitive to stratification effects.

Increasing the suspended concentration in the flow field (decreasing the particle size) causes a noticeable reduction of the vertical velocity fluctuations. This is clearly shown in Figure 3.6b, where we report the wall-normal (vertical) turbulent intensity v_{rms}, scaled with the shear velocity, for the

passive scalar and the two-way coupling cases. The results are consistent with the finding of Muste and Patel [1997] and Cellino and Graf [1999] which indicate the suppression of vertical turbulent momentum flux in presence of suspended particles.

In Figure 3.6c we present the variation of the turbulent concentration flux normalized by $u_\tau C_{ref}$. A comparison between one-way coupling and two way coupling is shown for $d^+ = 1$ and $d^+ = 3$, respectively. In all cases, the quantity is zero at the opposite boundaries and reaches the maximum value in the buffer layer of the boundary layer (see Pope [2000] for a definition). In the two-way coupling simulations, the turbulent concentration flux is always smaller than the correspondent one-way coupling case. For larger particle size ($d^+ = 3$), smaller deviation from the one-way coupling result is observed, compared to $d^+ = 1$. This behavior explains the variation of the mean concentration profile discussed in subsection 3.5.1.

3.5.3 Turbulence Power Spectra

Spectral analysis is a useful tool to understand how the turbulent kinetic energy distribution along the wave modes is altered by sediment suspension in the flow. In spectral analysis, turbulent fluctuations are considered as superposition of different spatial modes. Large length-scale structures extract energy from the mean flow, then transfer the energy to smaller and smaller scales up to viscous dissipation occurring around the Kolmogorov micro scale.

In Cellino and Graf [1999] it has been shown that sediment suspension reduces the turbulent power density in the range of low wave modes. Here, the spatial power spectra were computed for vertical fluctuating velocity at $y/\delta = 0.5$. Figure 3.7 shows the comparison between one-way and two-way coupling power spectra for the strongest stratification cases herein investigated ($Ri_b = 0.041, 0.038$). Note that the integral of the power spectra of the vertical velocity fluctuations is equal to the vertical Reynolds stress:

$$\int_0^\infty E_{vv}(k_x)dk = \overline{v'v'}. \tag{3.28}$$

The power density associated with the low spatial modes slightly decreases in the two-way coupling cases. This effect is more noticeable for small sediments (strong stratification case) in Figure 3.7b. Our result is consistent with the analysis of Cellino and Graf [1999] who observed the same behavior by adding suspended particles to clear-water. The difference is more remarkable in the low wave-number range, indicating that the presence of suspended sediments tends to destroy, at a larger extent, the large scales of turbulence.

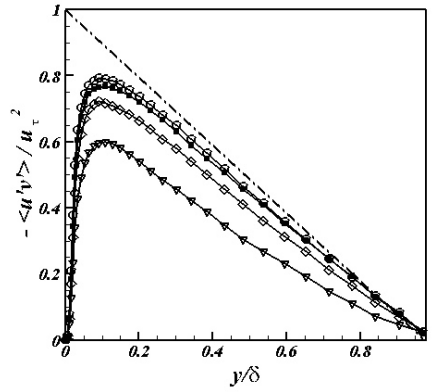

(a)

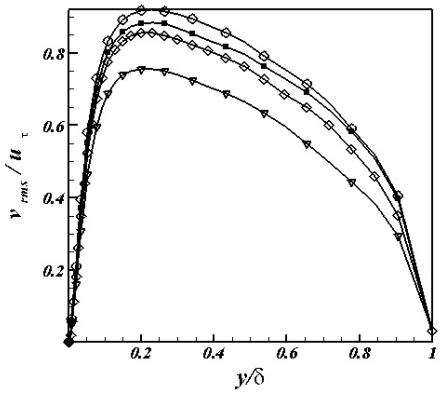

(b)

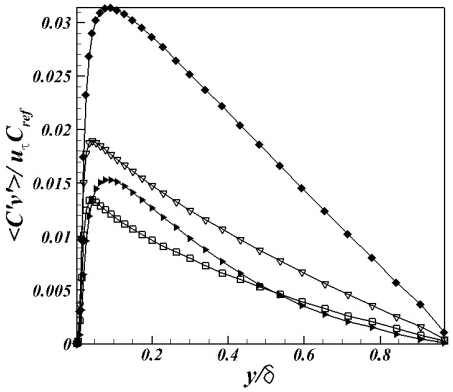

(c)

Figure 3.6: Turbulent fluxes for different stratification levels. (a) Turbulent shear stress ($\langle -u'v' \rangle$) and (b) vertical turbulent intensity (v_{rms}). Total shear stress: dash line, passive scalar case: circle, $Ri_b = 0.031$: square, $Ri_b = 0.038$: diamond, $Ri_b = 0.041$: gradient. (c) Turbulent concentration flux. Passive scalar case for $d^+ = 1$: diamond, two-way coupling for $d^+ = 1$: right triangle, passive scalar case for $d^+ = 3$: gradient, two-way coupling for $d^+ = 3$: square.

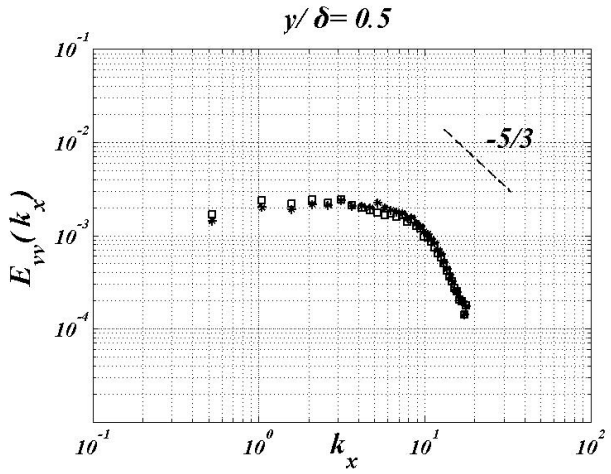

(a)

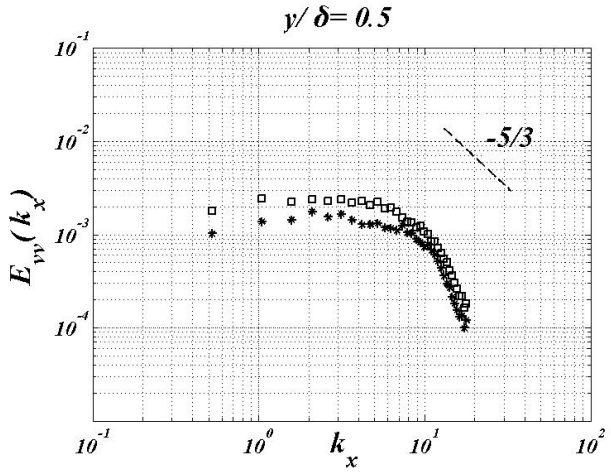

(b)

Figure 3.7: Comparison of spatial turbulence power spectra (E_{vv}) for one-way (square) and two-way coupling (star) at $y/\delta = 0.5$(a) $Ri_b = 0.038$ (b) $Ri_b = 0.041$.

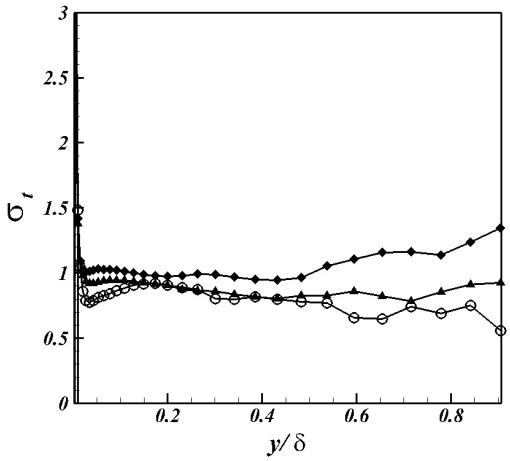

Figure 3.8: Vertical profile of turbulent Schmidt number for different levels of stratification, diamond: $Ri_b = 0.041$, delta: $Ri_b = 0.038$, circle: $Ri_b = 0.031$.

3.5.4 Turbulent Diffusivity

The estimation of turbulent momentum and concentration diffusivities by Equation 3.17 and Equation 3.18 is relevant for modelling purposes when using engineering tools for prediction of sediment suspension. As already discussed, the turbulent Schimdt number provides information on the ratio between turbulent momentum and concentration diffusivities. The Reynolds analogy assumes $\sigma_t \approx 1$ in the inertial part of the boundary layer. We have calculated directly σ_t by post-processing data of our simulations and show its vertical profile for different sediment sizes in Figure 3.8. Our results show that σ_t is nearly constant along the fluid column and increases with stratification. This is consistent with theory of stratified flows, since stratification inhibits vertical diffusivity of the sediment concentration at a larger extent than momentum diffusivity. On average, σ_t increases from a value $\sigma_t = 0.75$ for $Ri_b = 0.031$ to a value $\sigma_t = 1.1$ for $Ri_b = 0.041$, somewhat confirming the validity of the Reynolds analogy for this class of flows.

The effect of suspended sediments on the coefficient of concentration diffusivity (defined as $k_t/(u_\tau \delta)$ has been analyzed. Usually, the vertical distribution of diffusivity is presented for different values of the parameter $\beta = v_s/u_\tau$ appearing in the Rouse equation. In general, the diffusivity coefficient is nearly constant in the inertial part of the boundary layer and increases with β. We have calculated the non-dimensional concentration diffusivity from our numerical data and placed it over a plot containing the experimental data of Gust [1984]. When comparing our numerical results with experimental data we must consider that in our study $8.7 * 10^{-3} < \beta < 0.33$. The corresponding value of β for $Ri_b = 0.031$ is about 0.22 which is in the range of values as those of the Coleman's experiments. In agreement with the experimental data of Coleman, the turbulent concentration diffusivity is

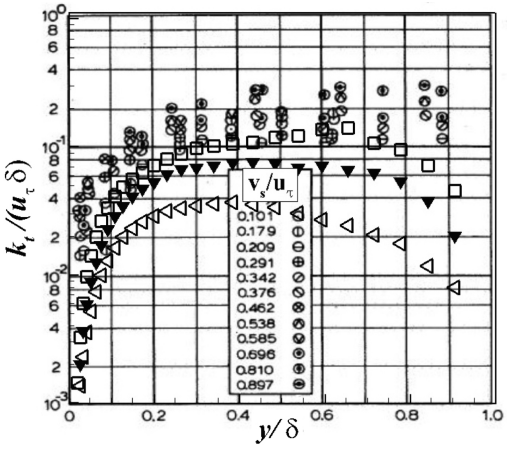

Figure 3.9: Vertical profile of turbulent concentration diffusivity for different sediment sizes, square: $Ri_b = 0.031$, $\beta = 0.22$, gradient: $Ri_b = 0.038$, $\beta = 0.077$, left-triangle: $Ri_b = 0.041$, $\beta = 8.3 * 10^{-3}$.

nearly constant in the inertial part of the flow.

For the case $Ri_b = 0.031$, corresponding to the suspension of the larger sediments herein considered, the diffusivity profile is within the range of the Coleman's data. By increasing the bulk Richardson number, thus decreasing the sediment size, the profile qualitatively fits the experimental one although being shifted down in the plot. This may be attributed to the fact that the value of β for these two cases is out of the range of the Coleman's experiments.

3.5.5 Validation of Single Phase Hypothesis

One of the main concerns in treating the water-sediment mixture is to validate the single phase approach. As described in the introduction, the single phase hypothesis holds if the settling velocity of particles is very small compared to the vertical turbulent velocity fluctuations ($v_s \ll v_{RMS}$). The ratio between v_{RMS} and the settling velocity is shown in Figure 3.10 along the vertical direction for one-way and two-way coupling approach for $d^+ = 1$. The vertical profiles follow the shape of v_{RMS} since the settling velocity is constant along the vertical. By considering the density variation in presence of particles in the flow field (two-way coupling), the ratio decreases as compared to the one-way coupling case. The values indicates that by considering the two-way coupling, the single phase assumption is still valid in the present study.

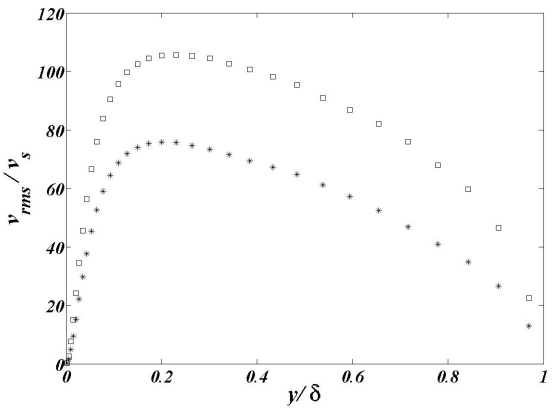

Figure 3.10: Validation of single phase approach for $d^+ = 1$, square: one-way coupling, star: two-way coupling.

3.5.6 Turbulence Structure

In a previous Section, when discussing the vertical profile of the gradient Richardson number, we argued on the fact that it is smaller than 0.2 in all cases except for the most stratified one, where it exceeds the critical value in a narrow region close to the free surface. According to Armenio and Sarkar [2002] in this region ($Ri_g \preceq 0.2$), the flow is in the buoyancy affected regime and hence ruled by active turbulence. A way to show that, is visualization of instantaneous turbulent structures in the most stratified case, namely $Ri_b = 0.041$. Actually, here we show a longitudinal cut of instantaneous concentration contour (Figure 3.11a) and 3D coherent structures (Figure 3.11b).

In Figure 3.11a a fully turbulent scenario is depicted. Concentration, coming from erosion process at the bottom surface is transported along elongated and inclined coherent structures, typical of wall-bounded turbulence. The most condensed area is observed near the bottom where the upward flux pushes the sediments into the water column. These structures appear more isotropic and increased in size moving along the channel height. The image does not show internal-wave patterns thus confirming what argued in the previous Sections. The coherent motion in turbulent flow is commonly associated with vertical structures which can be depicted by using the second invariant Q method. The second invariant Q, which quantify the relative strength of rotation and strains, is defined as $Q = (W_{ij}W_{ij} - S_{ij}S_{ij})$ where W_{ij} is the rotation rate tensor and S_{ij} is the strain rate tensor. The 3D image shows the presence of near-wall turbulent structures responsible of upward transport of sediments in the flow. The turbulent structures are mainly observed near the wall and extending up to half channel. Despite the high amount of concentration in water column, internal wave are not detected in the flow structure.

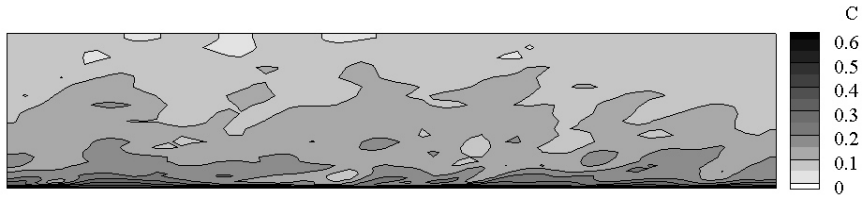

(a)

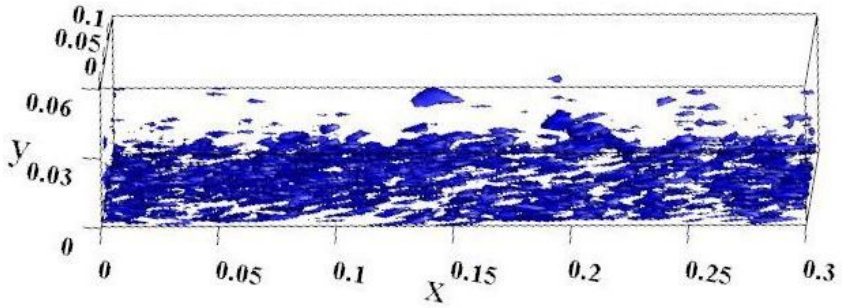

(b)

Figure 3.11: (a) Longitudinal cut of instantaneous concentration contour for $Ri_b = 0.041$,(b) 3D image of instantaneous coherent structures for corresponding bulk Richardson number. The value $Q(u/L)^2/(u_\tau/\delta)^2 = 72$.

3.6 Conclusions

In the present study Large eddy simulations were performed to investigate interaction between turbulence and suspended sediment transport in a turbulent open channel flow at $Re_\tau = 600$. An Euler-Euler approach was used based on single-phase model. In order to study the feedback effect of sediment concentration on momentum, the Boussinesq form of the three-dimensional Navier-Stokes equations was considered, where a buoyancy term accounting for sediment concentration is introduced in momentum equations. The results were analyzed for both one-way and two-way coupling models. In the first case, the concentration phase is transported in the flow field and does not affect momentum transport. In the second case, sediment concentration adds a buoyancy contribution to momentum giving rise to a stable stratified flow. Non-dimensional parameters were introduced, based on the theory of stratified flows, quantifying the effect of sediment concentration on the stability of the flow field. Simulations were carried out considering four different sediment sizes and running the simulations in both one-way and two-way coupling modes.

The analysis of the cases investigated showed that the bulk Richardson number, quantifying the level of stratification in the flow field, increases with the decrease of the sediment size; this suggested that two-way coupling effects were expected to be noticeable for small sediments. The analysis of the

concentration profile was performed in light of the single terms composing the one-dimensional Reynolds-averaged equation of concentration transport. It was shown that the increase of the sediment size produces, on one hand, a smaller available concentration at the bottom surface and, on the other hand, larger deposition fluxes. As a result, sediments remain confined in the near-wall region of the boundary layer and concentration as well as its vertical gradient are small in the inertial part of the boundary layer; this gives rise to a marginal stratification effect and the difference between one-way and two-way coupling models is negligible. Conversely, small sediments are likely to be transported in the flow field. The combination of larger available concentration at the bed and reduced deposition flux, enhances suspension and contributes to stable stratification. In these cases the buoyancy contribution to momentum transport cannot be neglected and the difference between one-way and two-way coupling simulations is noticeable.

The analysis of the feedback effect of sediment concentration on momentum showed that when the sediment size is small, stratification effects reduce the turbulent vertical momentum flux (quantified by the Reynolds shear stress) and correspondingly increases the diffusive flux, causing the decrease of the von Kàrmàn constant of the velocity profile. Hence, our analysis is in agreement with seminal theories of suspended sediment transport based on laboratory experiments.

The gradient Richardson number distribution along the vertical direction showed that as far as the sediment size decreases, wider regions of the boundary layer are affected by stable stratification. The value $Ri_g \sim 0.2$, which borders the *buoyancy affected region* where turbulence is active and reduced by stratification from the *buoyancy dominated region* where equilibrium turbulence is suppressed and replaced by internal waves, is practically never reached, apart in a small region close to the free-surface of the channel, for the smaller sediment size herein considered.

The vertical profile of momentum and concentration diffusivities was also analyzed and discussed in view of relevant literature laboratory-experiment analysis. The turbulent Schmidt number was shown to be nearly constant and ~ 1 in the inertial part of the boundary layer, in agreement with the Reynolds analogy. Its value increases with decreasing sediment size, due to the fact that stratification inhibits concentration flux more than momentum flux. The vertical profile of the non-dimensional concentration diffusivity was shown to be in a very good agreement with the Coleman's experimental data.

Overall, this study clearly shows that suspended sediment transport causes a moderate stable stratified environment, where turbulence is reduced but still active and thus controlling mixing mechanisms. From a modelization point of view, the passive scalar assumption cannot be considered valid for small sediments, which are transported in the suspension mode. Our results clearly show that the two-way coupling modelization is

more representative of the actual physical process.

Chapter 4

Turbulence in Meandering Flow

4.1 Introduction

As is well-known, river flows and the associated river morphological changes are among the most complex phenomena in earth sciences. Many scholars, in different fields of science, have tried to shed light on various aspects of river flows since the beginning of the last century. These efforts encompass a wide range of topics such as river engineering, river mechanics, fluid mechanics, environmental engineering and geography.

Rivers and streams are usually classified as straight, meandering and braiding, with meandering being by far the most common plan shape acquired by rivers. Owing to their scientific and practical significance, the flows in meandering streams and meandering dynamics have been the focus of intensive research since many years. In spite of this, several aspects of meandering flows, and in particular the patterns of secondary flow and turbulence characteristics remain poorly resolved and understood.

In the present study, Large Eddy Simulation is used to penetrate these aspects in sine-generated meandering streams. The channel geometry is according to the laboratory experiments carried out by Binns and da Silva [2015]. Since channel curvature has a significant effect on the flow field and sediment transport, the simulations are carried out with two different deflection angles $\theta_0 = 45°$ and $95°$.

This chapter is organized as follows: Section 4.2 presents a brief review of meandering concepts and definitions; Section 4.3 presents a review of previous experimental and numerical works, with emphasis on recent LES studies of meandering; Section 4.4 provides a description of the laboratory test cases, the computational aspects and related boundary conditions. In Section 4.5 the results are presented and discussed in detail.

4.2 Meandering, General Concepts and Definitions

Yalin [1992] defined meandering as "a self-induced plan deformation of a stream which, under ideal conditions, is periodic and anti-symmetrical with respect to an axis x".

Meandering rivers can be regular or irregular [Yalin, 1992]. Leopold and Wolman [1957] have shown that regular meandering streams closely follow sine-generated curves. The idea of the sine-generated curve originates in the work by Von Schelling [1951], who expressed meander path as the most probable path between fixed points with a Gaussian distribution on the basis of the minimum variance concept. Leopold and Langbein [1966] approximated the expression by Von Schelling [1951] with the "sine-generated" equation for meander path, namely:

$$\theta = \theta_0 cos(\frac{2\pi l_c}{L}), \tag{4.1}$$

where l_c is distance from crossover point (O_i), L is the meander length and θ_0 is the initial deflection angle (see Figure 4.1).

The sinuosity (σ) of a meandering stream is defined as the ratio of actual river length to the down-valley length (i.e. $\sigma(= L/\Lambda_M]$). It has been shown [da Silva, 1991, Yalin, 1992] that for a sine-generated channel, σ can be expressed as:

$$\sigma = \frac{1}{J_0(\theta_0)} \tag{4.2}$$

in which $J_0(\theta_0)$ is the Bessel function of the first kind and zeroth order of θ_0 and $\Lambda_M = 2\pi B$ is meander wave length, where B is the channel width. The curvature at the apex B/R_a is given by:

$$\frac{B}{R_a} = \theta_0 J_0(\theta_0) \tag{4.3}$$

4.3 Pertinent Studies on Meandering Flows

Meandering rivers are characterized by highly three-dimensional flows dominated by energetic coherence vortices, secondary flows, shear layers, regions of recirculation and flow stagnation and non-isotropic turbulence stresses.

Owing to its role in redistributing the velocity and effect on sediment transport pattern and consequently on bed bathymetric evolution, the cross-circulatory motion is the main feature in three-dimensional river flows investigation. This cross-circularly motion affects the bathymetry evolution. In circular bends, the flow dynamics is mainly controlled by curvature-induced centrifugal and pressure gradient forces that produce transverse variations in bed topography, which in turn have a feedback effect on fluid motion

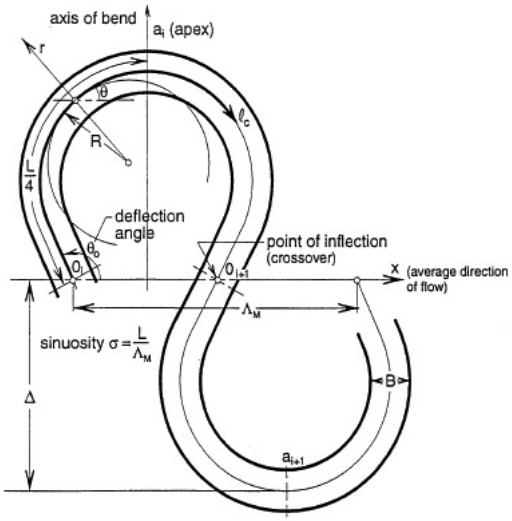

Figure 4.1: Definition geometry of a meander bend [Yalin and da Silva, 2001].

through the bend. The centrifugal acceleration induced by channel curvature directs water from the inner bank at the entrance of a bend, across the channel at high velocity, toward the outer bank. The pressure gradient force generated by the super elevated water surface at the outer bank redirects the flow toward the inner bank near the bed, where velocity and centrifugal effects are lowest (Prandtl [1952], Rozovskii [1957], Dietrich [1987]). The secondary currents, therefore, result from the local imbalance between centrifugal and pressure gradient forces over depth which results in outward movement of near surface flow and inward directed near bed flow.

The cross-stream movement of high-velocity flow from the inner to outer bank, as observed in circular bends, causes a spatial variation in boundary shear stress and bed-load transport. This pattern of spatial variation in shear stress and bed-load transport produces erosion along the outer bank and deposition along the inner bank, especially downstream of the bend apex (Dietrich [1987]).

In the case of sine-generated streams, the bed deformation results from a combination of flow acceleration/deceleration (due to the streamwise variation in channel curvature) and cross-circulation (due to the channel curvature itself). It has been shown that the convective flow pattern is a strong function of channel sinuosity. In meandering channels with small sinuosity, the streamlines diverge from the outer bank (decelerating flow) and converge on the inner bank (accelerating flow) in a zone between the crossover and apex. This pattern changes as the flow passes the apex point which implies the acceleration zone appears on the outer bank and the deceleration zone on the inner bank. The convective acceleration/deceleration of the flow re-

sults in erosion/deposition region in the vicinity of the crossovers (da Silva [1995]). In channels with large sinuosity, the flow decelerates along the outer bank and accelerates along the inner bank throughout the entire region from the first crossover to the next one.

Although, the occurrence of this type of fluvial features in bends has been extensively studied, only a few works have investigated the circulatory motion in the meandering channel. Most of the studies on flow in the curved bends have been done using laboratory flume experiments either through a rectangular cross-section or over deformed topography.

Detailed laboratory and field studies of flow in meandering streams have been carried out by Rozovskii [1957], Chang [1971], Shiono and Muto [1998], and Tamai et al. [1983], among many others. The secondary flow measurement in two subsequent 180° bends (Siebert and Götz [1975]) showed that the strength of the secondary flow decreased in the second bend. Ippen [1962] carried out experimental studies to measure the shear stress in a meandering channel. The cross-section of the laboratory case was trapezoidal with side slope of 1 : 2. He indicated that the bed shear stress has a crucial role to predict the bathymetry changes in the meandering channel and a larger radius of curvature will cause a higher value of shear stress.

Blanckaert and Graf [2004] performed a laboratory study to investigate the characteristics of secondary flow in a circular flume. Their experiments were carried out in a 0.4-meter-wide flume, 60° bend angle by using an ADVP (Acoustic Doppler Velocity Profiler) to measure the 3 components of flow velocity. They noticed the existence of two-celled secondary flow in the bend and a reduced intensity of turbulence near the outer bank which results in a weaker shear stress in that region. They concluded that the flow velocity distribution is not the only factor to constitute the secondary flow in meandering channels and turbulence has also a significant effect on the circulation.

The above mentioned studies have comprehensively contributed to the understanding of the mean flow and turbulence features in the curved open channels but are often based on rather inaccurate velocity measurements on coarse measuring grids. In the meandering channels, the numerical investigation on the flow field characteristics and morphodynamics is most often implemented by using the depth-averaged models. Recently, the rather costly (in terms of computational expenses) method of Large Eddy Simulation (LES) has found increasing interest amongst the researchers of meandering channel (e.g. Moncho-esteve et al. [2010], Stoesser et al. [2010]).

Van Balen et al. [2010] have studied the main flow and secondary flow and the role of turbulence in a curved single bend open-channel flow by employing the LES technique and Reynolds-averaged (RANS) methodology. They revealed that a comparison by the experimental data collected with the ADVP method (by Blanckaert and Graf [2004]) shows generally, that LES yields much better results than RANS. Their observation indicates that

in the time-averaged flow pattern the large scale eddies play an important role to interact with the mean secondary flow structures, whereas the small-scale turbulence is merely dissipative. On the other hand, in the RANS computation, the bed shear stress pattern is not well estimated. This might result in an incorrect estimation of the development of river morphology.

A three-dimensional LES code was employed by Van Balen et al. [2009]. For this modeling, the simulation was carried out using the experimental data of Booij [2003]. The numerical results show good agreement with the experimental data.

Khosronejad et al. [2007] studied the flow and sediment transport in a channel bend using a three-dimensional low-Reynolds number $k-\omega$ turbulence model and a standard $k-\epsilon$ model. They validated their numerical model with the experimental data of Ghanmi [1999]. The authors concluded that the low-Reynolds number $k-\omega$ turbulence model yields better agreement with the measurements due to its ability to capture the wall turbulence.

Constantinescu et al. [2011] employed a hybrid numerical model of Detached Eddy Simulation (DES) to investigate the flow in a 193° strongly-curved open channel bend with a flat and equilibrium scour bed. Their results demonstrated that DES model, compared to RANS, has better ability to capture the redistribution of mean-flow streamwise velocity and vorticity in corresponding cross-sections not only in the case of flat bed but also for the deformed bed case. Based on their simulation, a more accurate prediction of streamwise velocity and vorticity results in a more accurate estimation of shear stress and morphological changes.

A numerical simulation was performed by Zeng et al. [2010] in meandering flow using a RANS model. The simulation was based on mobile bed topography and the bathymetry changes were considered. They reported that the RANS model can yield a good agreement with experimental data at a much lower computational cost than LES.

Stoesser et al. [2010] presented a numerical study with both RANS and LES method to predict turbulent flow in a meandering channel. They used an experimental database for model comparison which was based on measurements in a flume consisting of a sequence of two 180° bends with a short 0.5 m long straight reach connecting the two bends. Both of their simulations predict the primary helical flow pattern in the meander as well as the occurrence of an outer-bank secondary cell. They indicated that LES was found to be slightly superior to RANS in predicting the time-averaged secondary velocities.

In recent years, a number of researchers [Van Balen et al., 2009, Zeng et al., 2010] presented their fully three-dimensional models with the treatment of the free water surface. For three-dimensional modeling of open channel flows, calculation of the free water surface presents a very difficult problem. Most models employ one of the three techniques: the rigid-lid assumption, the Volume-of-Fluid (VOF) technique, or calculation of water

level based on the kinematic boundary condition.

The rigid-lid assumption treats the free water surface as a plane of symmetry where zero gradient conditions are applied for the variables parallel to the surface with the wall-normal variables set to zero [Stoesser et al., 2010]. This is the simplest method computationally, thus having a definite advantage in terms of the calculation costs. On the other hand, to represent the free surface of the flow, the time-averaged pressure distribution resulting from the numerical simulations can be used to calculate the equivalent water levels [Van Balen et al., 2009, Zeng et al., 2010]. In the present study, the deformation of the free surface is considered in the numerical model.

4.4 Description of Simulation Cases

4.4.1 Flow Configuration

As previously stated, in the present simulation, the computational domain was constructed based on the laboratory study carried out by Binns [2012] in two sine-generated channels having $\theta_0 = 45°, 95°$.

The simulated channels have a rectangular cross-section with width to depth ratio 14.9. The bed consisted of silica sand having an averaged grain size D equal to 0.65 mm. The hydraulic condition of the tests [Binns, 2012] were as summarized in Table 4.1 in which h_{av} is the flow depth, S_c is the bed slope along the channel centerline, u_{av} is channel averaged flow velocity, v^* is the shear velocity, Re is flow Reynolds number ($= u_{av}h_{av}/\nu$ where ν is fluid kinematic viscosity) and Fr is Froude number ($= u_{av}/\sqrt{g.h_{av}}$), Re_* is Roughness Reynolds number ($= v^*k_s/\nu$ calculated using $k_s = 2D$), $(\tau_w)_{av}$ is channel-averaged bed shear stress ($= \gamma S_c h_{av}$ in which γ is fluid specific weight) and τ_{cr} is bed shear stress at the critical stage of initiation of sediment transport. In contrast to previous LES studies of meandering flows, the present test cases involve streams exhibiting a continuous variation of curvature in the streamwise direction, a large value of width-to-depth ratio and a large value of Froude number.

Table 4.1: Hydraulic conditions of experimental tests ($B = 0.3\ m$ and $D = 0.65\ mm$.)

Run	θ_0°	$Q\ [m^3/s]$	$h_{av}\ [cm]$	S_c	$u_{av}\ [m/s]$	$\nu^*\ [m/s]$	B/h	B/R_a	Re	Fr	Re_*	$(\tau_w)_{av}/\tau_{cr}$
Case 1	45	0.0019	2.01	1/130	0.321	0.039	14.9	0.67	6438	0.72	51	4.64
Case 2	95	0.0018	2.02	1/130	0.29	0.039	14.9	0.7	5839	0.65	51	4.66

4.4.2 Computational Details

The computations were performed, in each case, on a very high-resolution grid consisting of $560 \times 64 \times 128$ points in the streamwise, wall-normal and

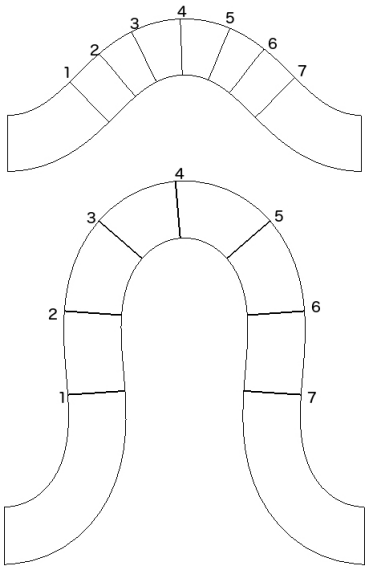

Figure 4.2: Computational domain view in $x - z$ plane.

spanwise directions, respectively. In total, the number of grid points is approximately equal to 4.5 million. Based on the wall unit, the maximum grid spacing is $\Delta x^+ = 55$ in streamwise and $\Delta z^+ = 15$ in spanwise directions. In order to satisfy the requirement for the wall-resolving LES, the grids are stretched close to the wall regions in both spanwise and wall normal directions. The distance of the first grid point to the bottom-wall is $\Delta y^+ = 1$ in which $y^+ = v^* y/\nu$. The $x - z$ plane view of the computational domain for both cases is shown in Figure 4.2. Cross-sections 1 and 7 coincide with crossover positions in the channels. The selected cross-sections will frequently be referred to in the text.

No-slip boundary condition is used at the bed and side walls with approximately five grid points placed within the viscous layer. A periodic boundary condition is assumed only in streamwise direction. A constant pressure gradient Π was imposed to drive the flow along the meandering channel. The walls are assumed to be smooth.

After reaching a statistically steady condition, the simulation has been run for about 40 non-dimensional time units based on the channel averaged velocity (u_{av}) and the channel length to accumulate statistics.

4.4.3 Free Surface Treatment

All open-channel curved streams exhibit a transverse inclination of the free surface which varies along the bend. The water surface inclination consists of a level difference between the inner bank and the outer bank of the bend

(Δh) and can be obtained from the balance of transverse forces acting on a column of fluid.

As mentioned earlier, the free surface can be treated as a plane of symmetry. For this purpose, the wall-normal variables in the free surface are set to zero. This assumption is accurate enough for small Froude numbers ($Fr \leq 0.4$) where the super-elevation of the free surface is less than 10% of the channel depth [Van Balen et al., 2010, Stoesser et al., 2010, Constantinescu et al., 2011]. In the flow field with sufficiently large Froude number, the effect of super-elevation on the flow properties is thought to be not insignificant. Therefore, the contribution of this study is to predict an accurate flow field in a meandering channel in 3D simulation by introducing the free surface elevation.

The approach proposed here is to impose a hydrostatic pressure variation as a body force in the Navier-Stokes equations (Lopez, S. personal communication, Dec 2015).

Here, we will denote the normal projection of Navier-Stokes equations over the free-surface by:

$$n \cdot \nabla P = \frac{\partial p}{\partial n} = \nu \nabla^2 u_n - (\frac{\partial u_n}{\partial t} + \vec{u} \cdot \nabla u_n) + f_n, \tag{4.4}$$

where f_n is a Lipschitz continuous function that represents the force term.

The imposed force f_n at the computational surface is assumed to be the weight of a water column of height η_{fs}:

$$f_n = -g\eta_{fs}, \tag{4.5}$$

where g is the gravity acceleration and η_{fs} is height difference with respect to mean water level.

To have a realistic assumption of free surface elevation, the modified variational method by Yalin and da Silva [2001] is considered to estimate the water level (η_{fs}) along the channel (for more details see Appendix A). The numerical results of the simulation by considering the free surface elevation are presented in the following section.

4.5 Results and Discussion

This section addresses the resulting time-averaged flow properties in the aforementioned meandering channels. The corresponding velocity components in curvilinear coordinates are streamwise velocity U_ξ, transverse velocity U_ζ and vertical velocity U_η.

4.5.1 Velocity Distribution

The time-averaged streamwise velocity profiles along the channel are shown in Figure 4.4 and Figure 4.5, for two vertical levels. It is noticeable from these figures how the streamwise velocity varies along the bend. It can be observed in Figure 4.4 that the highest velocity appears just before the apex of the bend at the inner bank. The predicted pattern is consistent with the flow field measured by da Silva [1995] in a channel having small deflection angle (30°). The most distinct difference between the streamwise velocity pattern in two vertical level apart from their magnitude is the high inclination of velocity vectors close to the channel bed which is due to the large transverse velocity close to the channel bed.

For the 95° meander channel, the general trend of the streamwise velocity is found to be different from the previous case.

According to da Silva [1995], for sufficiently large values of the initial deflection angle (θ_0) (and a flat bed), the maximum velocity is located at the inner bank in a region approximately close to the crossover (Figure 4.3). From the velocity field measurement by da Silva [1995], it has been reported that the longitudinal velocity near the inner bank increases along the section Oa and decreases along the section aO' if the deflection angle is small. This flow trend has been termed as *ingoing*. On the other hand, for large sinuosity channel, the velocity near the inner bank constantly decreases throughout the region OaO' which is referred to as *outgoing* flow.

Figure 4.5 reveals a shift of maximum velocity location backwards to the crossover points. Noteworthy is the fact that the velocity magnitude in the inner bank continuously decreases throughout the region between two crossovers (*outgoing* flow).

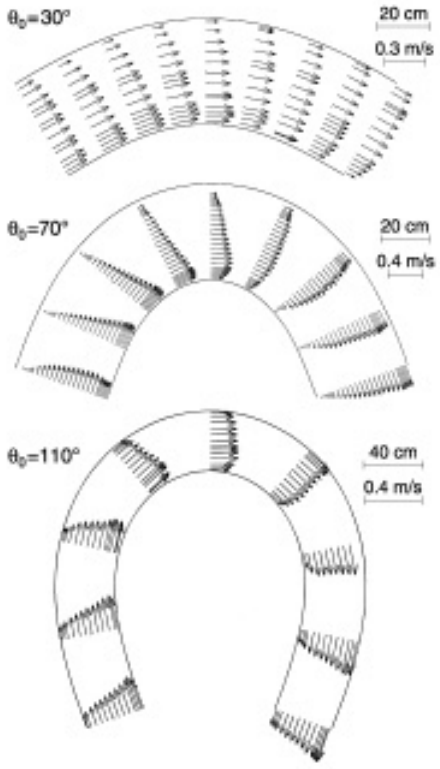

Figure 4.3: Velocity field for $\theta_0 = 30°$, $70°$ and $90°$ [da Silva, 1995].

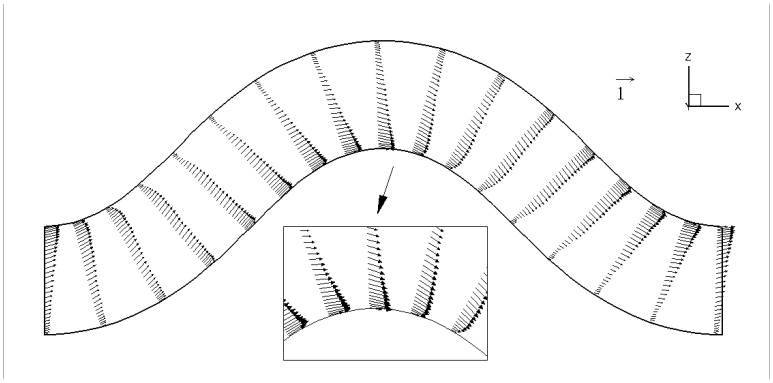

(a) at vertical level $y^+ = 24$

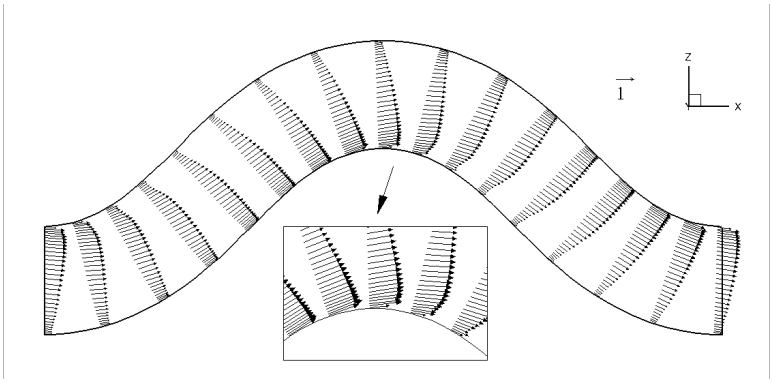

(b) at vertical level $y^+ = 350$

Figure 4.4: Pattern of streamwise velocity U_ξ scaled with averaged velocity u_{av} along the 45° meandering channel.

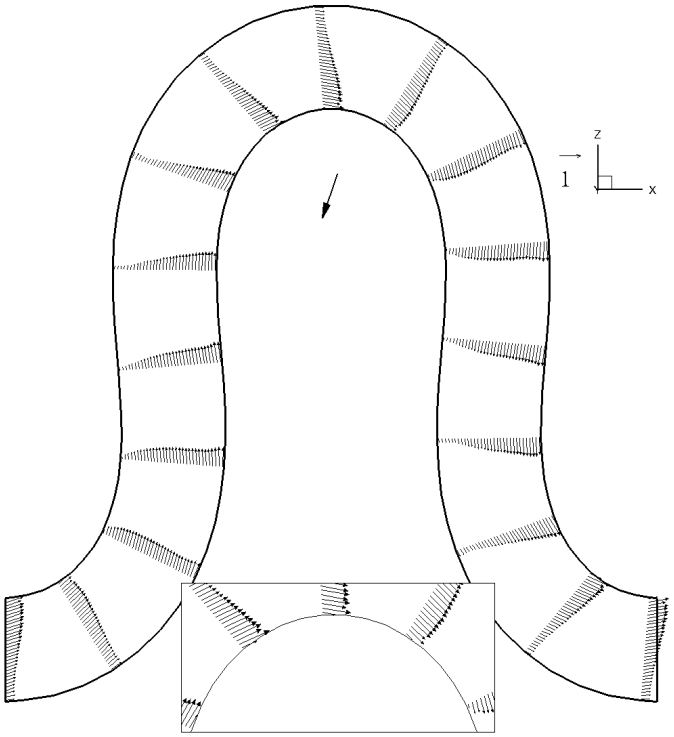

(a) at vertical level $y^+ = 24$

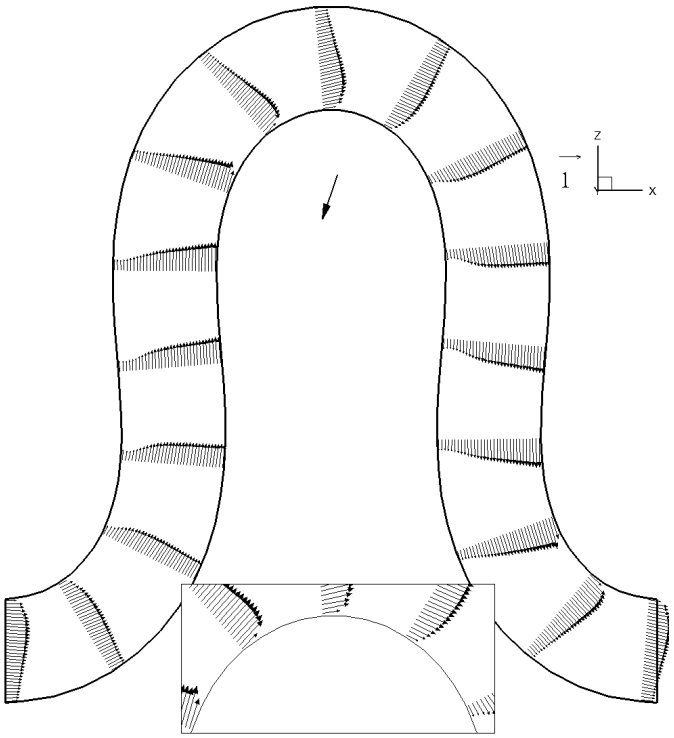

(b) at vertical level $y^+ = 350$

Figure 4.5: Pattern of streamwise velocity U_ξ scaled with averaged velocity u_{av} along the 95° meandering channel.

4.5.2 Time Averaged Secondary Flow Pattern

The generation of secondary flows in the meandering channel is mainly controlled by the centrifugal force and the lateral component of flow. To discuss the details of the secondary motion in a meander, Figure 4.6 shows the computed secondary velocity vectors and streamwise velocity contours for the case of 45° in selected cross-sections between the first and second crossover. The numerical results of cross-sectional view are plotted only for every $3rd$ grid line.

As can be observed, the intensity of secondary motion varies as the flow progresses through the bend. The intensity of secondary motion at section 1 is larger than that at section 2 because the secondary flow is enhanced by the transverse component of the flow which is larger in section 1 due to the channel curvature.

At section 3 a new secondary motion is generated from the bottom edge of the inner bank towards the outer bank. This results in a double direction change of velocity vector along the channel depth. The new secondary flow grows rapidly from section 3 to 4, reaching its largest at section 5. The center core of this secondary motion for the case of 45° is observed in one-third of channel depth. The magnitude of secondary flow decreases gradually towards the next crossover point. For the crossover sections (1 and 7), the secondary flows rotate conversely (toward the inner bank in section 1 and toward the outer bank in section 7). The periodic phenomenon can also be discovered when comparing the sections 1 and 7 of the meandering channel.

To explore the flow field further, the contour plots of the streamwise velocities are also presented in the same cross-sections in Figure 4.6. The time-averaged results are normalized by the averaged velocity in the channel. It is noted that the centrifugal force tends to move the high momentum fluid from inner bank towards the outer bank in the bend region. This leads to the meandering of the flow as seen in the color contour plots of the streamwise velocity component. The location of maximum streamwise velocity is varied from one section to another. In the first crossover (section 1), the highest velocity is observed in the middle of the channel width. Moving toward the apex (section 4), the maximum velocity location approaches to the inner bank of the bend as a result of channel curvature.

Furthermore, considering the vertical distribution of streamwise velocity, in most cross-sections the maximum velocity occurs at about one-third of the channel depth, below the free surface. This shift is due to the secondary motion convecting the high-momentum flow mass from the surface to the region below the free surface.

The circulatory motion for high deflection bend (95°) is shown in Figure 4.7. It appears that the sinuosity has a dominant effect on the secondary flow pattern in that the formation of the secondary cell is different in comparison to the latter case. The strength of the secondary motion is also

larger than for the case of 45°. The predicted secondary flow generated in 95° channel is almost symmetric in the apex (section 4). It is found as the sinuosity increases, there is a shift in the location of maximum secondary motion. The developing secondary flow seems to reach its maximum in section 4, which shifts towards upstream of the bend as compared to the case of 45°. This shift can also be observed for the location where the new secondary motion encounters with the existing spiral motion in section 2.

The streamwise velocity contour plots are also presented in Figure 4.7 for the case of 95° meandering channel. A few differences in comparison with the latter case should be pointed out. The maximum velocity region in the crossover (section 1) deviates from the channel center and moves toward the inner bank compared to the 45° meander channel. The same trend is apparent in the other cross-sections.

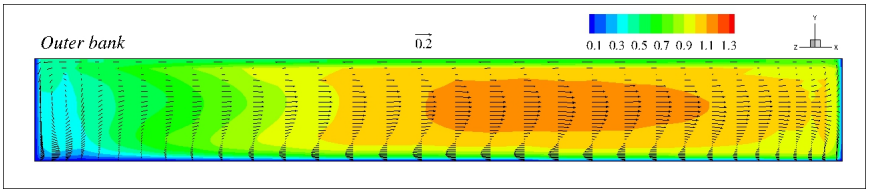

(a) Cross-section 1

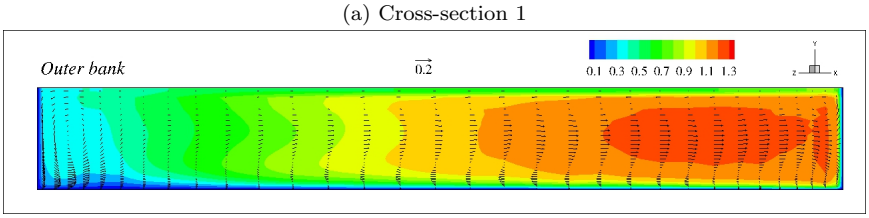

(b) Cross-section 2

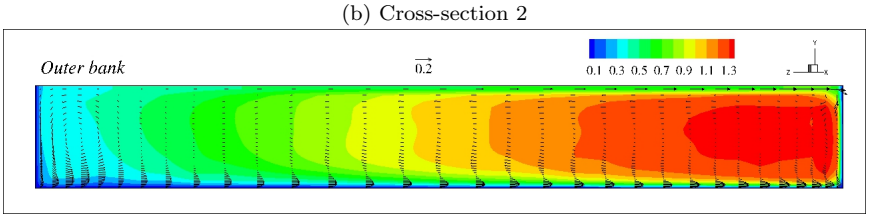

(c) Cross-section 3

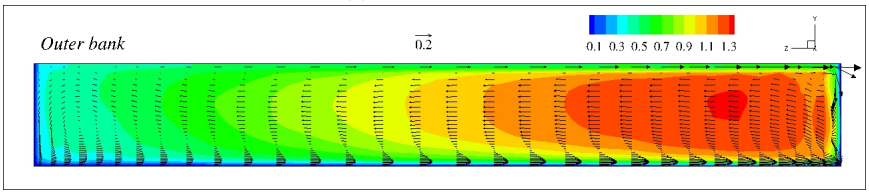

(d) Cross-section 4

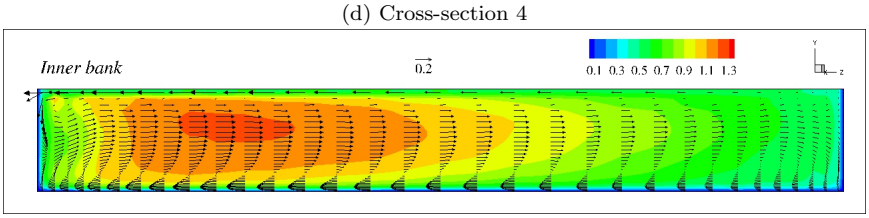

(e) Cross-section 5

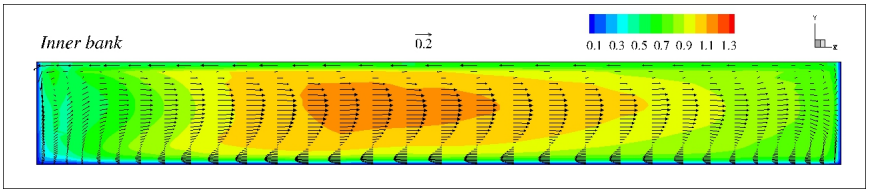

(f) Cross-section 6

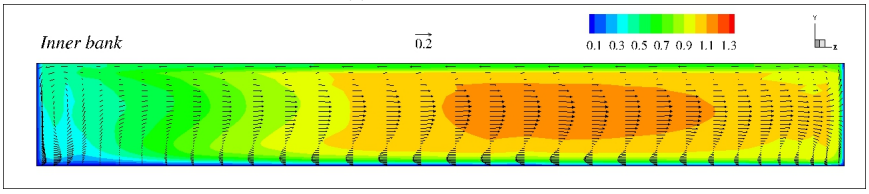

(g) Cross-section 7

Figure 4.6: Secondary motion pattern and streamwise velocity contour plot in different cross sections for 45° meandering channel. All variables are normalized by u_{av}.

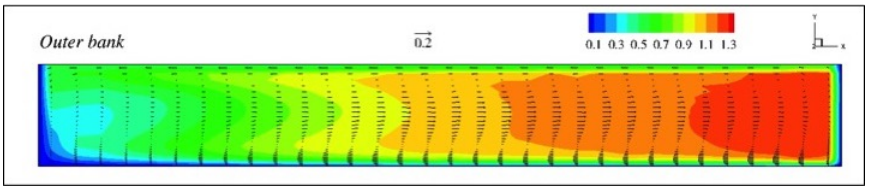

(a) Cross-section 1

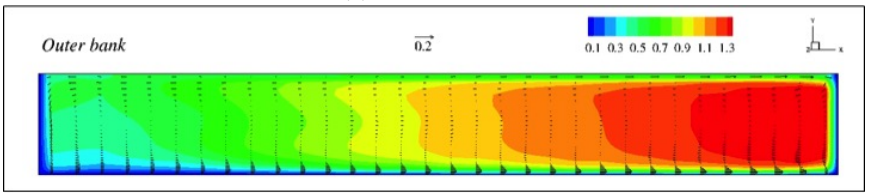

(b) Cross-section 2

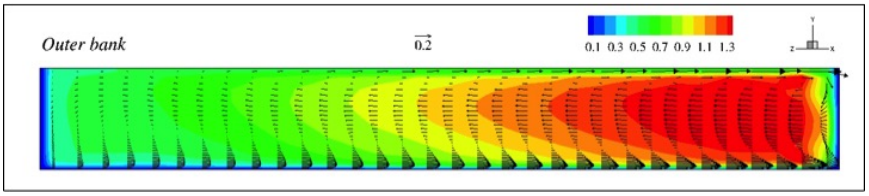

(c) Cross-section 3

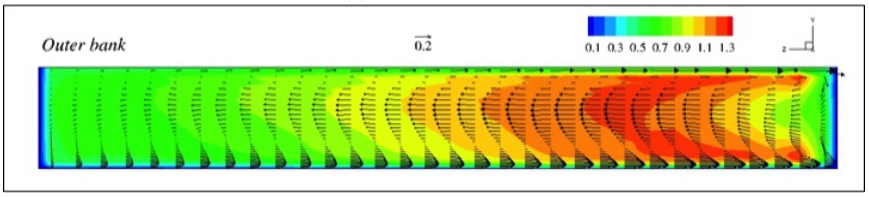

(d) Cross-section 4

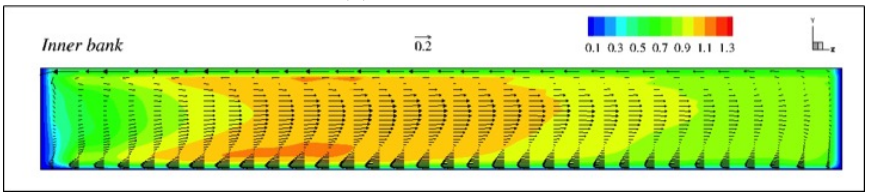

(e) Cross-section 5

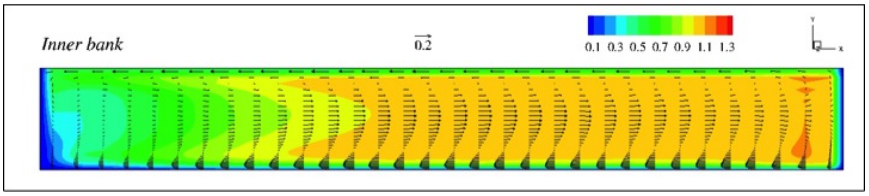

(f) Cross-section 6

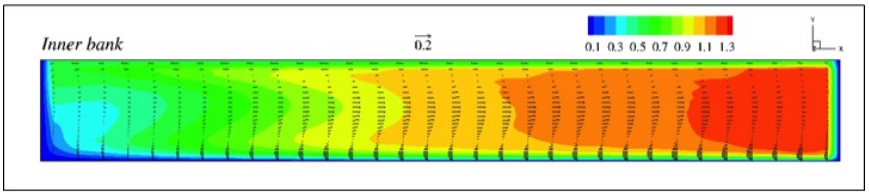

(g) Cross-section 7

Figure 4.7: Secondary motion pattern and streamwise velocity contour plot in different cross-sections for 95° meandering channel. All variables are normalized by u_{av}.

4.5.3 Vertical Distribution of the Velocity Field

In addition to the analysis of the transverse distribution of the streamwise velocity along the meandering streams (subsection 4.5.1), a similar procedure can be followed to analyse the redistribution of the streamwise velocity in the vertical direction. The curvature variation may cause deformations of the streamiwse velocity distribution with respect to its straight channel shape. For the case of 45°, the vertical distributions of the streamwise velocity component are shown for different cross-sections in Figure 4.8 and Figure 4.9. One may observe that the distribution of the streamwise velocity along the vertical direction tends to be skewed outwards in some regions in the bend.

The physical interpretation of the local deformation in the streamwise velocity distribution is essentially referred to the influence of the secondary stream to convey the momentum inside the meandering bend. The curvature-induced secondary stream convects the high-momentum fluid form the surface to a region below the surface. This flow in the lower part of the cross-section has a momentum surplus and consequently increases the streamwise velocity. This effect is considerably strong, near the apex region and especially at cross-sections 1, 2 and 5, where the secondary cell reaches its highest intensity (see Figure 4.6).

Similar comparisons are shown in Figure 4.10 and Figure 4.11 for the case of 95°. The deformation of streamwise velocity in the vertical direction can be explained in the same way as for the case of 45°. According to Figure 4.8-Figure 4.11, the difference between the vertical distribution of streamwsie velocity in the case of 95° and 45° is reflected by the locus of the deformation. Throughout the section 4 of the 95° meandering bend the intensity of the secondary flow increases. This implies an overall larger reduction of the streamwise velocity in the upper part of the cross-section with respect to the latter case.

To summarize, it can be concluded that the redistribution of the streamwise velocity in vertical direction is mainly caused by the secondary flow. It worth noting that the mechanism of this deformation is proportional to the intensity of the secondary motion.

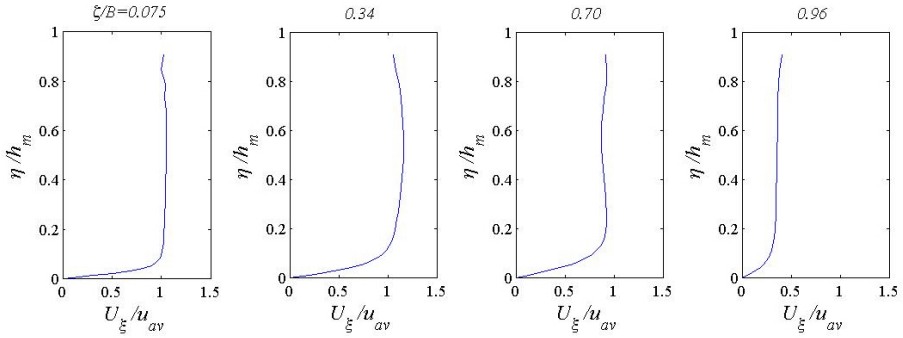

(a) Cross-section 1

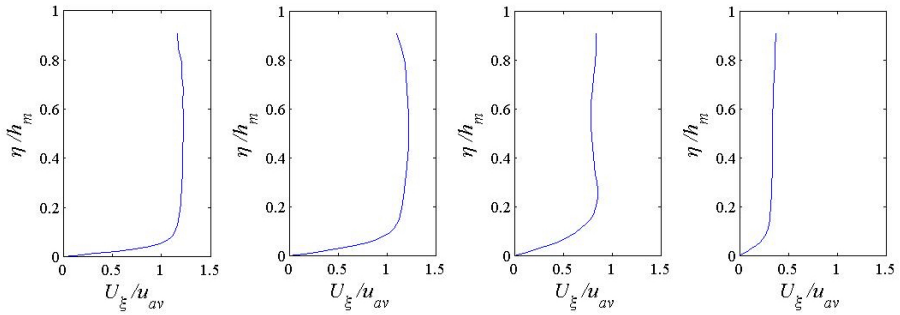

(b) Cross-section 2

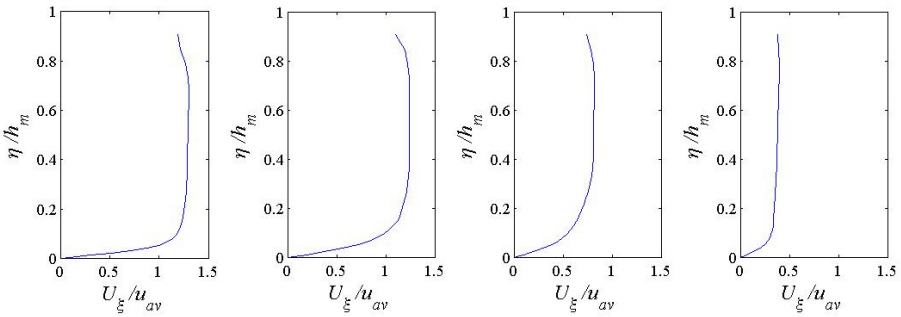

(c) Cross-section 3

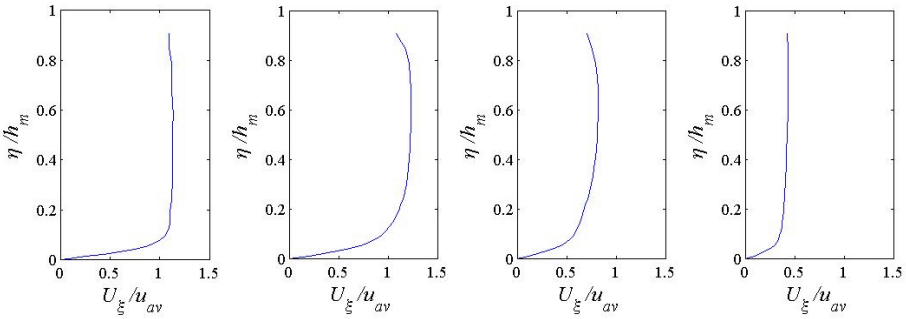

(d) Cross-section 4

Figure 4.8: Vertical distribution of the streamwise velocity for 45° meandering channel.

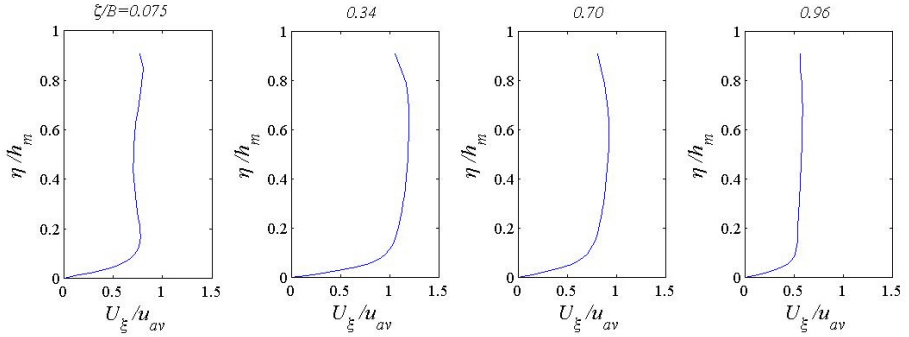

(a) Cross-section 5

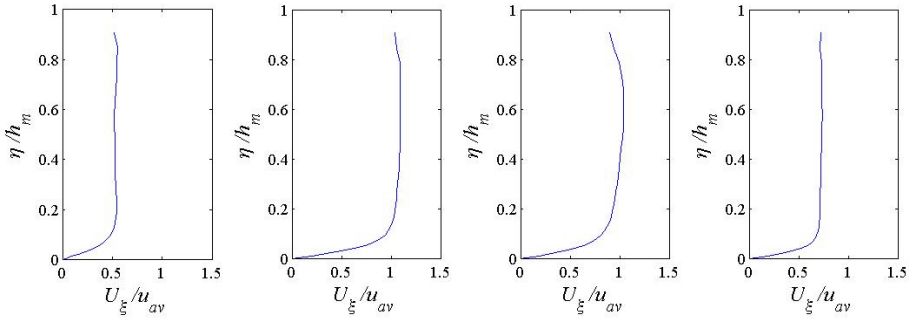

(b) Cross-section 6

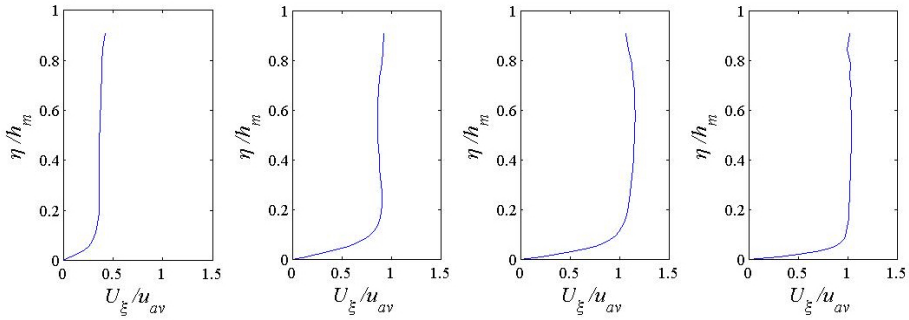

(c) Cross-section 7

Figure 4.9: Vertical distribution of the streamwise velocity for 45° meandering channel.

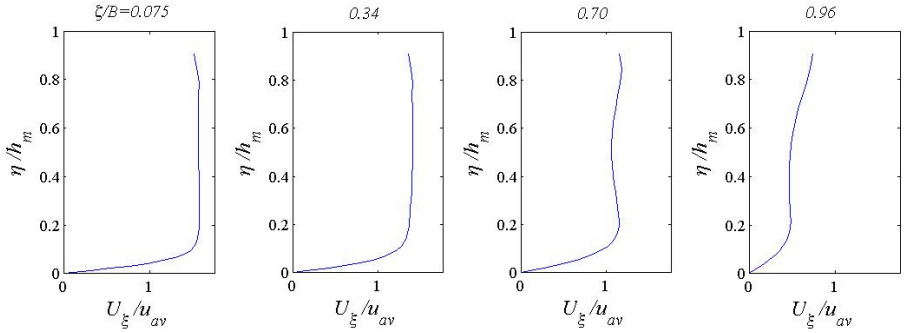

(a) Cross-section 1

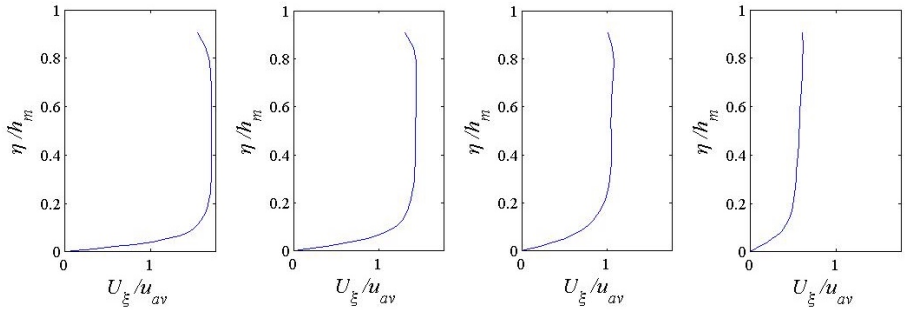

(b) Cross-section 2

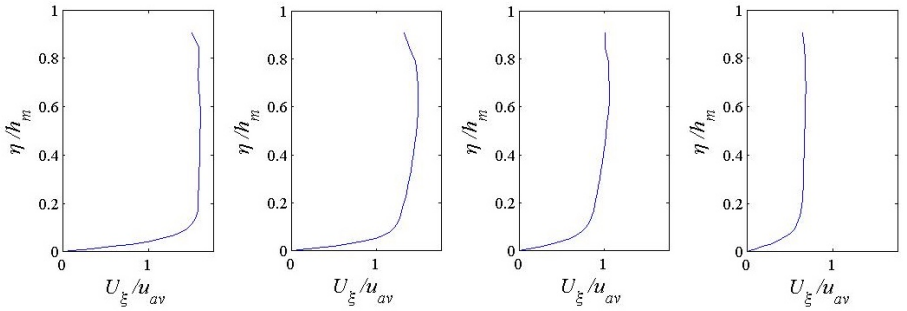

(c) Cross-section 3

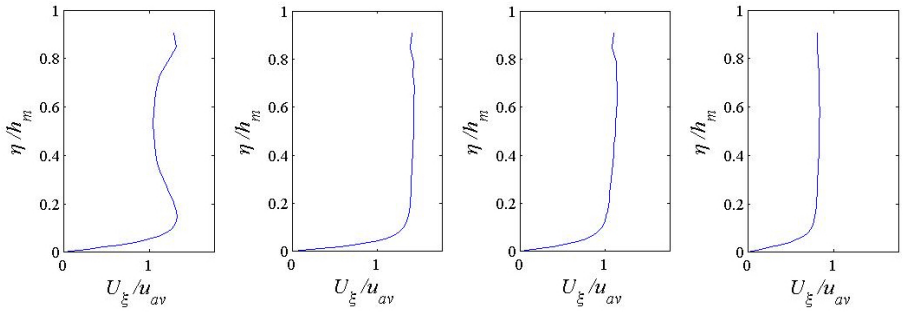

(d) Cross-section 4

Figure 4.10: Vertical distribution of the streamwise velocity for 95° meandering channel.

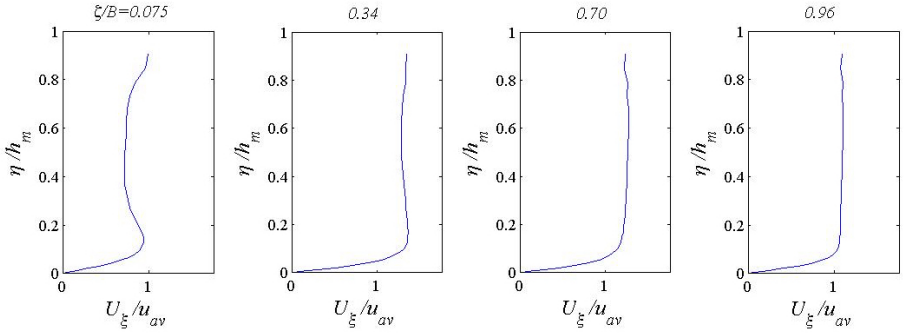

(a) Cross-section 5

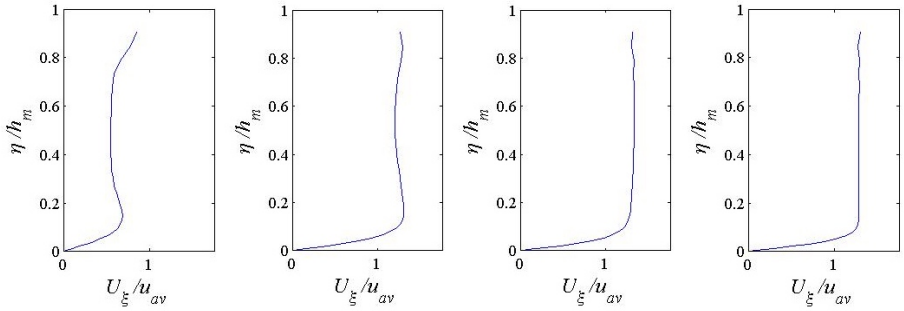

(b) Cross-section 6

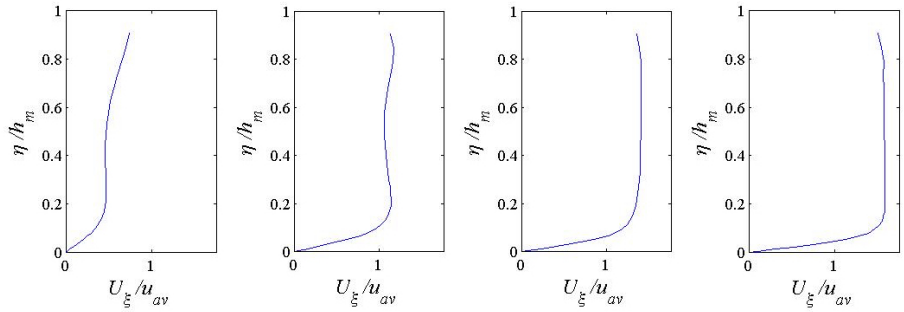

(c) Cross-section 7

Figure 4.11: Vertical distribution of the streamwise velocity for 95° meandering channel.

4.5.4 Bed Shear Stresses

The pattern of the bed shear stress provides a good indication of the erosion-deposition regions. To estimate the bed shear stress in the curvilinear coordinate, the shear stress components are computed in streamwise (ξ) and spanwise (ζ) direction as:

$$\tau_\xi = \mu \frac{\partial U_\xi}{\partial \eta}, \quad \tau_\zeta = \mu \frac{\partial U_\zeta}{\partial \eta} \tag{4.6}$$

in which μ is dynamic viscosity of the fluid. The total (time-averaged) bed shear stress is obtained by:

$$\tau_w = \sqrt{\overline{\tau}_\xi^2 + \overline{\tau}_\zeta^2} \tag{4.7}$$

The distribution of bed shear stress is shown in Figure 4.12 and Figure 4.13. Time-averaged bed-shear stress contour plots were normalized with the density times the square of the averaged velocity.

In Figure 4.12, it can be observed that the region of maximum bed shear stress at the inner bank is situated mostly in the apex while the minimum bed shear stress is located adjacently on the opposite bank. The computed shear velocity pattern (Figure 4.13) shows a slight shift of the high bed shear stress region towards the apex upstream compared to the latter one.

Reported by Abad and Garcia [2009], for the intermediate sinuosity, very high values of bed shear stress were found in upstream from the bend apex. For high-sinuosity channel (90°) the peak shear stress region is detected slightly upstream of the bend apex at the inner bank. Generally, the plan distribution of bed shear stress predicted by the LES model is in good agreement with the previous studies.

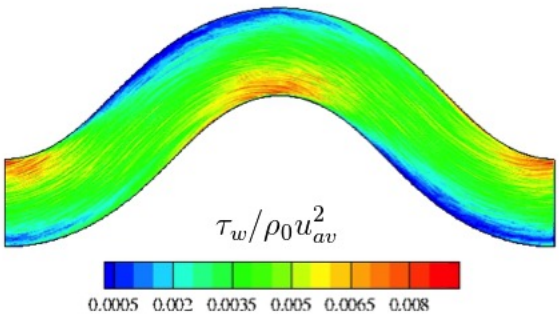

Figure 4.12: Normalized time-averaged bed-shear stress contour plot for 45° meandering channel (flow from left to right).

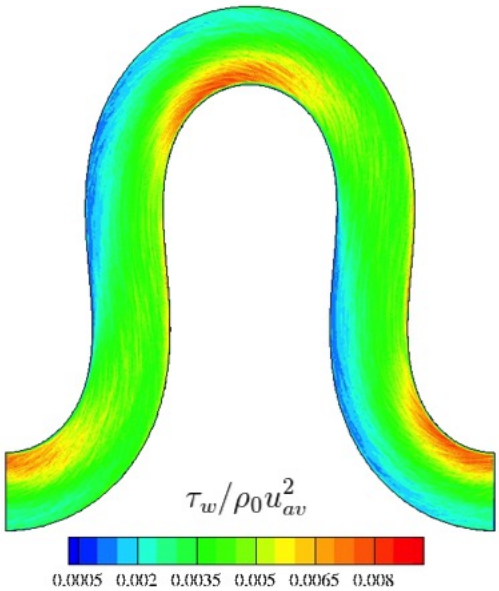

Figure 4.13: Normalized time-averaged bed-shear stress contour plot for 95° meandering channel (flow from left to right).

4.5.5 Divergence of Specific Volumetric Bed-load Rate

The prediction of the bed deformation out of bed shear stress distribution is a key element in the study of natural bends. The bed deformation is governed by the sediment transport continuity equation:

$$\frac{\partial z_b}{\partial t} = -\frac{1}{(1-p)} \overrightarrow{\nabla} \cdot \mathbf{q}_{sb}, \tag{4.8}$$

in which z_b is bed elevation measured with regard to an arbitrary reference datum, t is time, p is porosity of the bed material and $\mathbf{q}_{sb}$ is specific volumetric sediment transport rate vector. In the case of bed-load transport only, as in the present test cases, $\mathbf{q}_{sb}$ in Equation 4.8 is to be identified with the (specific, volumetric) bed-load rate. Here, the following generalized version of Bagnold's bed-load rate is adopted (see Yalin and da Silva [2001]).

$$\mathbf{q}_{sb} = \overrightarrow{U_b} \cdot [\beta(\tau_w - \tau_{cr})/\gamma_s], \tag{4.9}$$

in which $\overrightarrow{U_b}$ is flow velocity vector at the bed, τ_w is bed shear stress, τ_{cr} is value of τ_w at the critical stage for initiation of sediment transport, γ_s is submerged specific weight of the bed material ($\gamma_s = 16186.5$ N/m^3) and $\beta \approx 0.5$. Equation 4.9 can be written as:

$$\mathbf{q}_{sb} = \frac{\beta}{\gamma_s} \overrightarrow{U_b} \cdot [(\tau_w - \tau_{cr})]. \tag{4.10}$$

The flow velocity at the bed $\overrightarrow{U_b}$ can be typified by the average flow velocity within the bed-load layer, having the thickness ϵ (Yalin and da Silva [2001]). In this work ϵ was determined from the following equation, due to Van Rijn [1984]:

$$\frac{\epsilon}{D} = 0.3\Xi^{0.7}(\frac{\tau_w}{\tau_{cr}} - 1)^{0.5}, \tag{4.11}$$

where D is average grain size of the bed material and Ξ is material number ($\Xi = (\gamma_s D^3/\rho_0\nu^2)^{1/3}$ in which ν is fluid kinematic viscosity and ρ_0 is fluid density). This yielded $\epsilon = 2.6$ mm.

Substitution of Equation 4.10 into Equation 4.8 yields the following expression for the sediment transport continuity equation:

$$\frac{\partial z_b}{\partial t} = -\frac{\beta}{\gamma_s(1-p)}\overrightarrow{\nabla}\cdot[\overrightarrow{U_b}\cdot(\tau_w - \tau_{cr})]. \tag{4.12}$$

In the following, to represent the bed deformation, the term $\overrightarrow{\nabla}\cdot\mathbf{q}_{sb} = \overrightarrow{\nabla}\cdot[\overrightarrow{U_b}\cdot(\tau_w - \tau_{cr})]$ is calculated. This can be written in curvilinear coordinates as follows:

$$\overrightarrow{\nabla}\cdot\mathbf{q}_{sb} = [\frac{\partial}{\partial\xi}[U_\xi\cdot(\tau_w - \tau_{cr})] + \frac{\partial}{\partial\zeta}[U_\zeta\cdot(\tau_w - \tau_{cr})]]. \tag{4.13}$$

According to the sediment transport continuity equation (Equation 4.12), the accelerating flow (i.e., if $\overrightarrow{\nabla}\cdot\mathbf{q}_{sb} > 0$), causes erosion, and the decelerating flow (i.e., if $\overrightarrow{\nabla}\cdot\mathbf{q}_{sb} < 0$), causes the deposition.

Figure 4.14 shows the contour plot of time-averaged $\overrightarrow{\nabla}\cdot\mathbf{q}_{sb}$ to reveal more details in the flow domain. As shown in Figure 4.14a, the erosion zone is situated in a narrow region adjacent to the inner bank. The deposition bar starts slightly before the apex in the outer bank. Figure 4.14b presents an elongated erosion-deposition zone in the 95° bend. The erosion zone ($\overrightarrow{\nabla}\cdot\mathbf{q}_{sb} > 0$) is shifted gradually towards upstream.

To reveal how the presented numerical results compare with previous studies which investigate the bed deformation within channel bends, the results of the laboratory study by Binns and da Silva [2015] are presented in this section (the hydraulic conditions of experiments are summarized in Table 4.1).

In the aforementioned experiments, the channel walls were made of 2.5 mm thick acrylonitrile butadiene styrene (ABS plastic); the movable bed consisted of a well-sorted silica sand having average grain size (D_{50}) equal to 0.65 mm and specific density equal to 2.65. The experiments started from a flat bed (i.e. no slope in transverse direction) and were continued until the morphological conditions reached the equilibrium stage. The flow rate Q was kept constant throughout the duration of the runs.The tests were carried out in a series of time-steps to monitor the temporal bed evolution. In both

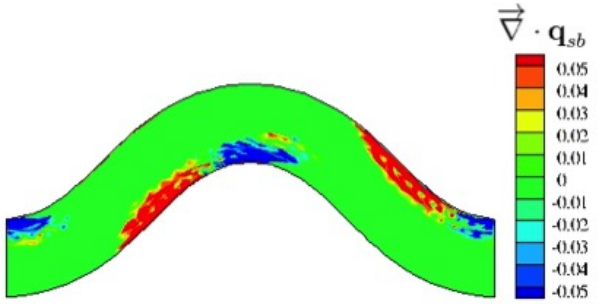

(a)

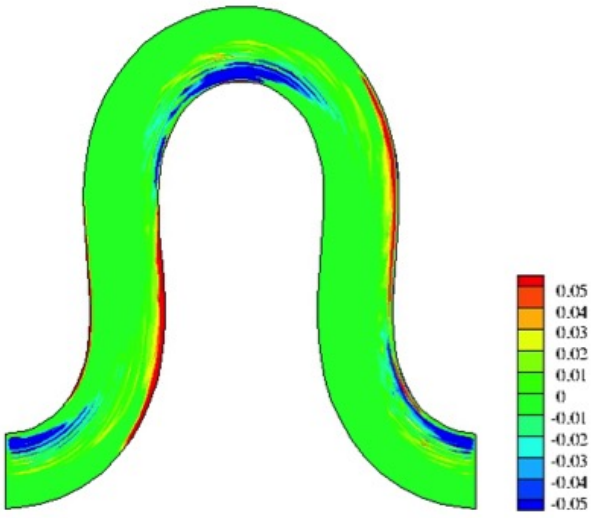

(b)

Figure 4.14: Contour plots of time-averaged $\vec{\nabla} \cdot \mathbf{q}_{sb}$ for the (a) 45° (b) 95° channel (flow from left to right).

experimental cases, the bed developed by acquiring laterally adjacent, large-scale erosion-deposition zones, having the length $L/2$ (in which L is meander length measured along ξ_c).

Figure 4.15 shows the bed elevation contour plots corresponding to the test case 1 (Table 4.1) at two time steps. The first measurement time reflects the early stage of bed development (Figure 4.15a) while the second measurement time represents the equilibrium condition (Figure 4.15b). As can be observed, the erosion-deposition zone is located downstream of the apexes. Figure 4.16 shows the bed elevation contour plot for the 95° channel at two time steps. In case 2 (95°) the $L/2$ long erosion/deposition zones were located further upstream than in case 1 (45°).

As shown in Figure 4.16a the erosion pools in the 95° channel split into two distinct pool features (marked as $P1$ and $P2$ in Figure 4.16a). Small dunes developed in the erosion pools during the course of all experimental runs due to the flow depth becoming larger over the pools as the bed deformed. The dunes, while never exceeding a few centimeters in height, became increasingly prominent as the bed became more deformed [Binns and da Silva, 2015].

As a brief conclusion, the erosion-deposition zones predicted by means of the sediment transport continuity equation are not in good agreement with those obtained by [Binns and da Silva, 2015] in both cases. As shown earlier in Figure 4.16a and Figure 4.16a the erosion and deposition region occur laterally adjacent in the meandering bend whereas this pattern does not appear in the aforementioned contour plots . In addition, the divided pool which is mentioned earlier is not observed in the predicted results for the 95° channel.

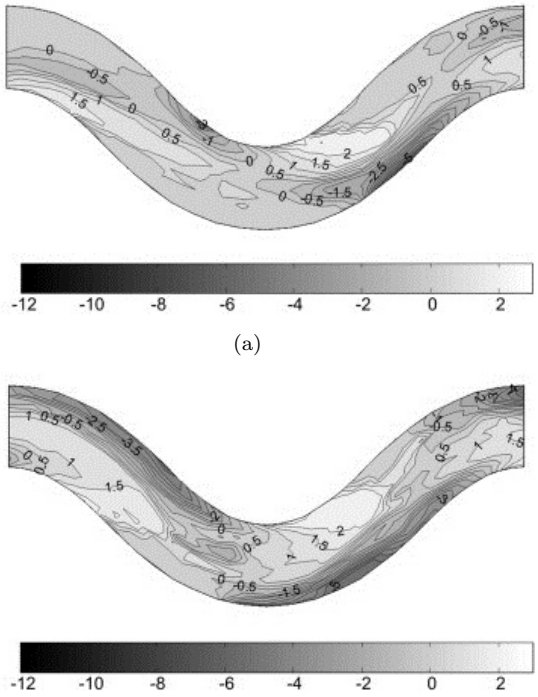

Figure 4.15: Bed elevation contour plot for the 45° channel (from Binns and da Silva [2015]) (a) at $t = 9.00$ min; (b) at $t = 54.0$ min (flow from left to right).

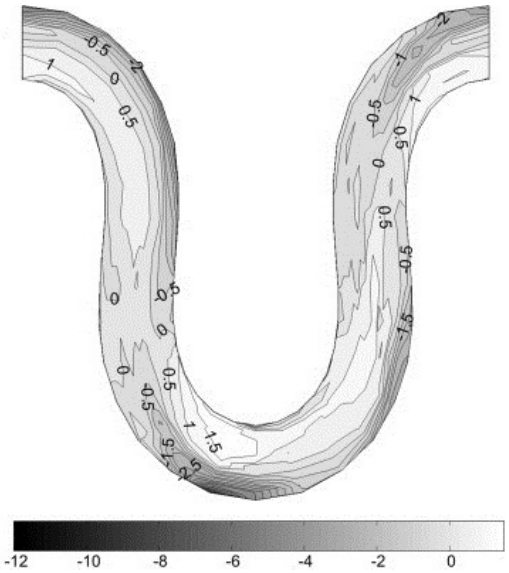

(a)

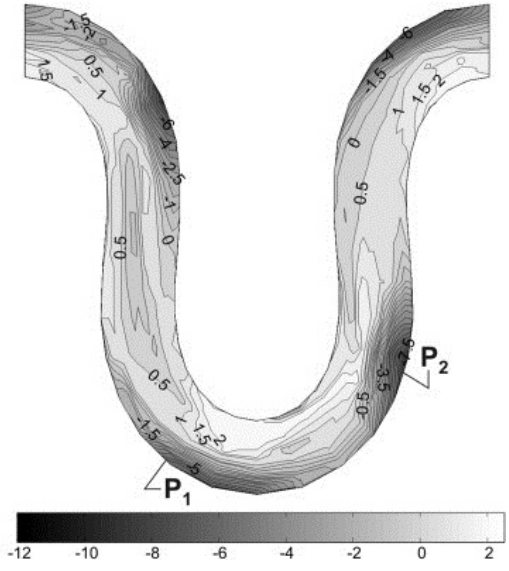

(b)

Figure 4.16: Bed elevation contour plot for the 95° channel (from Binns and da Silva [2015]) (a) at $t = 10.0$ min; (b) at $t = 70.0$ min (flow from left to right).

4.5.6 Turbulent Structures

A better understanding of turbulent structures in the cross-sections can be achieved by analysing the streamwise vorticity of mean flow along the channel.

The streamwise vorticity is defined as:

$$\omega_\xi = \frac{\partial \overline{U}_\eta}{\partial \zeta} - \frac{\partial \overline{U}_\zeta}{\partial \eta}, \tag{4.14}$$

which renders the rotational strength of the secondary flow. The streamwise vorticity is calculated with the mean values of transverse and wall-normal velocity. In Figure 4.17, the distribution of the time-averaged streamwise vorticity (ω_ξ) is shown for the selected cross-sections of simulation cases. In this figure, ω_ξ is normalized by u_{av}/h. The originating mechanisms of secondary flow can be clarified by examining the strength of vorticity identified in Figure 4.17a. As shown in Figure 4.17a a shear layer associated with positive vorticity comes into existence from the inner bank towards the outer bank in section 3. The figure clearly shows that the area identified with the positive vorticity corresponds to the generation of a new clockwise secondary flow at the inner edge of section 3 (see Figure 4.6c). The streamwise vorticity generated at the inner edge of the bend at section 3 is enhanced, enlarged and transported downstream of the bend (section 5). It can also be seen that this vorticity reduces in strength as the flow reaches the crossover area.

The predicted distribution of ω_ξ in the large sinuosity case (95°) shows that the pattern is quite similar. However, the values for the vorticity are higher in this case. The general trend of these results is consistent with the vorticity distribution obtained from simulations by Constantinescu et al. [2011] for the flat bed case.

4.5.7 Turbulence Stresses

The mean flow analysis in the previous sections shows that there are shear layers and vorticity zones in the apex region of the meandering channel. This implies the turbulence will be generated due to the shear layer. The turbulence characteristics in a meandering channel are now considered in detail.

Turbulence intensity is obtained for all normal components as the variance of the temporal velocity variation:

$$< u_i' u_i' >= \frac{1}{T} \Sigma (u_i(t) - \overline{u}_i)^2 \Delta t. \tag{4.15}$$

The normal shear stresses $< u'u' >$, $< v'v' >$ and $< w'w' >$ correspond for streamwise, wall normal and spanwise directions respectively.

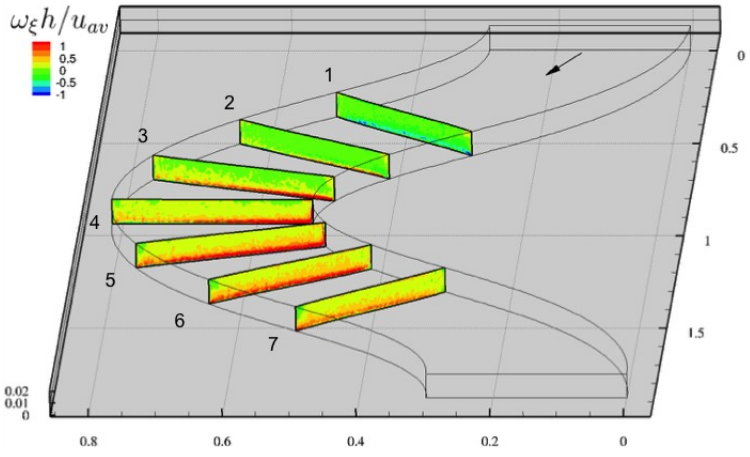

(a)

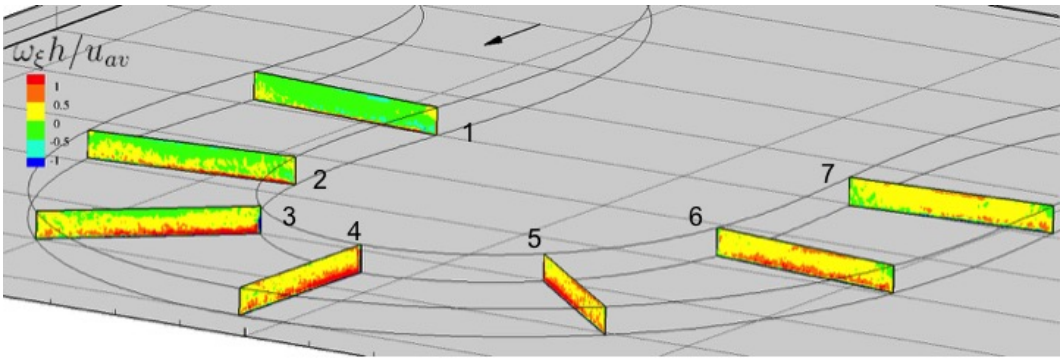

(b)

Figure 4.17: Time-averaged streamwise vorticity contour plots at different cross-sections for (a) 45° meandering channel (b) 95° meandering channel.

Reynolds shear stresses are expressed as the temporally averaged product of two components of the velocity variation. Results for the normal and shear Reynolds stresses over selected cross-sections are presented in Figure 4.18 to Figure 4.21. The calculated results are scaled by squared of the averaged velocity (u_{av}^2) in the channel.

As can be observed in Figure 4.18a, the location of the maximum streamwise fluctuation $< u^{'}u^{'} >$ is recognized clearly in the inner bank region of the channel apex. From the streamwise velocity contour (Figure 4.6) and vorticity contour plot (Figure 4.17a), the highly turbulent intensity areas for $< u^{'}u^{'} >$ along the meandering channel are located at roughly similar locations of the maximum vorticity and streamwise velocity. The area in which the magnitude of normalized $< u^{'}u^{'} >$ are relatively high, shifts towards outer bank as the flow passes through the channel apex. It can be clearly seen that the wall-generated turbulence is dominant in the inner parts of the apex section.

The streamwise velocity fluctuations decrease toward the crossover region due to the suppression of the secondary flow. The contour plot of streamwise velocity fluctuations for the 95° bend (Figure 4.19a) follows a similar trend with an exception in the location of maximum magnitude. It can be noticed that compared to the 45° meandering channel, the location of maximum streamwise stress is shifted towards the upstream after the crossover section.

The wall-normal velocity fluctuations contour plot is shown in Figure 4.18b. The maximum magnitude of the wall normal intensities is generally smaller than that of the streamwise intensities. The vertical fluctuations ($< v^{'}v^{'} >$) with high magnitude are generated in the side wall regions (inner and outer banks) for all lateral sections. The maximum magnitude of the vertical fluctuations is generated in the inner bank of section 5 where the strongest secondary flow is located.

Figure 4.19b presents the wall-normal velocity fluctuations for the 95° bend. The areas in which the magnitude of $< v^{'}v^{'} >$ is high coincide within the region of the high intensity secondary motion in section 4. The overall distribution of vertical velocity fluctuations for the 95° is in the same trend of the latter case (Figure 4.18b).

The transverse velocity fluctuation contours are presented in Figure 4.18c and Figure 4.19c. Such an area of high $< w^{'}w^{'} >$ for both cases are observed in the relevant location of the strong secondary cell along the meandering channel. This indicates that the spiral motion of the flow induces a large lateral component of the turbulent intensity in the apex region.

Contour plots of time-averaged streamwise-vertical Reynolds shear stress $< u^{'}v^{'} >$ over the selected cross-sections are shown in Figure 4.20a and Figure 4.21a. There is a region of positive $< u^{'}v^{'} >$ which forms at the lower part of the inner bank in section 3 (before the apex) and spreads throughout the outer bank. This region is corresponding with the developing clock-wise

secondary cell in this area (see Figure 4.6c). In contrast, in the outer bank region, negative values are observed for $< u'v' >$. An outward decrease from the outer bank can be observed for the absolute value of $< u'v' >$ in this region. The cross-sectional pattern of $< u'v' >$ clearly reveals the streamwise periodicity in the meandering bend.

Figure 4.20b and Figure 4.21b show the distribution of the normalized streamwise-spanwise Reynolds shear stress $< u'w' >$ along the meandering bends. This Reynolds shear stress seems to be mainly correlated with the distribution of the lateral and streamwise component of the velocity in the corresponding cross-section. The absolute value of $< u'w' >$ slightly decreases from section 1 to 3 where the outward directed lateral velocity is damped by the channel curvature. The values then increase towards section 5 and 6 as the inwards lateral velocity components attain large magnitude. The maximum of the absolute values for this Reynolds intensities is observed in the region with high streamwise velocity. The distribution of $< u'w' >$ in the 95° channel is nearly similar to those of the 45° channel. The latter shows a shift of $< u'w' >$ pattern towards the channel upstream.

To summarize, the variation in Reynolds stresses along the channel length highlights the influence of channel geometry on the distribution and magnitude of these stresses.

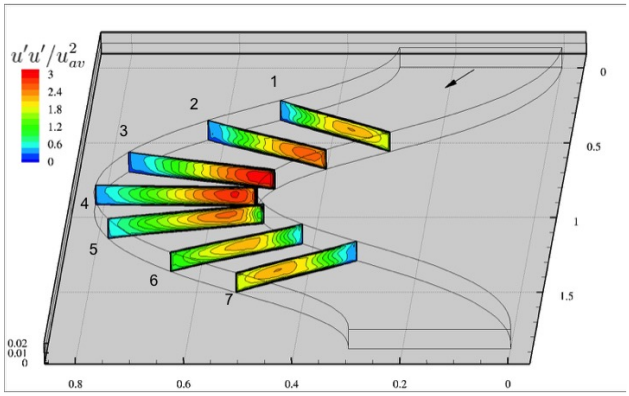

(a)

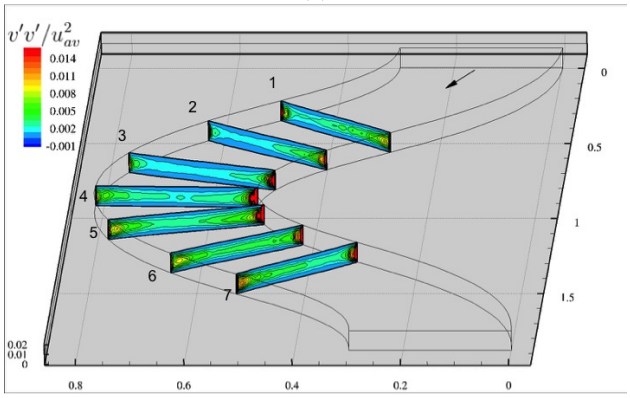

(b)

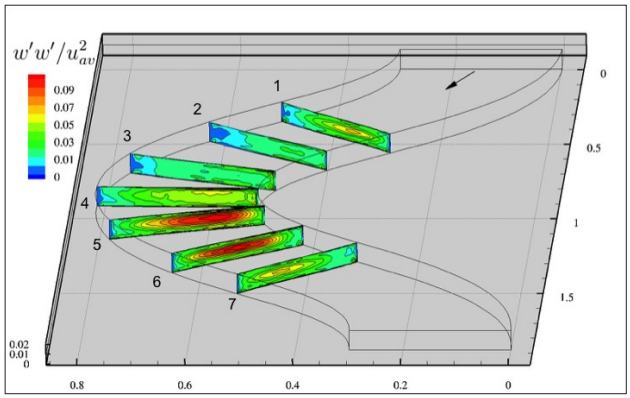

(c)

Figure 4.18: Normal Reynolds stress components along the 45° meandering channel (a) $< u^{'} u^{'} > /u_{av}^2$, (b) $< v^{'} v^{'} > /u_{av}^2$, (c) $< w^{'} w^{'} > /u_{av}^2$.

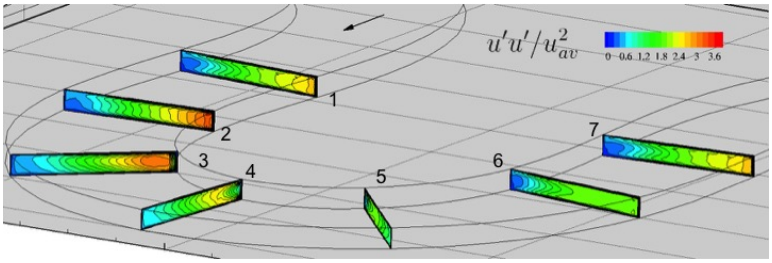

(a)

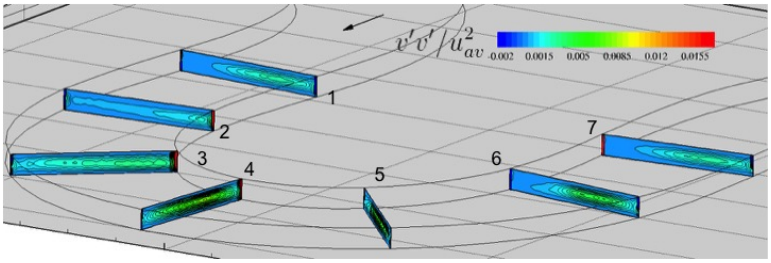

(b)

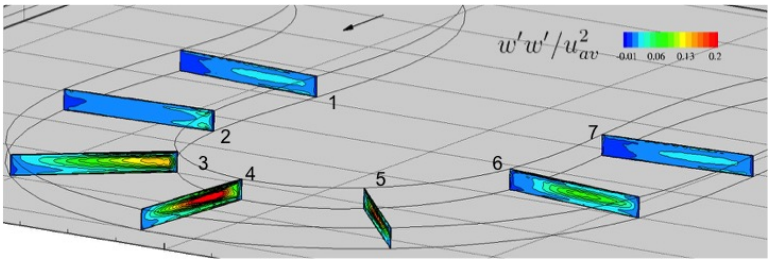

(c)

Figure 4.19: Normal Reynolds stress components along the 95° meandering channel (a) $< u^{'} u^{'} > /u_{av}^2$, (b) $< v^{'} v^{'} > /u_{av}^2$, (c) $< w^{'} w^{'} > /u_{av}^2$.

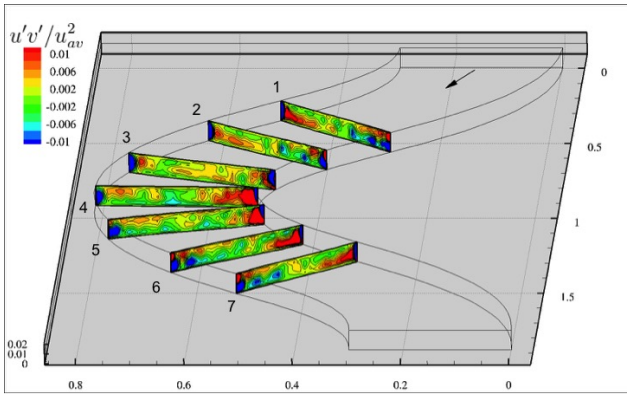

(a)

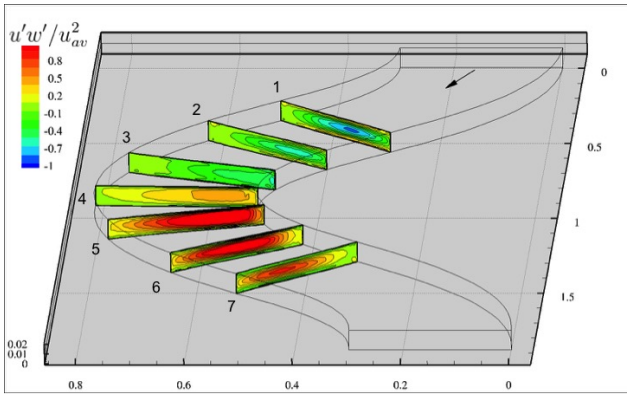

(b)

Figure 4.20: Reynolds shear stress components along the 45° meandering channel (a) $< u^{'} v^{'} > /u_{av}^2$, (b) $< u^{'} w^{'} > /u_{av}^2$.

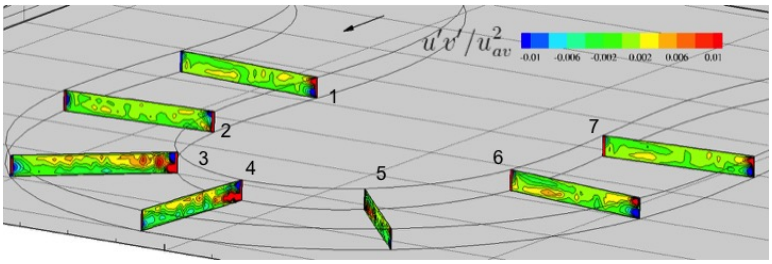

(a)

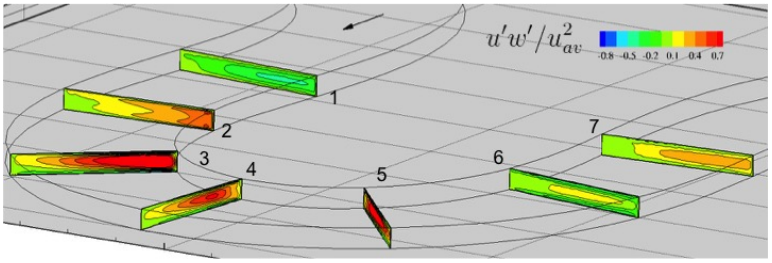

(b)

Figure 4.21: Reynolds shear stress components along the 95° meandering channel (a) $< u^{'} v^{'} > /u_{av}^2$, (b) $< u^{'} w^{'} > /u_{av}^2$.

4.6 Conclusions

A numerical investigation of turbulent flow was performed in two sine-generated channels with vertical side walls and a flat bed (no slope in the radial direction). Large Eddy Simulation was used to resolve the large scales and filter out the small scales of turbulence whose effect on the resolved field was parametrized through a Lagrangian sub-grid scale model. The simulation was carried out under the hydraulic conditions of laboratory experiments by Binns and da Silva [2015]. Periodicity condition was applied in the streamwise direction. It should be emphasized that the free surface treatment has been added to the mathematical model. The simulation results were presented in the time-averaged form in different cross-sections along the channels. The present analysis gives the indication of how the secondary flow influences the flow field, which leads to the following concluding remarks:

- Comparison of the flow field in both rectangular channels with flat bed indicated the significant influence of the channel sinuosity on the flow pattern. On closer investigation, this effect appeared specifically in the velocity pattern adjacent to the inner bank. The observed velocity patterns along both channels were consistent with the experimental results.

- The formation of the secondary cell was affected by the centrifugal

forces induced by the channel curvature. Increasing the channel sinuosity intensified the secondary motion along the channel and mutated its development through the lateral sections. As the sinuosity increases, the new formed secondary cell which was found in the upstream of the channel apex was moved backward to the crossover section.

- According to the presence of the secondary motion in the meandering bends, the distribution of the streamwise velocity was skewed vertically. In the foregoing mechanism, the high momentum fluid was conveyed to a region below the free surface.

- The contour plots of bed shear stress over the meandering bend revealed the region of maximum bed shear stress at the inner bank was located mostly in the apex while the minimum bed shear stress was located adjacently on the outer bank. The predicted patterns were in agreement with the previous studies.

- The bed deformation along the channel bends was predicted by means of the sediment transport continuity equation. The estimated results showed that the erosion zone was located in a narrow region adjacent to the inner bank and the deposition bar was situated subsequently after that. In the case of high curvature channel, the erosion zone moved gradually towards upstream.

- An analysis of the turbulent characteristics showed that the turbulence activity reduced far from the apex for both the inner and the outer bank regions. It seemed that the regions with the high value of the normal Reynolds stresses corresponded to the location of the high intensity secondary cell along the meandering channels.

Chapter 5

Sediment Transport in Meandering Channel

The nature of flow in meandering channels has pronounced effects on erosion, deposition, and sediment transport in comparison with straight channel flow. There are many complex physical processes involved in the meandering streams. Owing to the variation of the velocity field along the channel bend, the dispersion of scalar quantities may be not spatially homogeneous. This resulting nonuniform suspended sediment distribution in channel bends is subject not only to longitudinal transport but also to transverse transport caused by the circulatory motion of the flow induced by the channel curvature.

The objective of this chapter is to study sediment transport in the meandering channels in order to estimate the effect of channel curvature on suspended sediment concentration. The simulations are confined to a steady, uniform, low Reynolds-number meandering stream with a smooth bed, admitting that this circumstance does not fully represent a natural meandering bend. Here we show preliminary, still interesting results. The complete analysis will be carried out in the upcoming future.

A summary of the previous studies on the sediment transport in the meandering streams is presented in Section 5.1. This overview is followed by re-visiting the pertinent numerical computational researches. The flow and boundary conditions are described in Section 5.2. The simulation results are discussed in Section 5.3.

5.1 Previous Studies

The traditional approaches to study the sediment transport in river flows are based on field measurements and laboratory experiments. Several laboratory experiments have been undertaken to investigate the pollutant dispersion in meandering channels. It has been found that the secondary flow, which is a transverse circulation induced by channel curvature, has a significant effect on the lateral dispersion of pollutant in the meandering channels (Fischer [1969], Chang [1971], Holley and Abraham [1973], Smith [1982, 1983], Demuren and Rodi [1986]).

To understand the diffusion and dispersion for scalar transport processes, mixing is generally studied through eddy viscosity and eddy diffusivity coefficients. In an experimental study, Fischer [1969] estimated the effect of curvature on the dispersion coefficient in a bend with constant curvature. He showed the flow prediction was accurate for "fully" developed laboratory conditions. Chang [1971] conducted laboratory studies of transverse mixing in the meandering channels. This research was led to developing a relation between the transverse mixing coefficient and the channel curvature.

Shimizu et al. [1990] developed a model to calculate the 3D flow field in bends. Their model considered bed deformation and bed load transport, as well as suspended load. The model was tested for an experiment flume having 180° bend with fixed bed. A definite difference between the 3D and 2D models is found in the predicted bed deformation with suspended load. It was found that the study of bed deformation and suspended load in the meandering channels needs an appropriate estimation of the secondary flows.

The effect of secondary flows on passive contaminant diffusion processes was studied by Shiono and Feng [2003], experimentally. They performed experimental measurements in a rectangular and compound channels by using Laser Doppler Anemometer (LDA) and Laser Induced Fluorescence (LIF), instantaneously. The concentration and Reynolds fluxes were measured for the validation of the turbulence transport model. The results showed that the secondary flow skewing the concentration distributions and moving the location of concentration peaks. Another laboratory study on the relationship between the channel curvature and transverse mixing coefficient was reported by Boxall et al. [2003]. They maintained that the normalized transverse mixing coefficient varies significantly along the meandering channel. The maximum values of the transverse mixing coefficient were found in the regions of strong secondary circulation, just downstream of the bend apex.

It is rather difficult from the field measurements and laboratory studies to achieve a detailed physical understating of sediment transport, particle re-suspension and deposition in meandering channels. To date, only a few efforts have been made to predict the scalar dispersion in curved channels numerically.

A Reynolds averaged simulation had been presented by Demuren and

Rodi [1986] to calculate secondary flows and pollutant-concentration fields in meandering channels. The standard $k - \epsilon$ turbulence model has been modified to account for the effects of channel curvature on the turbulent transport mechanisms. The simulation has done for the meandering channel with different width-to-depth ratio and bed roughness. The concentration distributions are compared with the measurements of Chang [1971]. It has been shown that the bed roughness enhances the transverse mixing considerably.

A computational modeling of the flow and sediment transport in meandering rivers was performed by Shams et al. [2002]. The Reynolds stress transport model of Fluent code, was used in their simulations. The Lagrangian tracking of individual particles has been implemented. It has been reported that the sediment deposition pattern was affected by the secondary flow vortices formed on the river bend.

Duan [2004] applied a depth-averaged two-dimensional (2D) model to estimate the mass dispersion in the meandering channel. A dispersion term was included in the governing equations. The Schmidt number which correlates mass dispersion with turbulent diffusion was adjusted as a calibration parameter in 2D model. While the accuracy of 2D model is limited, they recommended employing a 3-dimensional model in order to determine the transversed mixing coefficient.

Van Balen [2010] investigated the scalar spreading through a strongly curved flow. They employed both the LES approach and the RANS approach for their simulations. It has been found that the flow deceleration occurs in the downstream inner bank region and the upstream outer bank region where the contaminant tends to accumulate. These decelerating effects were found to be very weak for shallow flows which make the contaminant spread gently along the flow. On the other hand, for deep flows, it was found that these decelerating effects are very strong. It was also found that the sediment transport in the three directions is far from isotropic.

The present survey shows that the available models analysing sediment transport as a transferred scalar in meandering channels can not fully clarify the re-suspension process in the presence of secondary motion.

In this Chapter, the sediment transport in meandering channels is studied numerically. The distribution of concentration is presented to reveal its diversity compared to a straight channel.

5.2 Flow Simulation

To investigate the distribution of the suspended sediments in the meandering channel, the numerical analysis was performed in two sine-generated meandering channels. In the present case, the geometry of the meandering channels is the same as that shown in Figure 4.2, having initial deflection angles 45° and 95° respectively. The hydraulic conditions of the flow were similar to those of the previous chapter (see Table 4.1).

According to the results presented in the Chapter 3 of this thesis (subsection 3.5.1) the amount of suspended sediments in the water column was considerable for two dimensionless particle sizes, $d^+ = 1$ and 3 respectively; in these cases the buoyancy contribution to the momentum transport has been shown to be relevant. Thereby, the dimensionless particle sizes in this test were chosen to be consistent with those ones in Chapter 3 ($d^+ = 1$ and 3).

Following the boundary conditions considered for the straight channel in Chapter 3, the reference concentration at the channel bed was prescribed as that of Equation 3.20. The zero concentration flux was applied at the lateral walls. The initial concentration in the flow domain was set to be zero. After the statistically steady state flow was established, the simulations were continued for 20 non-dimensional time units to provide a developed concentration field. For the each channel cases, the lateral distribution of suspended sediments is presented in the cross-sections defined in Figure 4.2.

5.3 Numerical Results

To study the nature of the suspended sediment transport in the meandering streams and point out the effect of the channel curvature on the lateral dispersion of the scalar field, the suspended sediments contour plots are presented in this section.

Figure 5.1 shows the suspended sediment concentration contour plots for two grain sizes in the case 45°. The figures show that the contour pattern is not uniform in the lateral direction due to the complex pattern of the velocity field in the meandering streams. It is observed that there is a noticeable gradient of the suspended concentration from the inner to the outer bank of the channel. Close comparison of the lateral suspended concentration distributions shows that, in the first half of the bend, the amount of suspended concentration at the outer bank is larger than that of observed at the inner bank.

As noted earlier for the straight channel, the suspended sediment concentration is a function of erosion rate from the channel bed and deposition flux. Besides the mentioned factors, in meandering streams, the suspended load is strongly influenced by the curvature-induced secondary motion in

the flow domain.

Addressing subsection 4.5.4, the high bed shear stress region (and accordingly the high erosion flux) is situated at the inner bank near the bend apex. As shown in the contour plots, the amount of suspended sediments decreases moving towards the inner bank (in the first half of the bend). This behaviour may be attributed to the secondary circulation (see Figure 4.6) existing at the outer bank and moving towards the inner bank, thus lifting the particles and reducing their deposition quantity. The strength of the main secondary motion diminished due to the formation of a new secondary cell (which counter-rotates to the main one) from the inner bank in cross-section 3. This reflects a gradually reduction of the suspended load in the outer bank region and an enhancement in the inner bank region. Accordingly, as the flow passes through the bend, the region of high suspended load shifts from the outer to the inner bank.

Increasing the grain size, the amount of the suspended sediments concentration decreases. This is attributed to a decrease of the erosion flux (according to the higher critical bed shear stress) and an increase of the deposition flux (due to the larger setting velocity).

Similar comparisons are shown in Figure 5.2 for the case 95°, in which the suspended sediments concentration follows the similar pattern as the latter case. However, there are some quantitative differences on the locations and amount of the high-concentration regions.

As the channel sinuosity increases (95°), the bed shear stress and accordingly, the erosion flux increase. Moreover, the presence of a secondary flow stronger than that of the case 45° results in the higher net suspended sediments inside the water column. Also, The locus for the high suspended concentration slightly changes. This happens due to the shift of the new developed secondary cell in the inner bank to the channel upstream (cross-section 2).

Same as the latter case, it can be observed that the total amount of the suspended sediments decreases for the larger grain size.

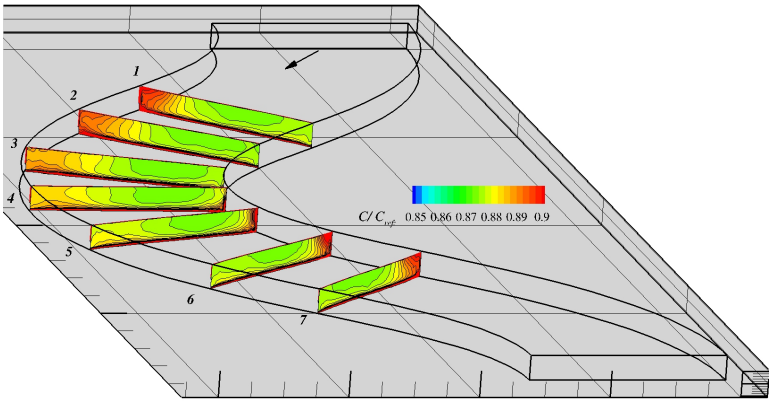

(a) $d^+ = 1$

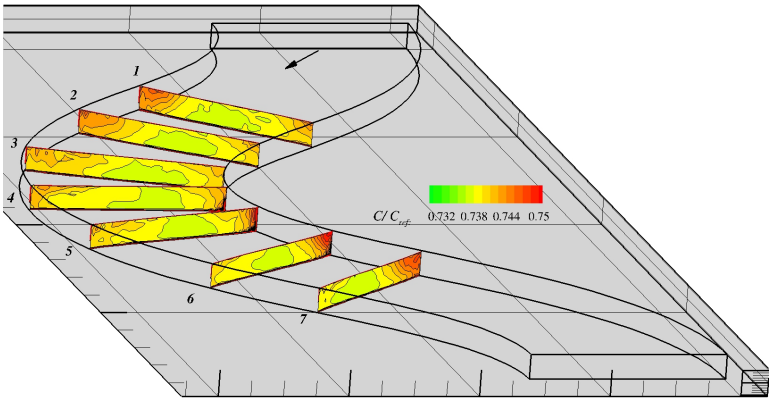

(b) $d^+ = 3$

Figure 5.1: Contour plot of suspended sediment concentration along the channel in 45° meandering channel for two particle sizes.

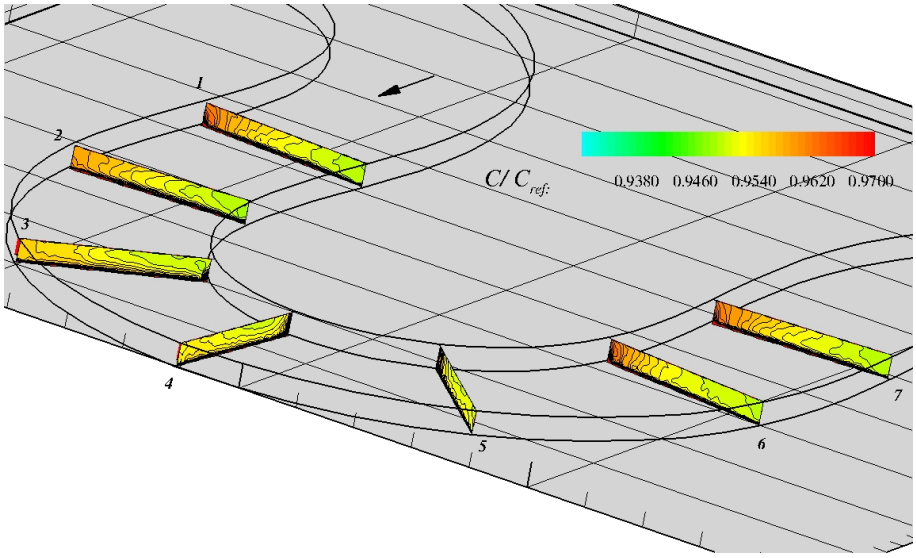

(a) $d^+ = 1$

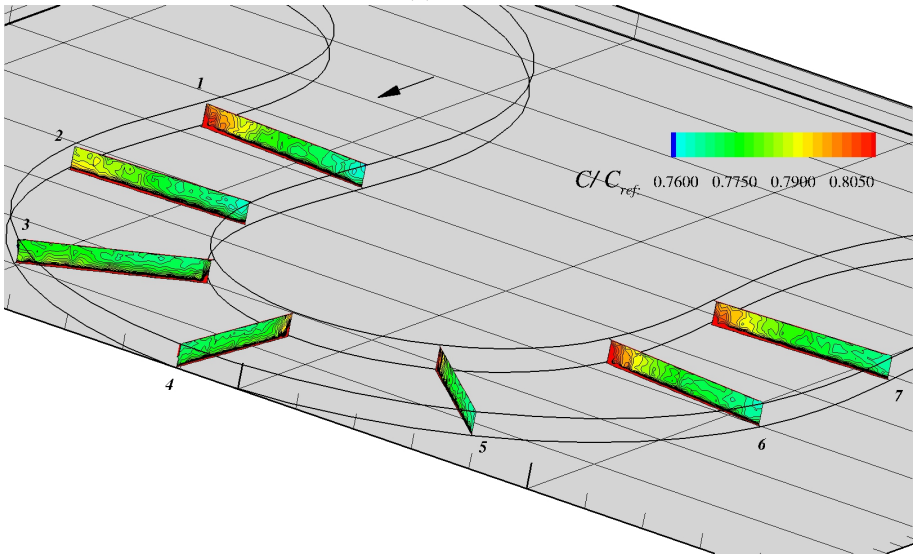

(b) $d^+ = 3$

Figure 5.2: Contour plot of suspended sediment concentration along the channel in 95° meandering channel for two particle sizes.

5.4 Conclusions

Flow in meandering channels is clearly highlighted due to the complex three-dimensional nature of these flows. The curvature-induced secondary motion in meandering channels causes considerable lateral spreading of the dispersed phase so that mixing is much stronger than in a straight channel. As a consequence, the transverse distribution of suspended sediments is expected to be non-uniform.

A numerical investigation was presented in this chapter to provide us the opportunity to understand the behavior and the pattern of suspended sediment of different sizes across a meandering channel. The analysis discussed in the present chapter has to be considered preliminary. Additional investigations will be performed in the upcoming future.

It was found that the bed shear stresses and secondary circulations were responsible for the concentration patterns of the suspended sediments over the cross-sections. The bed shear stress increased towards the inner bank of the apex, resulting in higher erosion flux. On the other hand, the secondary circulation caused lifting of fine particles from the outer regions.

Comparison of the suspended sediment concentration contours in the case 45° and 95° showed that the amount of the suspended sediment concentration decreased due to the weaker circulatory motion and lower erosion flux for the mild curvature channel.

Appendices

Appendix A

Analyzing the Free Surface Shape by Variational Method

A.1 Review of Yalin and da Silva' s Variational Equation

A.1.1 Theoretical Formulation

Yalin and da Silva [2001] postulated 'the free surface is shaped by nature in such a way as to render its variations (in every direction) to occur in the *smoothest* possible manner'. According to these authors, this condition would minimize the pressure variations from one location to another within the fluid, providing the *most comfortable* flow condition. Considering this, they have stated that the free surface should be such that:

$$\int_{\Omega} J_r^2 d\Omega \rightarrow \min, \tag{A.1}$$

where $J_r = \partial z_f / \partial r$ is the radial free surface slope ($z_f = z_b + h$; see Figure A.2) and $d\Omega$ is the (infinitesimal) area $dl.dn$ as shown in Figure A.1.

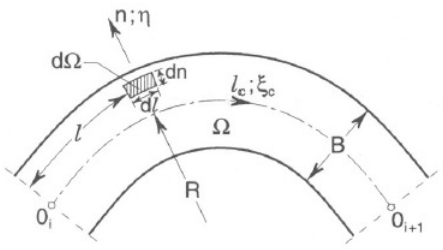

Figure A.1: Plan area Ω of a meander loop (from Yalin and da Silva [2001].)

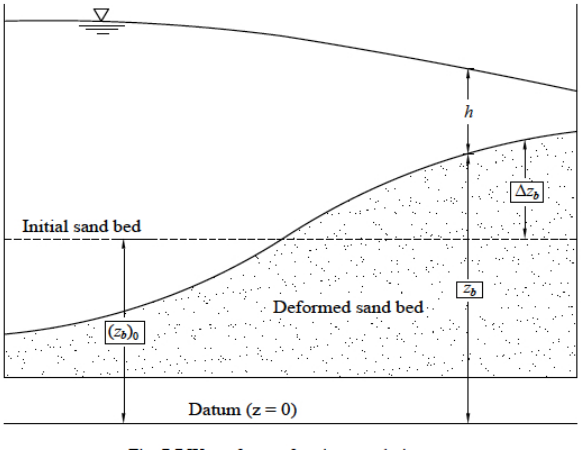

Figure A.2: Water free surface in meandering channel.

Introducing the notation

$$H = \frac{z_f}{B}(= \frac{z_{fb}}{B} + \frac{h}{B}) \ , \ H_\eta = \frac{\partial H}{\partial \eta}, \tag{A.2}$$

where $\eta = n/B$ and taking into account that for any quantity A, $\partial A/\partial r = \partial A/\partial n$, these authors wrote:

$$J_r = \frac{\partial z_f}{\partial r} = \frac{\partial z_f}{\partial n} = \frac{\partial (z_f/B)}{\partial (n/B)} = \frac{\partial H}{\partial \eta} = H_\eta, \tag{A.3}$$

on the other hand,

$$d\Omega = dl.dn = (1 + \frac{n}{R})dl_c.dn = (1 + \eta\frac{B}{R})LBd\xi_c d\eta. \tag{A.4}$$

Here B/R is a known function of ξ_c given as:

$$\frac{B}{R} = [\theta_0 J_0(\theta_0)] \sin(2\pi\xi_c) = f(\xi_c). \tag{A.5}$$

Substituting of Equation A.3 and Equation A.4. in Equation A.1 yields

$$LB \int_0^1 [\int_{-1/2}^{+1/2} H_\eta^2 (1 + f(\xi_c).\eta) d\eta] d\xi_c \to \min, \tag{A.6}$$

where $f(\xi_c)$ stands for B/R. Since $f(\xi_c)$ is known, Yalin and da Silva [2001] replaced the minimization above by:

$$\int_{-1/2}^{+1/2} H_\eta^2 (1 + f(\xi_c).\eta) d\eta \to \min, \tag{A.7}$$

defining $F = H_\eta^2(1 + f(\xi_c).\eta)d\eta$, the determination of H_η from Equation A.7, which is valid for all ξ_c-sections, is a variational problem. Therefore, a solution to the problem was obtained by these authors by substituting the integrated F into Euler equation, which yields:

$$\frac{\partial F}{\partial H} - \frac{\partial}{\partial \eta}(\frac{\partial F}{\partial H_\eta}) = 0. \tag{A.8}$$

Considering that F is a function of H_η and η, *Yalin and da Silva* further simplified Equation A.8 into:

$$\frac{\partial}{\partial \eta}(\frac{\partial F}{\partial H_\eta}) = 0, \tag{A.9}$$

which can be written in terms of $H(= z_f/B)$ as

$$\frac{\partial^2 H}{\partial \eta^2} + (\frac{f(\xi_c)}{1 + f(\xi_c).\eta}).\frac{\partial H}{\partial \eta} = 0, \tag{A.10}$$

or in terms of z_f

$$\frac{\partial^2 z_f}{\partial n^2} + (\frac{1}{R + n}).\frac{\partial z_f}{\partial n} = 0. \tag{A.11}$$

Equation A.11 gives, for any cross-section, the (cross-sectional) distribution of $z_f(= z_b + h)$ in a meandering channel of any given bed geometry. In the particular case of a flat bed ($\partial z_b/\partial n = 0$), Equation A.11 can be written as:

$$\frac{\partial^2 h}{\partial n^2} + (\frac{1}{R + n}).\frac{\partial h}{\partial n} = 0. \tag{A.12}$$

Solving analytically Equation A.11, Yalin and da Silva [2001] obtained the following equation for the flow depth h:

$$\frac{h}{h_m} - 1 = 2\alpha_* Fr \frac{f(\xi_c)}{ln(a/b)}[F(\xi_c, \eta) - \int_{-1/2}^{+1/2} F(\xi_c, \eta)d\eta] + K, \tag{A.13}$$

where h_m is cross-sectional averaged value of h and

$$Fr = \frac{u_m^2}{gh_m}\ ,\ F(\xi_c, \eta) = ln(1 + f(\xi_c).\eta),$$

$$a = 1 + f(\xi_c),\ b = 1 - f(\xi_c),$$

$$K = -\frac{1}{h_m}(\int_{-1/2}^{+1/2} \Delta z_b d\eta - \Delta z_b),$$

where $\Delta z_b = z_b - z_0$. Note that if the bed is flat, then $K = 0$.

A.1.2 Ability and Limitation of Variational Method

To investigate the adequacy of Yalin and da Silva 's variational method the comparison of the computed profile and the measurement by da Silva [1995] is shown in Figure A.3 for two different sinuosities.

It is remarkable that the computed profile is not satisfactory follows the curved pattern of measured data for water surface. Thereby, the variational method does not provide an adequate representation of free-surface shape. This fact leads us to present a modified equation in next section to have more realistic results.

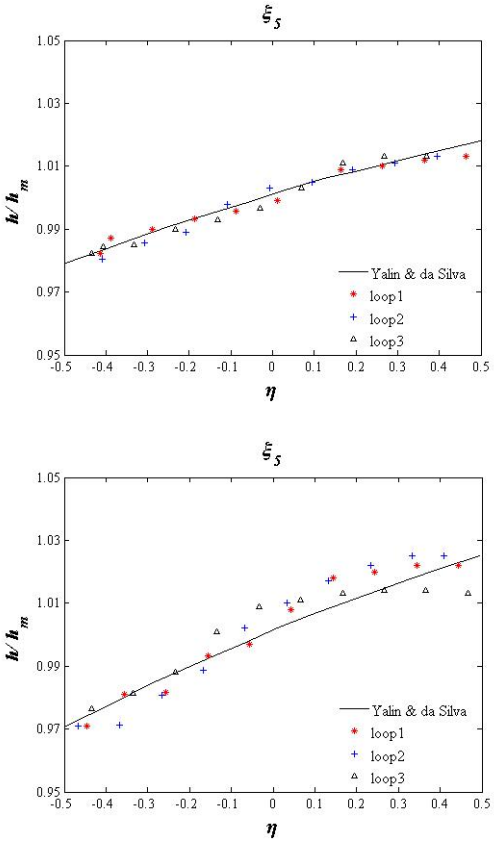

Figure A.3: Measured and computed water surface profiles at cross-section 5 (Apex) for channel (a) 30°, (b) 110°.

A.2 Present Modified Form of Variational Equation

A.2.1 Introduction of Modified Variational Equation

Consider the below equation,

$$\int_{-1/2}^{+1/2} H_\eta^2(1+f(\xi_c).\eta)d\eta \rightarrow \ min, \tag{A.14}$$

where $H_\eta = \partial H/\partial\eta = \partial(z_f/B)/\partial\eta$ and $f(\xi_c) = B/R$. In above equation, the term $(1+f(\xi).\eta)$ is always positive. considering this, and taking into account that H_η is always positive as well, we start by replacing the minimization above by:

$$\int_{-1/2}^{+1/2} H_\eta^2(1+f(\xi_c).\eta)^{k+1}d\eta \rightarrow \ min, \tag{A.15}$$

where k can be any positive number. Since for any specified cross-section ξ_c, the function $f(\xi_c)$ has a certain known value, the integrand $F(= H_\eta^2(1+f(\xi_c).\eta)^{k+1})$ is to be treated as an unknown function of H_η and η only. Following the same technique adopted by Yalin and da Silva [2001] in their derivation, by substituting F into the Euler equation, one obtains:

$$\frac{\partial}{\partial\eta}(2H_\eta(1+f(\xi_c).\eta)^{k+1}) = 0, \tag{A.16}$$

i.e

$$\frac{\partial}{\partial\eta}(H_\eta(1+f(\xi_c).\eta)^{k+1}) = 0, \tag{A.17}$$

which yields

$$(\frac{\partial H}{\partial\eta})(k+1)(1+f(\xi_c).\eta)^k f(\xi_c) + (1+f(\xi_c).\eta)^{k+1}\frac{\partial^2 H}{\partial\eta^2} = 0. \tag{A.18}$$

Division of Equation A.18 by $(1+f(\xi_c).\eta)^{k+1}$ yields

$$\frac{\partial^2 H}{\partial\eta^2} + (k+1)(\frac{f(\xi_c)}{1+f(\xi_c).\eta})\cdot\frac{\partial H}{\partial\eta} = 0, \tag{A.19}$$

or equivalently,

$$\frac{\partial^2 z_f}{\partial n^2} + (k+1)(\frac{1}{R+n})\cdot\frac{\partial z_f}{\partial n} = 0. \tag{A.20}$$

Note that for the case of a flat bed and introducing $\phi_h = h/h_m$, Equation A.20 can be written as:

$$\frac{\partial^2\phi_h}{\partial\eta^2} + (k+1)(\frac{f(\xi_c)}{1+f(\xi_c).\eta})\cdot\frac{\partial\phi_h}{\partial\eta} = 0. \tag{A.21}$$

The numerical method to solve Equation A.21 is described in the following section.

A.2.2 Numerical Solution

A.2.2.1 Flat Bed

Equation A.21 is solved by adopting a finite difference scheme on a computational grid $(i\Delta\xi; j\delta\eta)$ defined as shown in Figure A.4 [El-Tahawy, 2004]. The boundary conditions used in solution of Equation A.21 are as follows:

$$\int_{-1/2}^{1/2} \phi_h d\eta = 1, \tag{A.22}$$

$$\Delta\phi_{h_s} = \alpha_* \frac{u_m^2}{h_m g}.f(\xi_c) = dimensionless\ super-elevation, \tag{A.23}$$

where α_* is a factor close to unity which depends -at least- on the channel sinuosity.

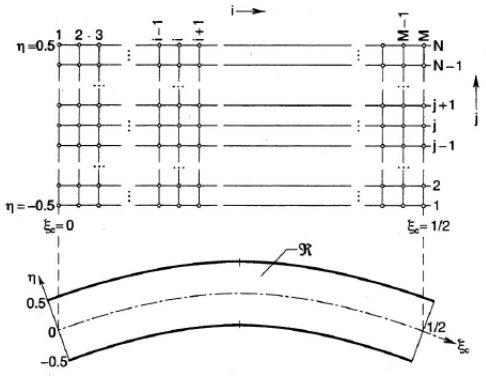

Figure A.4: Computational grid used in hydrodynamic model 'LOOP' from da Silva [1995].

Using central differencing method for second order derivative and backward differencing for the first order derivative, in Equation A.21, i.e. by adopting

$$\frac{\partial^2\phi_h}{\partial\eta^2} = \frac{(\phi_h)_i^{j+1} - 2(\phi_h)_i^j + (\phi_h)_i^{j-1}}{\Delta\eta^2}, \tag{A.24}$$

$$\frac{\partial\phi_h}{\partial\eta} = \frac{(\phi_h)_i^j - (\phi_h)_i^{j-1}}{\Delta\eta}. \tag{A.25}$$

One can express Equation A.21 as

$$\frac{(\phi_h)_i^{j+1} - 2(\phi_h)_i^j + (\phi_h)_i^{j-1}}{\Delta\eta^2} + (k+1)\left(\frac{f(\xi_c)}{1+f(\xi_c).\eta}\right)\cdot\frac{(\phi_h)_i^j - (\phi_h)_i^{j-1}}{\Delta\eta} = 0, \tag{A.26}$$

which after rearrangement it yields:

$$K_1.(\phi_h)_i^{j-1} - (\phi_h)_i^j + K_2.(\phi_h)_i^{j+1} = 0, \tag{A.27}$$

where $K_1 = \frac{C+1}{2C+1}$, $K_2 = \frac{C}{2C+1}$ and $C = -\frac{1/f(\xi_c)+\eta}{\Delta\eta(k+1)}$.

The application of Equation A.27 for all points $j = 2, 3, 4..., N-1$ on a given grid-line (cross-section) i, together with the two aforementioned boundary conditions, leads to a system of N equations. The value of $(\phi_h)_i^j$ for all $j = 1, ..., N$ on the given grid-line i are obtained as the solution of this system of N equations. The Gaussian elimination method is used to solve this system.

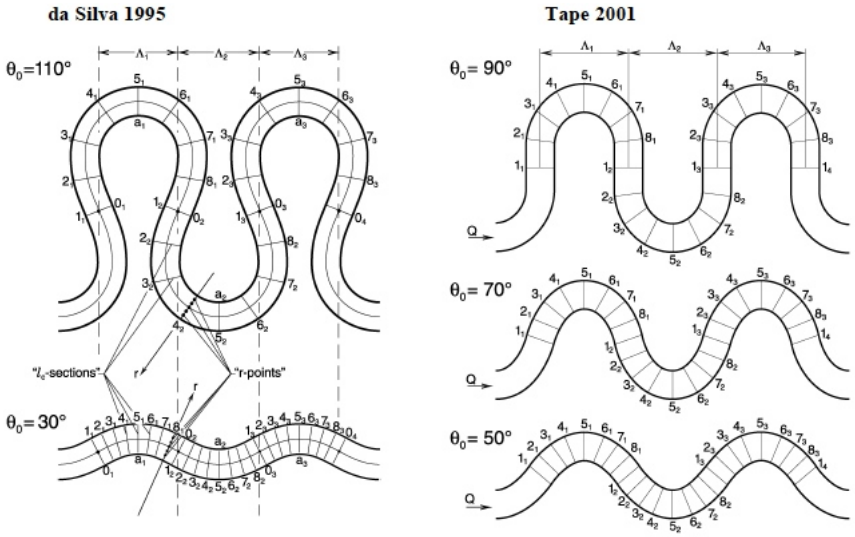

Figure A.5: Exprimental channels by da Silva [1995] and Tape [2001].

A.2.2.2 Deformed Bed

In the previous section, we considered $\partial z_b/\partial n = 0$ for the case of a flat bed. Another problem in estimating the water surface profile in bending river is accounting the bed deformation across the channel. Let's start out the derivation by recalling Equation A.20 and substituting $H_\eta = z_f/B = (z_b + h)/B$ such that:

$$\frac{\partial^2 z_b}{\partial n^2} + \frac{\partial^2 h}{\partial n^2} + (k+1)(\frac{1}{R+n}) \cdot [\frac{\partial z_b}{\partial n} + \frac{\partial h}{\partial n}] = 0. \tag{A.28}$$

By assuming $\phi_h = h/h_m$ and $\phi_z = z_b/h_m$ it yields:

$$\frac{\partial^2 \phi_h}{\partial \eta^2} + (k+1)(\frac{f(\xi_c)}{1+f(\xi_c).\eta}) \cdot \frac{\partial \phi_h}{\partial \eta} + C_z = 0, \tag{A.29}$$

where C_z is a known value related to the bed deformation as:

$$C_z = \frac{\partial^2 \phi_z}{\partial \eta^2} + (k+1)\left(\frac{f(\xi_c)}{1+f(\xi_c).\eta}\right) \cdot \frac{\partial \phi_z}{\partial \eta}.$$

Following the same numerical method applied in subsubsection A.2.2.1, the above equation is simplified to:

$$K_1.(\phi_h)_i^{j-1} - (\phi_h)_i^j + K_2.(\phi_h)_i^{j+1} = Cz.K_2.\Delta\eta^2. \tag{A.30}$$

The boundary condition is also modified as follows:

$$\int_{-B/2}^{B/2} (z_h - z_b)dn = h_m \Rightarrow \int_{-1/2}^{1/2} (\phi_h - \phi_z)d\eta = 1, \tag{A.31}$$

$$\Delta\phi_{h_s} = \alpha_* \frac{u_m^2}{h_m g}.f(\xi_c) = dimensionless\ superelevation, \tag{A.32}$$

A.3 Comparison with Experiments

A.3.1 Sine-generated Channels with Flat Bed

To investigate the adequacy of Yalin and da Silva's modified variational equation, the results are presented in comparison with measurement of da Silva [1995] (in a 30° and a 110° sine-generated channels) and Tape [2001] (in 50°, 70° *and* 90° channels). The hydraulic conditions of these experiments are summarized in Table A.2. The measured value of h/h_m at cross-sections ξ_2 to ξ_7 (see Figure A.5 for cross-sections location along the channel) are plotted in Figure A.6 to Figure A.10. The calculated water surface profile is shown with solid line.

The results are also presented in comparison with a free surface prediction method using by da Silva [1995] for channel with $\theta_0 = 30°$ and 110° in Figure A.11.

Table A.1: Cross-section coordinates

Cross-section	2	3	4	5	6	7	8
ξ_c	0.0625	0.125	0.1875	0.25	0.3125	0.375	0.4375

Table A.2: Summery of hydraulic conditions.

Channel	B/R_a	h_{av}	u_{uv}	B/hav	α_*	Re	Fr
30°	0.49	3.20	0.164	12.5	1.03	5250	0.086
50°	0.71	3.14	0.201	12.7	1.2	6325	0.131
70°	0.81	3.08	0.149	13.0	1.5	4600	0.073
90°	0.74	3.05	0.181	13.1	1.2	5525	0.109
110°	0.52	3.00	0.167	13.3	1.03	5025	0.095

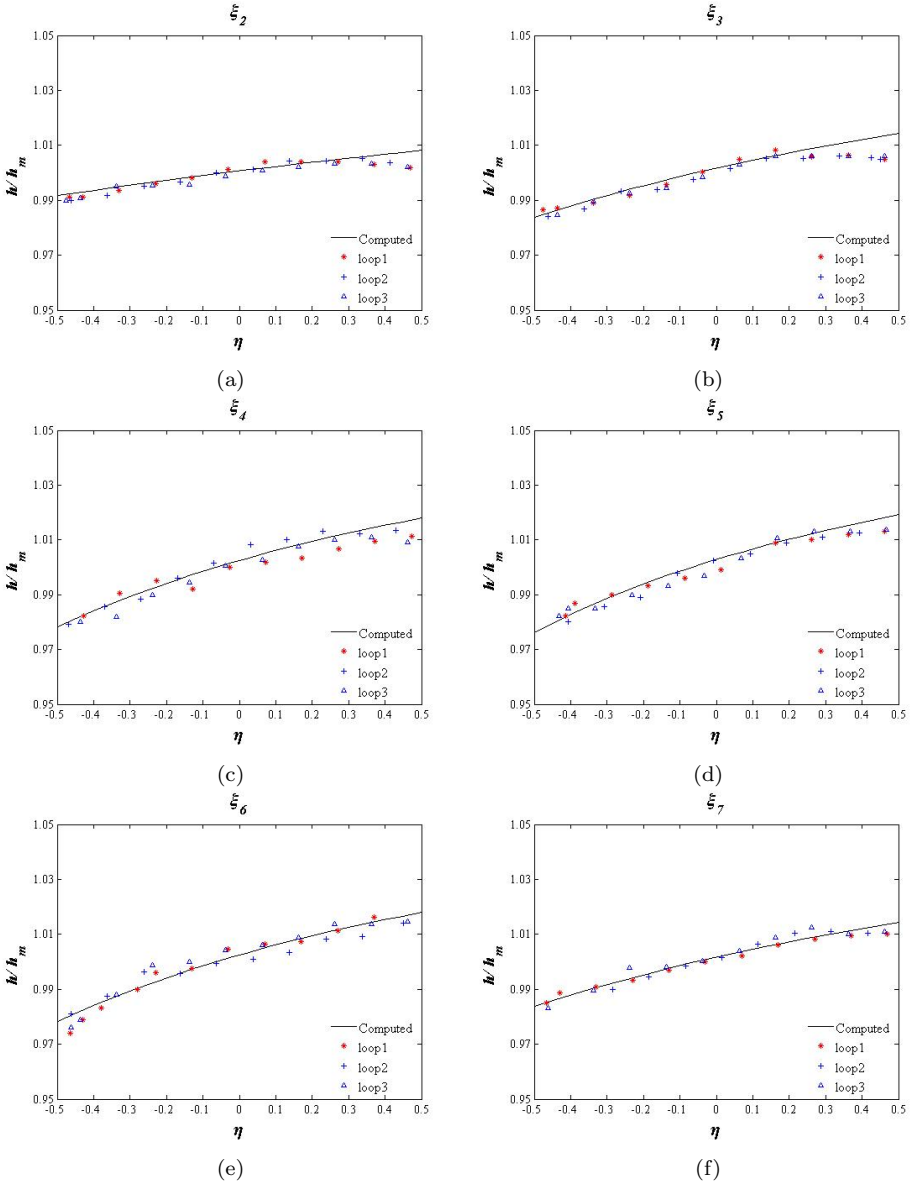

Figure A.6: Measured and computed water surface profiles for channel 30° at cross-sections 2 to 7.

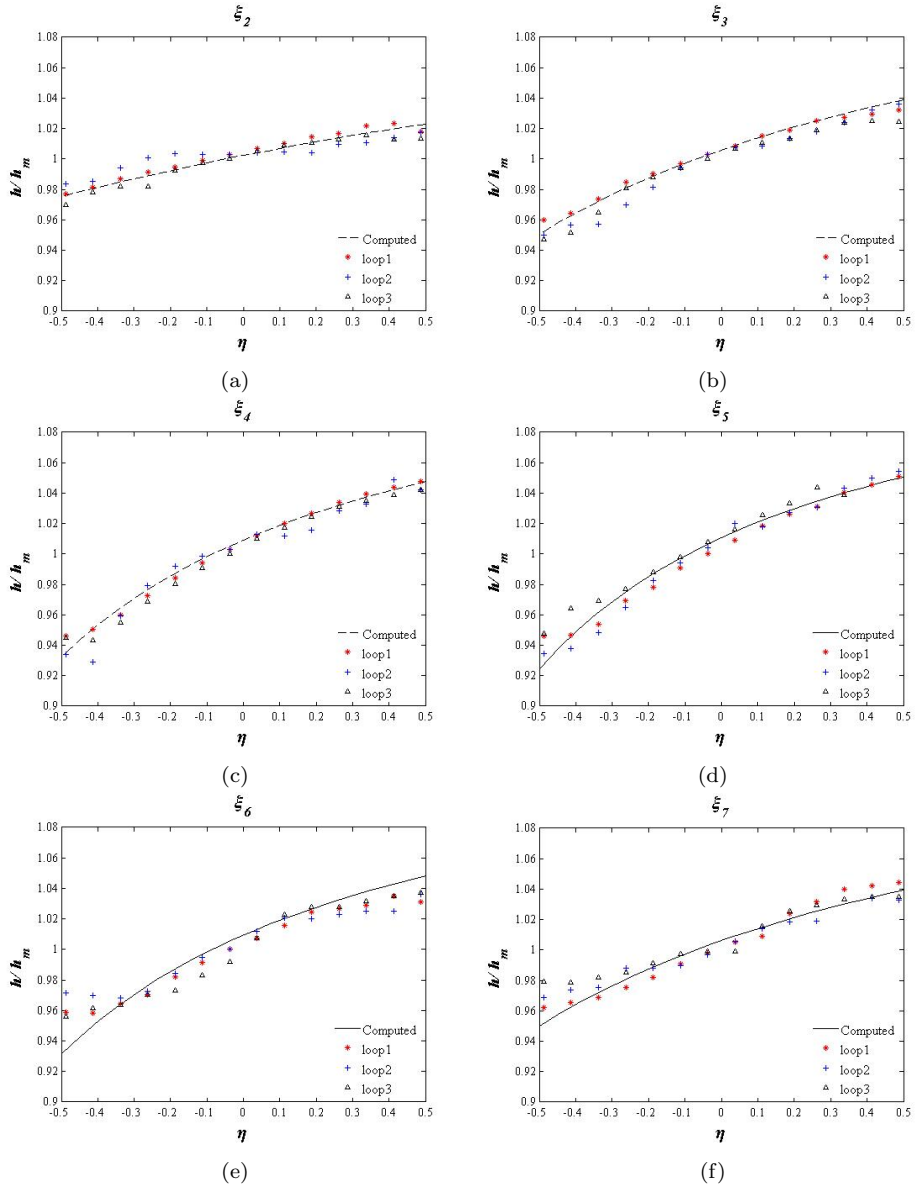

Figure A.7: Measured and computed water surface profiles for channel 50° at cross-sections 2 to 7.

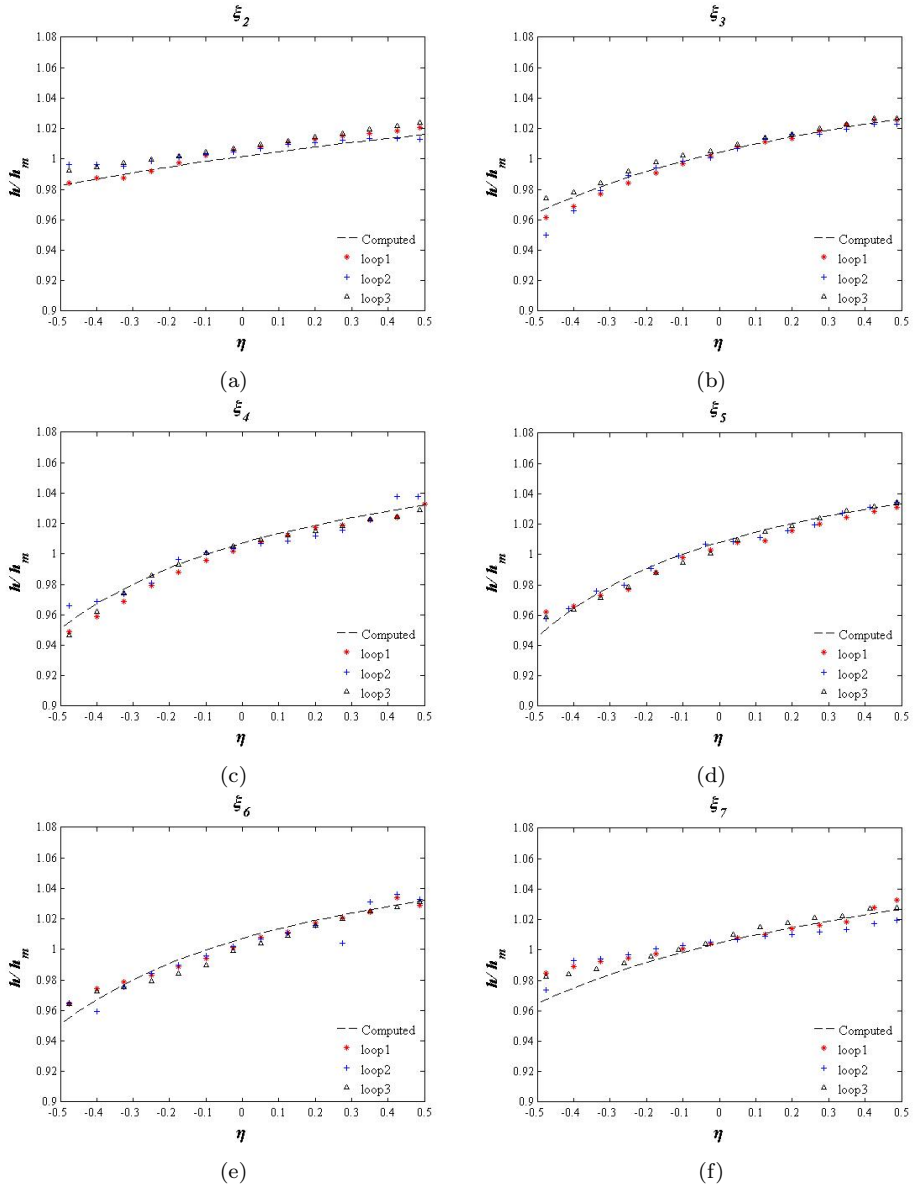

Figure A.8: Measured and computed water surface profiles for channel 70° at cross-sections 2 to 7.

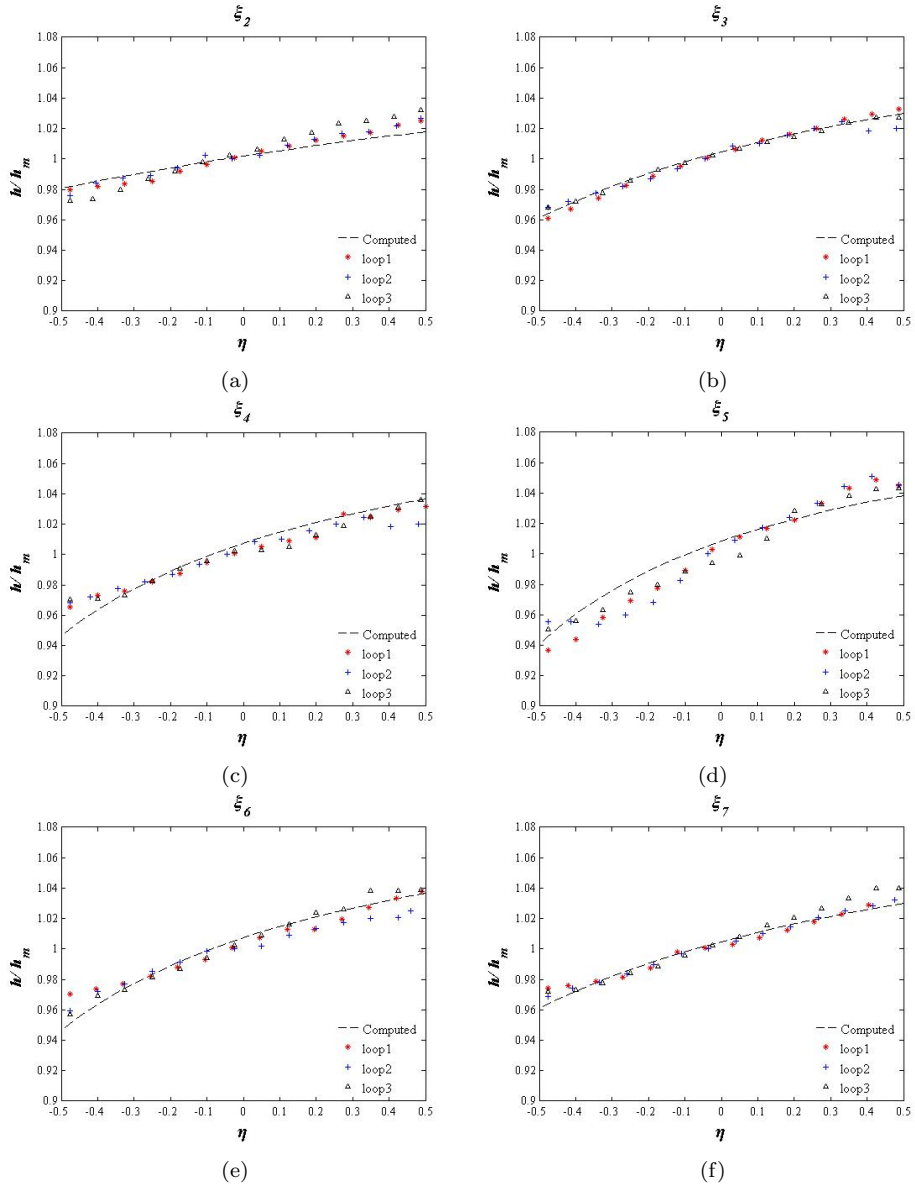

Figure A.9: Measured and computed water surface profiles for channel 90° at cross-sections 2 to 7.

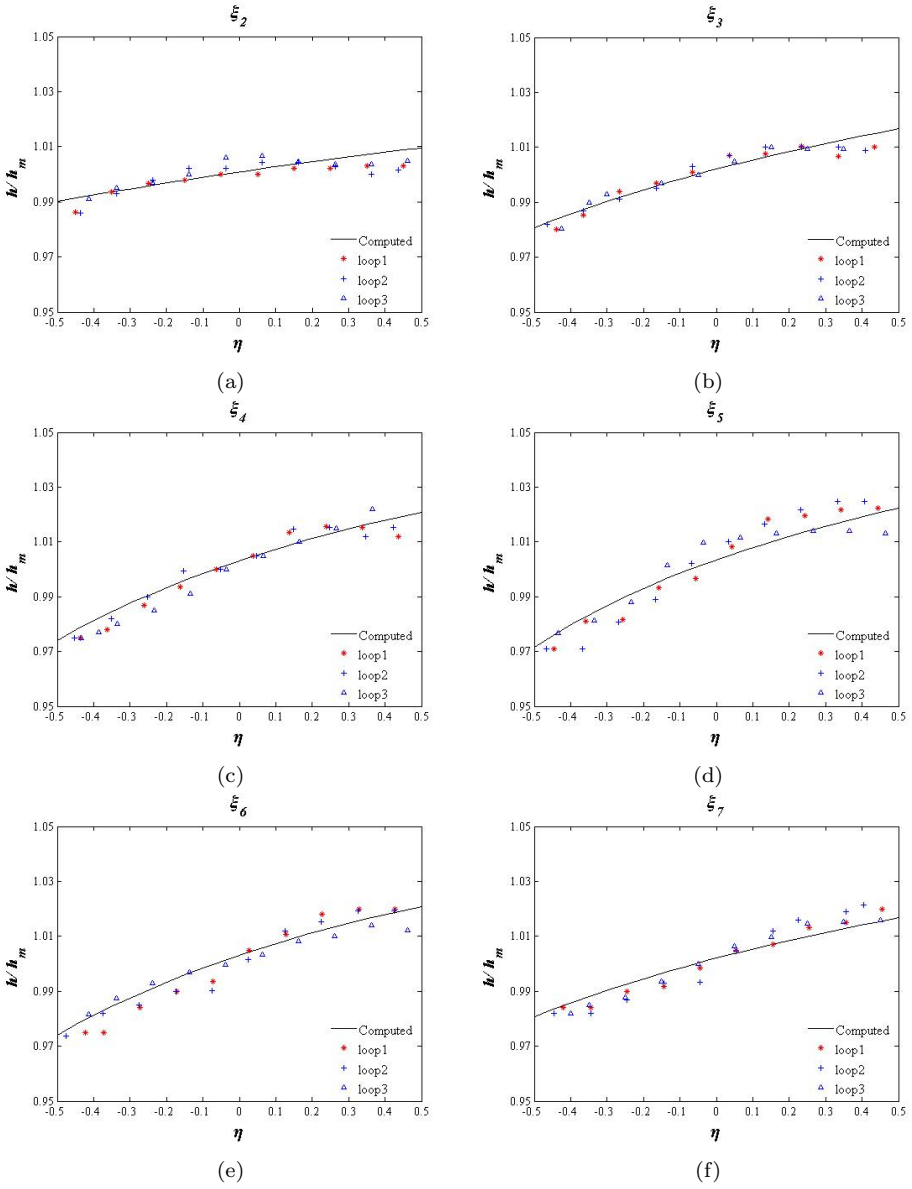

Figure A.10: Measured and computed water surface profiles for channel 110° at cross-sections 2 to 7.

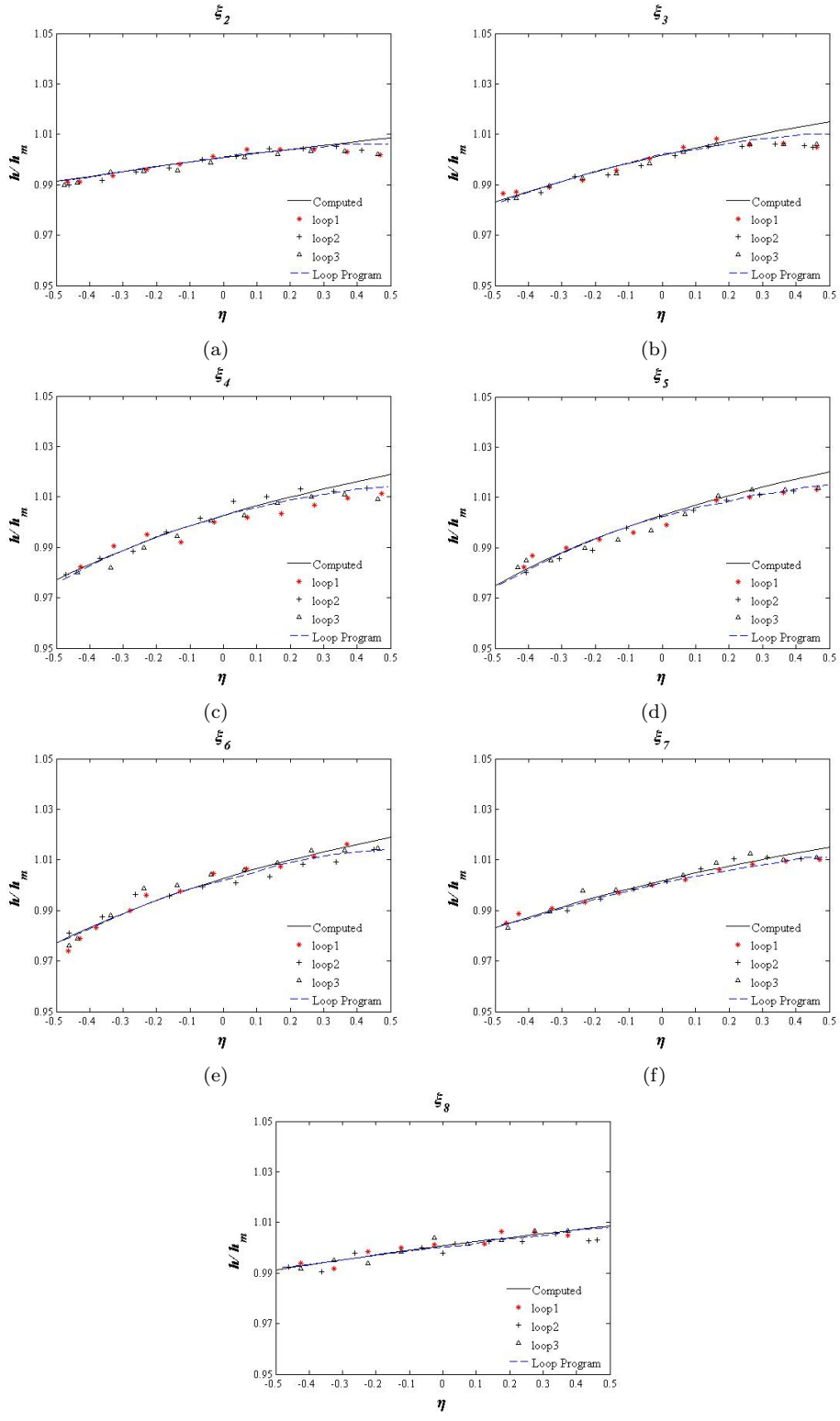

Figure A.11: Measured and computed water surface profiles in compared to calculated values by da Silva [1995] at cross-sections 2 to 8 for channel 30°

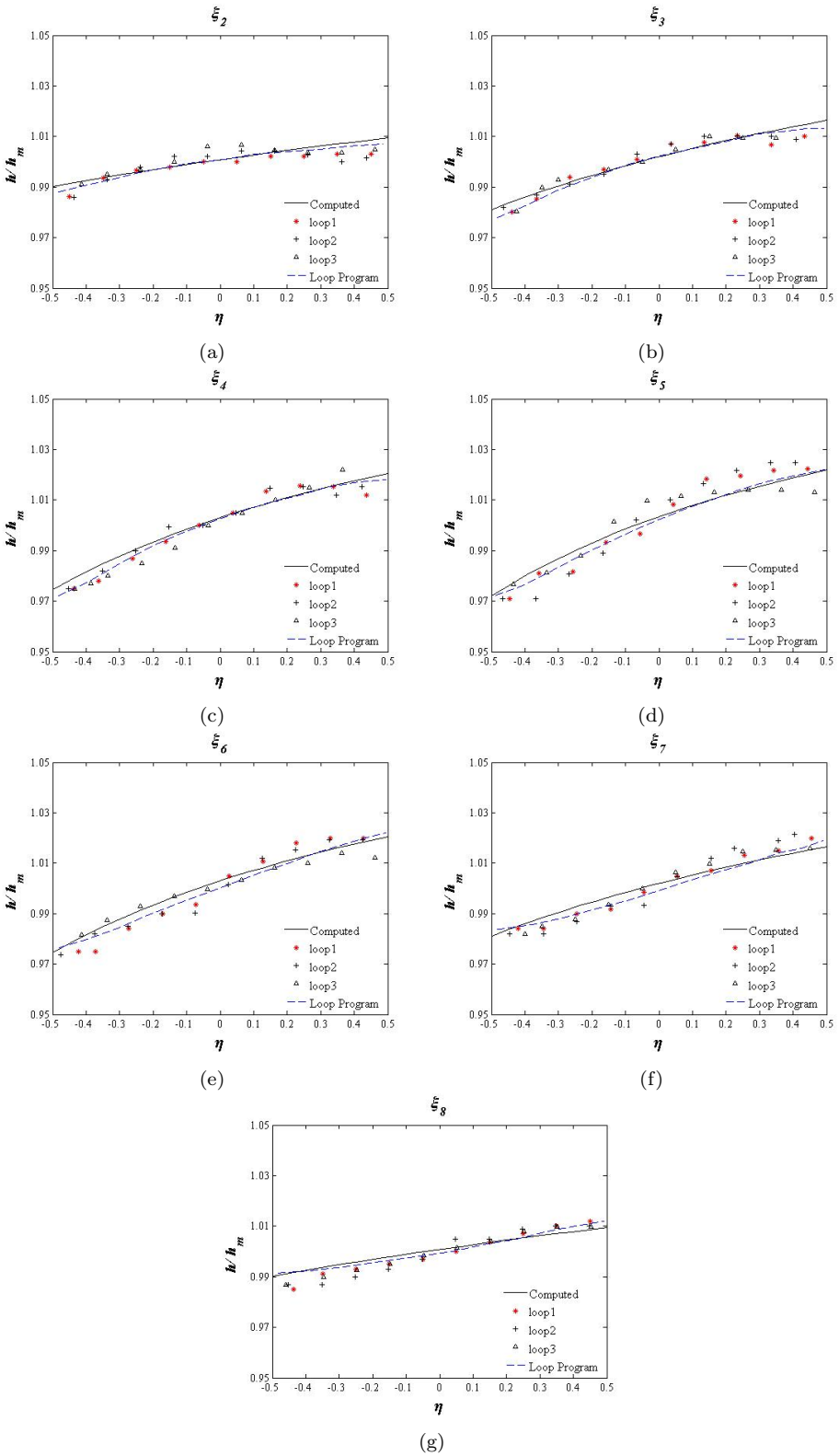

Figure A.12: Measured and computed water surface profiles in compared to calculated values by da Silva [1995] at cross-sections 2 to 8 for channel 110°.

A.3.2 Circular Channel with Flat Bed

In this section the validity of the present modified variational equation is evaluated in circular channels, by a comparison with the data measured by Rozovskii [1957] in a 180° circular bend shown in Figure A.13a. The flow rate was $Q = 12.3\, l/s$ and the mean height of channel was $h_m = 0.06\, m$. The measured and computed water surface profiles are shown in Figure A.13c for the central cross-section of the bend. The value of $\alpha_* = 1.2$ in this particular case to adopt to the collected data.

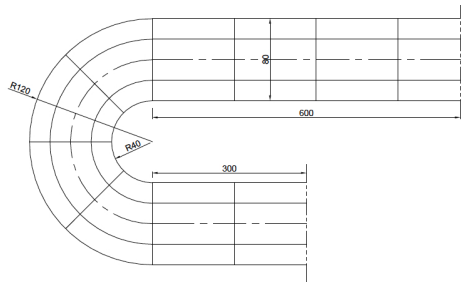

(a)

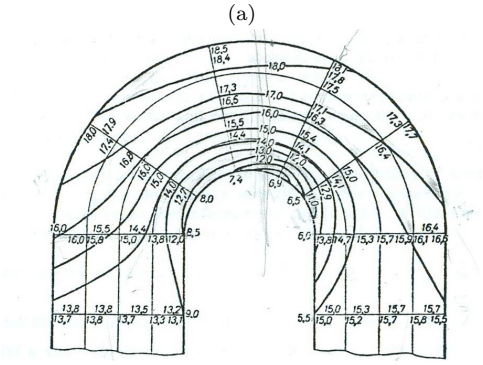

(b)

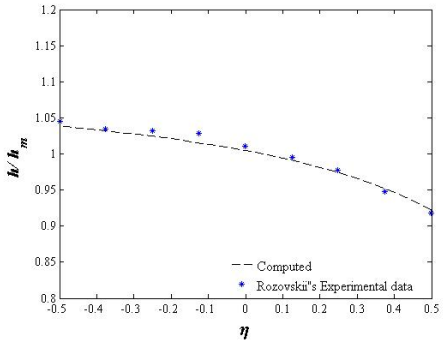

(c)

Figure A.13: (a) Geometry of Rozovskii's experimental channel 1961, (b) Free surface iso-surface contour of Rozovskii 's experimental channel 1961, (c) Measured and computed water surface profiles; flow in 180°.

The above cross-section is located in fully developed part of the bend where we can apply the free surface formulation for meandering curve with fix ratio for B/R.

To estimate the free surface shape in transitional part of the bend where $0 \leqslant B/R \leqslant (B/R)_{max}$, we introduce a sigmoid function curve which provides a description of B/R along the transitional part. The curve defines as :

$$Y = \frac{A1}{1 + exp[A2 * (A3 - X)]} + A4, \tag{A.33}$$

where $A1$ and $A4$ define the boundary value for B/R, $A3$ is the point with slope $B = A1.A2/4$ and $A2$ is gain factor (Figure A.14a).

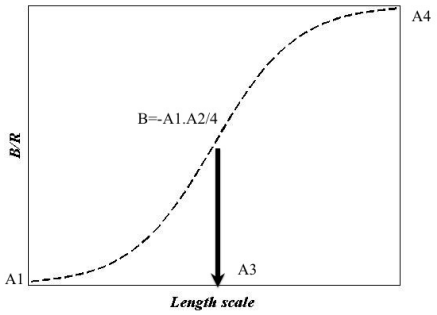

(a)

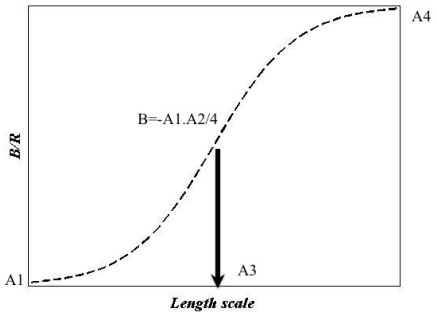

(b)

Figure A.14: (a) Typical sigmoid function applied to transient part of a circular channel, (b) Sigmoid function used for Rozovskii circular channel.

The above variables for sigmoid curve are obtained from Rozovskii 's data (Figure A.13b). The Reference point is fixed at level 5 (see Rozovskii [1957] for more details) and the length is calculating along the central streamwise direction. $A3$ is chosen to be at the level 6 (Figure A.14b).

The modified variational method is applied for cross-sections 5.5, 6, 6.5 and fitted to the experimental data observed by Rozovskii [1957] for same

level (Figure A.15). The comparison shows a good agreement between predicted and observed free surface shape.

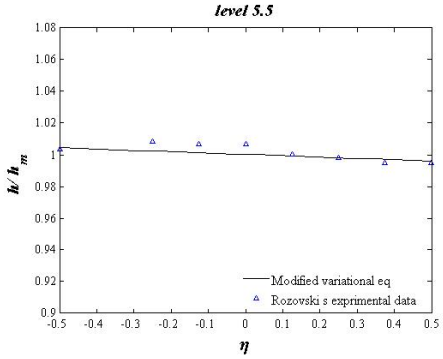

(a)

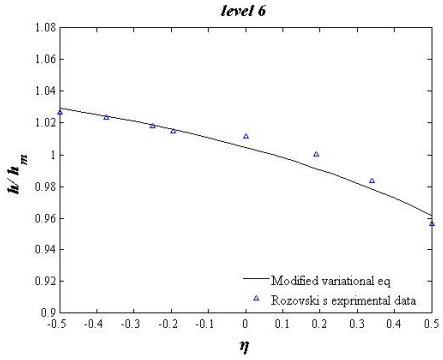

(b)

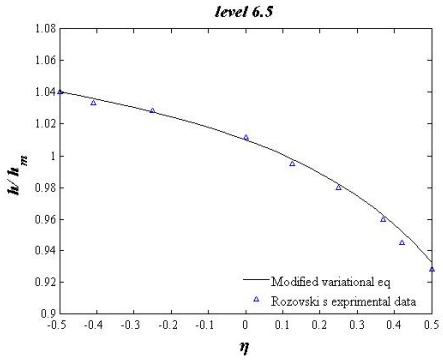

(c)

Figure A.15: Comparison of predicted free surface shape to experimental data of Rozovskii [1957] for transient part of circular channel.

A.3.3 Natural Streams

In order to validate the modified variational method with deformed bed shape, the predicated profile will compare to the data presented on the *Muddy Creek* by Dietrich and Smith [1983]. Figure A.16a shows the section locations through the bend. The Muddy Creek study bend during most year of measurement had a water surface slope of 0.0014, a mean depth and velocity of 40 cm and 55 cm/sec. The channel had a minimum radius of curvature to width ration of 1.5. The geometry of Muddy Creek is simulated by a sine-generated curve with $\theta_0 = 68°$ (Figure A.16b).

The observed data collected at several cross-sections of Muddy Creek meander (see Table A.3). Taking into the account the bed deformation in the modified variational method, the estimated results for surface elevation are presented in comparison with the observed and predicted values at Muddy Creek (Dietrich et al. [1979]) in Figure A.17.

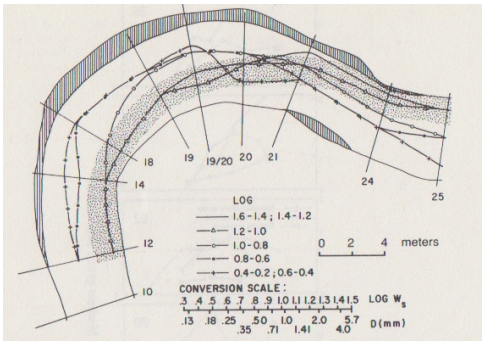

(a)

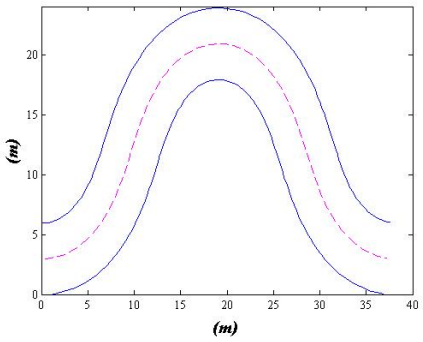

(b)

Figure A.16: (a) Map of Muddy Creek bend with measurement cross-sections, (b) sine-generated meander geometry estimated for Muddy Creek.

Table A.3: Cross-section coordinates at Muddy Creek.

Cross-section	12	14	18	19	20	22	24
ξ_c	0.05	0.12	0.16	0.23	0.31	0.36	0.4

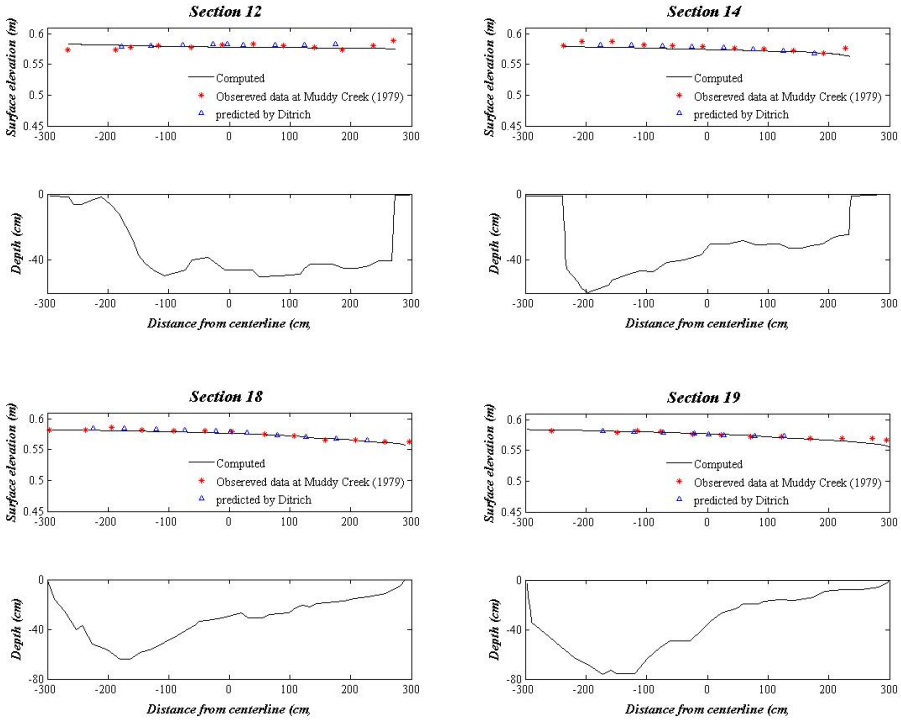

Figure A.17: Measured and predicted water surface profiles in Muddy Creek (Dietrich et al. [1979]) in compared to calculated values by da Silva [1995] at cross-sections 12 to 19.

Bibliography

J. D. Abad and M. H. Garcia. Experiments in a high-amplitude kinoshita meandering channel: 2. implications of bend orientation on bed morphodynamics. *Water Resources Research*, 45(2), feb 2009. ISSN 00431397. doi: 10.1029/2008WR007017.

L. Amoudry. A review on coastal sediment transport modelling. Technical report, Proudman Oceanographic Laboratory, 2008.

V. Armenio and V. Fiorotto. The importance of the forces acting on particles in turbulent flows. *Physics of Fluids*, 13(8):2437, 2001. ISSN 10706631. doi: 10.1063/1.1385390.

V. Armenio and U. Piomelli. A lagrangian mixed subgrid-scale model in generalized coordinates. *Flow, Turbulence and Combustion*, 65(1):51–81, 2000. ISSN 13866184. doi: 10.1023/A:1009998919233.

V. Armenio and S. Sarkar. An investigation of stably stratified turbulent channel flow using large-eddy simulation. *Journal of Fluid Mechanics*, 459:1–42, may 2002. ISSN 0022-1120. doi: 10.1017/S0022112002007851.

A. D. Binns. *Nature and time-scale of bed morphological adjustments toward equilibrium in meandering streams: an experimental study.* PhD thesis, Queen's University, Kingston, Canada, 2012.

A. D. Binns and A. M. F. da Silva. Meandering bed development time: formulation and related experimental testing. *Advances in Water Resources*, 81:152–160, jul 2015. ISSN 03091708. doi: 10.1016/j.advwatres.2014.11.007.

K. Blanckaert and W. H. Graf. Momentum transport in sharp open-channel bends. *Journal of Hydraulic Engineering*, 130(3):186–198, mar 2004. ISSN 0733-9429. doi: 10.1061/(ASCE)0733-9429(2004)130:3(186).

R. Booij. Measurements and large eddy simulations of the flows in some curved flumes. *Journal of Turbulence*, 4, mar 2003. ISSN 1468-5248. doi: 10.1088/1468-5248/4/1/008.

J. Boxall, I. Guymer, and A. Marion. Transverse mixing in sinuous natural open channel flows. *Journal of Hydraulic Research*, 41(2):153–165, 2003. doi: 10.1080/00221680309499958.

M. Cellino and W. H. Graf. Sediment-laden flow in open-channels under noncapacity and capacity conditions. *Journal of Hydraulic Engineering*, 125(5):455–462, may 1999. ISSN 0733-9429. doi: 10.1061/(ASCE)0733-9429(1999)125:5(455).

Y. C. Chang. *Lateral mixing in meandering channels.* PhD thesis, 1971.

N. L. Coleman. Effects of suspended sediment on the open-channel velocity distribution. *Water Resources Research*, 22(10):1377–1384, sep 1986. ISSN 00431397. doi: 10.1029/WR022i010p01377.

G. Constantinescu, M. Koken, and J. Zeng. The structure of turbulent flow in an open channel bend of strong curvature with deformed bed: insight provided by detached eddy simulation. *Water Resources Research*, 47(5): W05515, may 2011. ISSN 0043-1397. doi: 10.1029/2010WR010114.

A. M. F. da Silva. *Alternate bars and related alluvial processes.* 1991.

A. M. F. da Silva. *Turbulent flow in sine-generated meandering channels.* PhD thesis, Queen's Univ., 1995.

A. O. Demuren and W. Rodi. Calculation of flow and pollutant dispersion in meandering channels. *J. Fluid Mech.*, 172:63–92, 1986. ISSN 0002-8606. doi: 10.1029/TR032i002p00222.

W. E. Dietrich. Mechanics of flow and sediment transport in river bends [in] river channels: environment and process. Special publications/Institute of British Geographers:179–227, 1987. ISSN 063114577X.

W. E. Dietrich and J. D. Smith. Influence of the point bar on flow through curved channels. *Water Resources Research*, 19(5):1173–1192, oct 1983. ISSN 00431397. doi: 10.1029/WR019i005p01173.

W. E. Dietrich, J. D. Smith, and T. Dunne. Flow and sediment transport in a sand bedded meander. *The Journal of Geology*, 87(3):305–315, may 1979. doi: 10.1086/628419.

J. G. Duan. Simulation of flow and mass dispersion in meandering channels. *Journal of Hydraulic Engineering*, 130(10):964–976, oct 2004. doi: 10.1061/(asce)0733-9429(2004)130:10(964).

T. H. El-Tahawy. *Patterns of flow and bed deformation in meandering streams: An experimental study.* PhD thesis, Department of Civil Engineering, Queen's University, Kingston, Ontario, Canada, 2004.

E. Elata and A. T. Ippen. The dynamics of open channel flow with suspensions of neutrally buoyant particles. Technical report, Hydrodyn Lab. Mass.Inst of Technol., Cambridge, 1961.

H. A. Enstein and N. Chien. Effect of heavy sediment concentration near the bed on the velocity and sediment distribution. *MRD Sediment ser. 8*, 1955.

L. Falcomer and V. Armenio. Large-eddy simulation of secondary flow over longitudinally ridged walls. *Journal of Turbulence*, 3(008):N8, jan 2002. ISSN 1468-5248. doi: 10.1088/1468-5248/3/1/008.

H. B. Fischer. The effect of bends on dispersion in streams. *Water Resources Research*, 5(2):496–506, 1969. ISSN 1944-7973. doi: 10.1029/WR005i002p00496.

A. Galea, M. Grifoll, F. Roman, M. Mestres, V. Armenio, A. Sanchez-arcilla, and L. Zammit Mangion. Numerical simulation of water mixing and renewals in the barcelona harbour area: the winter season. *Environmental Fluid Mechanics*, 14(6):1405–1425, dec 2014. ISSN 1567-7419. doi: 10.1007/s10652-014-9351-6.

G. Gelfenbaum and J. D. Smith. Experimental evaluation of generalized suspended-sediment transport theory. *Shelf sand and Sandstones*, 1986.

M. Germano, U. Piomelli, P. Moin, and W. H. Cabot. A dynamic subgrid-scale eddy viscosity model. *Physics of Fluids A: Fluid Dynamics*, 3(7): 1760, 1991. ISSN 08998213. doi: 10.1063/1.857955.

A. Ghanmi. Modeling of flows between two consecutive reverse curves. *Journal of Hydraulic Research*, 37(1):121–135, jan 1999. ISSN 0022-1686. doi: 10.1080/00221689909498536.

J. Guo and P. Y. Julien. Turbulent velocity profiles in sediment-laden flows. *Journal of Hydraulic Research*, 39(1):11–23, jan 2001. ISSN 0022-1686. doi: 10.1080/00221680109499798.

G. Gust. Velocity profiles with suspended sediment. *Journal of Hydraulic Research*, 22(4):263–289, aug 1984. ISSN 0022-1686. doi: 10.1080/00221688409499383.

E. R. Holley and G. Abraham. Laboratory studies on transverse mixing in rivers. *Journal of Hydraulic Research*, 11(3):219–253, jul 1973. doi: 10.1080/00221687309499775.

T. J. Hsu. On two-phase sediment transport: dilute flow. *Journal of Geophysical Research*, 108(C3):3057, mar 2003. ISSN 0148-0227. doi: 10.1029/2001JC001276.

A. T. Ippen. *Stream dynamics and boundary shear distributions for curved trapezoidal channels*. Department of Civil Engineering, Massachusetts Institute of Technology, 1962.

A. Khosronejad, C. D. Rennie, S. A. A. salehi Neyshabouri, and R. D. Townsend. 3d numerical modeling of flow and sediment transport in laboratory channel bends. *Journal of Hydraulic Engineering*, 133(10):1123–1134, oct 2007. ISSN 0733-9429. doi: 10.1061/(ASCE)0733-9429(2007)133:10(1123).

S. Kraft, Y. Wang, and M. Oberlack. Large eddy simulation of sediment deformation in a turbulent flow by means of level-set method. *Journal of Hydraulic Engineering*, 137(11):1394–1405, nov 2011. ISSN 0733-9429. doi: 10.1061/(ASCE)HY.1943-7900.0000439.

L. B. Leopold and W. B. Langbein. River meanders. *Scientific American*, 214(6):60–70, jun 1966. ISSN 0036-8733. doi: 10.1038/scientificamerican0666-60.

L. B. Leopold and M. G. Wolman. *River channel patterns: braided, meandering, and straight*. Washington: U.S. Govt. Print. Off., 1957. doi: 10.4324/9780203784662.

D. K. Lilly. A proposed modification of the germano subgrid-scale closure method. *Physics of Fluids A: Fluid Dynamics*, 4(3):633, 1992. doi: 10.1063/1.858280.

D. A. Lyn. A similarity approach to turbulent sediment-laden flows in open channels. *Journal of Fluid Mechanics*, 193(-1):1, aug 1988. ISSN 0022-1120. doi: 10.1017/S0022112088002034.

C. Meneveau, T. S. Lund, and W. H. Cabot. A lagrangian dynamic subgrid-scale model of turbulence. *J. Fluid Mech.*, 319(-1):353, jul 1996. doi: 10.1017/s0022112096007379.

A. J. Metha. *An introduction to hydraulic of fine sediment transport*. World Scientific Publishing Co.Pte.Ltd., 2013.

I. Moncho-esteve, G. Palau-salvador, K. Shino, and Y. Muto. Turbulent structures in the flow through compound meandering channels. *River flow conference*, 2010.

M. Muste and V. C. Patel. Velocity profiles for particles and liquid in open-channel flow with suspended sediment. *Journal of Hydraulic Engineering*, 123(9):742–751, sep 1997. ISSN 0733-9429. doi: 10.1061/(ASCE)0733-9429(1997)123:9(742).

M. Muste, K. Yu, I. Fujita, and R. Ettema. Two-phase versus mixed-flow perspective on suspended sediment transport in turbulent channel flows. *Water Resources Research*, 41(10):n/a–n/a, oct 2005. ISSN 00431397. doi: 10.1029/2004WR003595.

A. Petronio, F. Roman, C. Nasello, and V. Armenio. Large eddy simulation model for wind-driven sea circulation in coastal areas. *Nonlinear Processes in Geophysics*, 20(6):1095–1112, dec 2013. ISSN 1607-7946. doi: 10.5194/npg-20-1095-2013.

S. B. Pope. *Turbulent flows*. Springer-Verlag, Berlin/Heidelberg, 2000. doi: 10.1007/SpringerReference{_}67869.

L. Prandtl. *Essentials of fluid dynamics: with applications to hydraulics aeronautics, meteorology, and other subjects*. 1952 (various printings). Hafner Pub. Co., 1952.

H. Rouse. Modern conceptions of the mechanics of fluid turbulence. *Trans. A.S.C.E.*, 102:463–543., 1937.

I. L. Rozovskii. *Flow of water in bends of open channels*. Academy of Sciences of the Ukrainian SSR, 1957.

M. Shams, G. Ahmadi, and D. H. Smith. Computational modeling of flow and sediment transport and deposition in meandering rivers. *Advances in Water Resources*, 25(6):689–699, jun 2002. doi: 10.1016/s0309-1708(02)00034-9.

Y. Shimizu, H. Yamaguchi, and T. Itakura. Three-dimensional computation of flow and bed deformation. *Journal of Hydraulic Engineering*, 116(9):1090–1108, sep 1990. doi: 10.1061/(asce)0733-9429(1990)116:9(1090).

K. Shiono and T. Feng. Turbulence measurements of dye concentration and effects of secondary flow on distribution in open channel flows. *Journal of Hydraulic Engineering*, 129(5):373–384, may 2003. doi: 10.1061/(asce)0733-9429(2003)129:5(373).

K. Shiono and Y. Muto. Complex flow mechanisms in compound meandering channels with overbank flow. *Journal of Fluid Mechanics*, 376:S0022112098002869, dec 1998. ISSN 00221120. doi: 10.1017/S0022112098002869.

W. Siebert and W. Götz. A study on the deformation of secondary flow in models of rectangular meandering channels. *Proc. 16th Congress, IAHR,*, 2:141–149, 1975.

J. Smagorinsky. General circulation experiments with the primitive equations. *Monthly Weather Review*, 91(3):99–164, mar 1963. ISSN 0027-0644. doi: 10.1175/1520-0493(1963)091⟨0099:GCEWTP⟩2.3.CO;2.

J. D. Smith and S. R. Mclean. Spatially averaged flow over a wavy surface. *Journal of Geophysical Research*, 82(12):1735–1746, apr 1977. ISSN 01480227. doi: 10.1029/JC082i012p01735.

R. Smith. Where to put a steady discharge in a river. *J. Fluid Mech.*, 115 (-1):1, feb 1982. doi: 10.1017/s0022112082000615.

R. Smith. Longitudinal dispersion coefficients for varying channels. *J. Fluid Mech.*, 130(-1):299, may 1983. doi: 10.1017/s002211208300110x.

T. Stoesser, N. Ruether, and N. R. B. Olsen. Calculation of primary and secondary flow and boundary shear stresses in a meandering channel. *Advances in Water Resources*, 33(2):158–170, feb 2010. ISSN 03091708. doi: 10.1016/j.advwatres.2009.11.001.

N. Tamai, K. Ikeuchi, and A. Yamazaki. Experimental analysis of the open channel flow in continuous bends. *Proceedings of the Japan Society of Civil Engineers*, 1983(331):83–94, 1983. ISSN 1884-4936. doi: 10.2208/jscej1969.1983.331_83.

W. D. Tape. *Experimental investigation of flow patterns in meandering channels of moderate sinuosity.* PhD thesis, University of Windsor, 2001.

J. R. Taylor, S. Sarkar, and V. Armenio. Large eddy simulation of stably stratified open channel flow. *Physics of Fluids*, 17(11):116602, 2005. ISSN 10706631. doi: 10.1063/1.2130747.

C. Teisson, O. Simonin, J. Galland, and D. Laurence. Turbulence and mud sedimentation: a reynolds stress model and a two-phase flow model. In *coastal engineering 1992*, pages 2853–2866, New York, NY, jun 1993. American Society of Civil Engineers. ISBN 978-0-87262-933-2. doi: 10.1061/9780872629332.217.

R. E. Uittenbogaard. Physics of turbulence:technical report on subtask, mast veriparse project. Series paper 4, Delf Hydraul, 1994.

W. Van Balen. *Curved open-channel flows.* PhD thesis, 2010.

W. Van Balen, W. S. J. Uijttewaal, and K. Blanckaert. Large-eddy simulation of a mildly curved open-channel flow. *Journal of Fluid Mechanics*, 630:413, jul 2009. ISSN 0022-1120. doi: 10.1017/S0022112009007277.

W. Van Balen, K. Blanckaert, and W. S. J. Uijttewaal. Analysis of the role of turbulence in curved open-channel flow at different water depths by means of experiments, LES and RANS. *Journal of Turbulence*, 11:N12, jan 2010. ISSN 1468-5248. doi: 10.1080/14685241003789404.

L. C. Van Rijn. Sediment transport, part ii: suspended load transport. *Journal of Hydraulic Engineering*, 110(11):1613–1641, nov 1984. ISSN 0733-9429. doi: 10.1061/(ASCE)0733-9429(1984)110:11(1613).

V. A. Vanoni. Transportation of suspended sediment by water. *Trans ASAE*, 1946.

V. A. Vanoni. *Sedimentation engineering*. American Society of Civil Engineers, Reston, VA, mar 2006. ISBN 978-0-7844-0823-0. doi: 10.1061/9780784408230.

C. Villaret and A. G. Davies. Modeling sediment-turbulent flow interactions. *Applied Mechanics Reviews*, 48(9):601, 1995. ISSN 00036900. doi: 10.1115/1.3023148.

H. Von Schelling. Most frequent particle paths in a plane. *Transactions, American Geophysical Union*, 32(2):222, 1951. ISSN 0002-8606. doi: 10.1029/TR032i002p00222.

B. Vreman, B. Geurts, and H. Kuerten. On the formulation of the dynamic mixed subgrid-scale model. *Physics of Fluids*, 6(12):4057, 1994. doi: 10.1063/1.868333.

L. P. Wang and M. R. Maxey. Settling velocity and concentration distribution of heavy particles in homogeneous isotropic turbulence. *Journal of Fluid Mechanics*, 256:27–68, nov 1993. ISSN 0022-1120. doi: 10.1017/S0022112093002708.

R. G. Wetzel. *Lake and river ecosystems*. Academic Press Elsevier, third edition edition, 2001.

G. A. Weyhenmeyer. The influence of stratification on the amount and distribution of different settling particles in lake erken. *Canadian Journal of Fisheries and Aquatic Sciences*, 53(6):1254–1262, jun 1996. ISSN 0706-652X. doi: 10.1139/f96-057.

J. C. Winterwerp. Stratification effects by cohesive and noncohesive sediment. *Journal of Geophysical Research: Oceans*, 106(C10):22559–22574, oct 2001. ISSN 01480227. doi: 10.1029/2000JC000435.

M. S. Yalin. *River mechanics*. Oxford: Pergamon Press, 1992.

M. S. Yalin and A. M. F. da Silva. *"fluvial processes"*. International Association of Hydraulic Engineering and Research (IAHR) Monograph, The Netherlands, 2001.

Y. Zang, R. L. Street, and J. R. Koseff. A non-staggered grid, fractional step method for time-dependent incompressible navier-stokes equations in

curvilinear coordinates. *Journal of Computational Physics*, 114(1):18–33, sep 1994. ISSN 00219991. doi: 10.1006/jcph.1994.1146.

U. C. E. Zanke. Berechnung der sinkgeschwindigkeiten von sedimenten. Technical report, Mitteilungen des Franzius-instituts fur wasserbau, Technische Universitat Hannover, 1977.

E. A. Zedler and R. L. Street. Large-eddy simulation of sediment transport: currents over ripples. *Journal of Hydraulic Engineering*, 127(6):444–452, jun 2001. ISSN 0733-9429. doi: 10.1061/(ASCE)0733-9429(2001)127:6(444).

J. Zeng, G. Constantinescu, and L. Weber. 3d calculations of equilibrium conditions in loose-bed open channels with significant suspended sediment load. *Journal of Hydraulic Engineering*, 136(9):557–571, sep 2010. ISSN 0733-9429. doi: 10.1061/(ASCE)HY.1943-7900.0000213.